On the stability of cerium inhibiting layers on aluminium 2024-T3: an *in situ* optical and electrochemical study

Matteo Olgiati

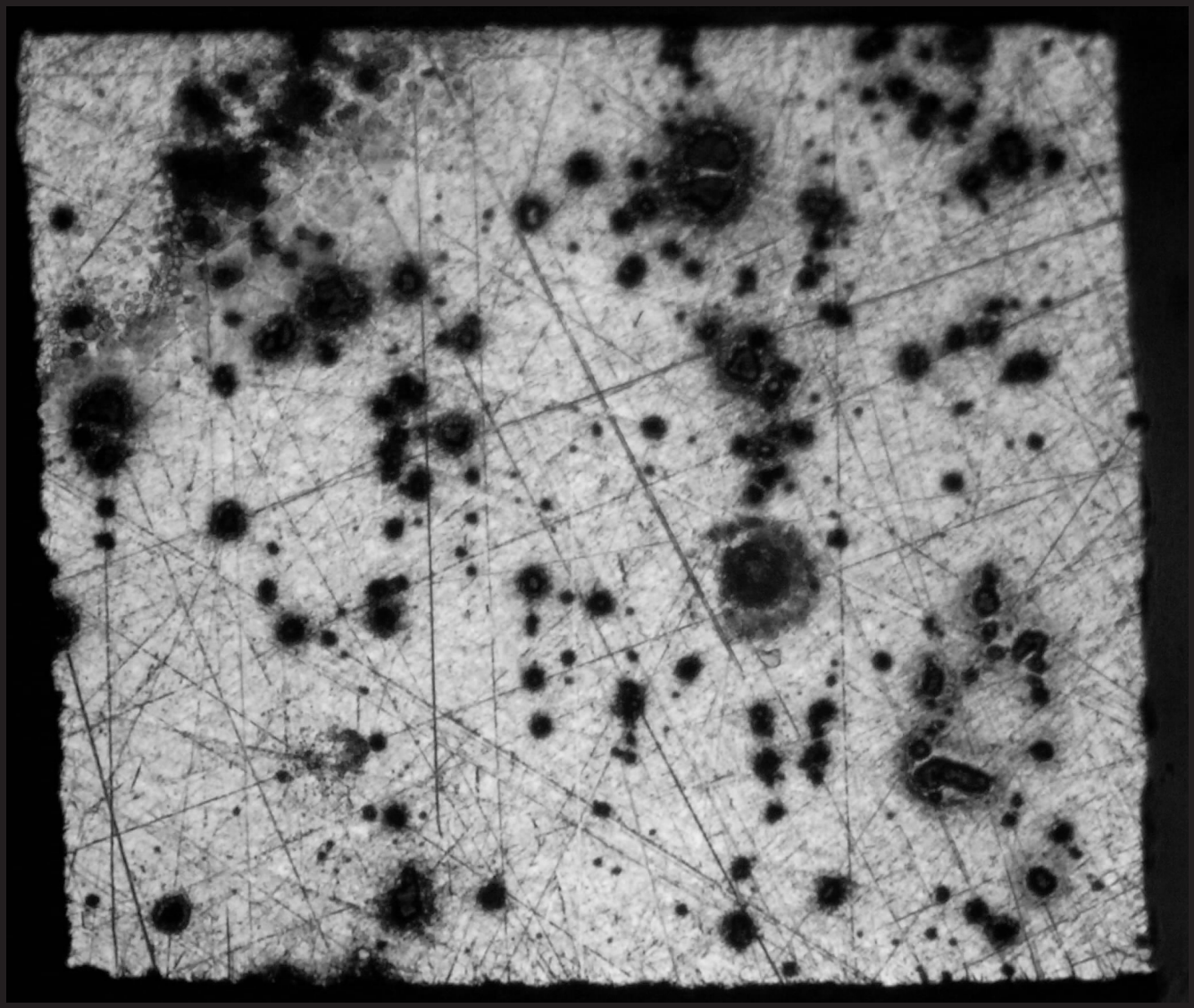

TU Delft

THIS PAGE IS INTENTIONALLY LEFT BLANK

On the stability of cerium inhibiting layers on aluminium 2024-T3: an *in situ* optical and electrochemical study

by

Matteo Olgiati

to obtain the degree of Master of Science in Materials Science and Engineering
at the Delft University of Technology,
to be defended publicly on Thursday March 5, 2020 at 9:00 AM.

Student number:	4745078	
Project duration:	April 1, 2019 – March 5, 2020	
Thesis committee:	Dr. Y. Gonzalez-García,	TU Delft, Faculty of 3mE (MSE), Exam committee chair
	Dr. S. J. García Espallargas,	TU Delft, Faculty of LR (NovAM), Thesis supervisor
	Prof. dr. ir. S. van der Zwaag,	TU Delft, Faculty of LR (NovAM), External member
	P. J. Denissen,	TU Delft, Faculty of LR (NovAM), Daily supervisor

This thesis is confidential and cannot be made public until March 5, 2021.

"L'arte è questo: scappare dalla normalità che ti vuole mangiare.
Io fuggo sempre, e i miei disegni sono così perché so che
possono essere cancellati, divorati in un attimo.
Eppure so che uno di questi, almeno uno, o tanti, durerà
milioni di anni"

Benni S., *Margherita Dolcevita*

Abstract

Salts of trivalent cerium (Ce(III)) are known to successfully hinder localised corrosion phenomena typical of aerospace aluminium alloys by forming a thin passivation layer on top of the corrosion-active intermetallic phases. This is generally observed to happen when the alloy is under immersion conditions in a solution containing Ce^{3+} ions. However, some very preliminary works suggest that protection provided by this layer is lost once the passivated metal is re-exposed to a corrosive solution in absence of inhibitor (for example, aqueous solution of sodium chloride). This (in)stability process has not been directly addressed in literature and is, therefore, not well understood. A deeper understanding of such process and the strategies that could lead to a higher passive layer stability are needed to bring Ce-based inhibitor technologies closer to application and replacement of the harmful Cr(VI)-based primers.

In this work we studied the inhibition mechanism and stability of cerium inhibiting layers created on AA 2024-T3 upon exposure to electrolytic solutions containing $Ce(NO_3)_3$ and NaCl. The stability of Ce(III) layers after re-exposure to corrosive electrolytes (*i.e.* without inhibitors) is investigated. Furthermore, the interaction between Ce(III) layers and different organic compounds, namely 2,5-Dimercapto-1,3,4-thiadiazole (DMTD), phytic acid and sodium alginate, was also explored as a potential strategy for stabilisation of Ce-based inhibitive layers.

Due to the complex interpretation of electrochemical signals typically used in corrosion studies (*e.g.* electrochemical noise and impedance spectroscopy), it was decided to combine such electrochemical methods with highly spatio-temporally resolved *in-situ* microscopy in order to assess both corrosion of AA 2024-T3 and its inhibition. For this purpose, a home made optical-electrochemical experimental setup was used, together with a protocol for optical data analysis. This hyphenated *in-situ* protocol is further supported with SEM-EDS, Raman and SKPFM analysis after exposure.

In the work here presented, the unstable nature of Ce-inhibitive deposits was found to be associated to their dissolution after re-exposure to inhibitor-free electrolytes. Studies devoted to the stabilisation of Ce(III)-inhibitive layers with organic molecules indicated different behaviours and outcomes. Alginate oligomers efficiently passivate the Ce-protected intermetallic phase, but, at the same time, destabilise the Al-rich matrix, which became subject to general corrosion. Phytic acid was found to provide synergy with Ce(III) layers, which however lacked in stability. Treatment of Ce-passivated surfaces with DMTD, on the other hand, shows a significantly delayed onset of optical-electrochemical activity upon re-immersion in NaCl solution, which suggested the accomplishment of a more stable system. The results obtained confirm the power of *in-situ* (*i.e.* under immersion) optical investigation not only to support the understanding of complex electrochemical signals, but also to deliver quantitative information relevant in corrosion and inhibition studies. The approach proposed in this research is believed to be of future help for an improved design of Cr(VI)-free anticorrosion coating systems.

Acknowledgments

This thesis seals the end of my unpredictably amazing journey as a MSc student at TU Delft and, for this reason, I would like to thank all those people that contributed to the accomplishment of this work. First of all, my acknowledgment goes to Dr. Santiago Garcia and Paul Denissen for their supervision throughout this project. Secondly, I would like to thank Prof. Sybrand van der Zwaag for accepting to be part of the thesis committee. I am also very grateful to all the other NovAM colleagues for welcoming me in their group and being source of daily fun and laughter. I could not be more grateful to Aytac Yilmaz for all the help he gave with SKPFM measurements as well as the interpretation of results. Special thanks also go to Dr. Yaiza Gonzalez Garcia, not only for accepting to be part of the thesis committee, but also for being a great source of inspiration during the months back in my own faculty.

Reaching this goal will be an inevitable "rite of passage" for my life, but I also find it difficult to put the word "end" onto something that has meant so much for me. Therefore, I would like to mention not just the lessons learnt from such experience, but also the good things that will remain for the future.

First of all, the interest for this discipline. I can fairly say I have no regrets for choosing this track for my studies and I will do my best to keep fostering such interest with care, resolution and passion in the coming years.

Secondly, the friends. I would like to reserve special thanks to all my "day-ones", my little second "rimasterrimi" family, precisely Isa, Zia, Michelozzo, Fiorellino, Emmis, Leo, Sam, Anto and Ben. *A volte mi domando come avrei fatto senza di voi. Insieme abbiamo condiviso così tanto: risate, birre, cene in compagnia, serate, ma anche delusioni e momenti di sconforto. Con voi mi sono sentito a casa. Vi ringrazio per ogni singolo sorriso che mi avete regalato, per ogni abbraccio e per ogni piccolo gesto quotidiano che ci ha resi così uniti in questi due anni. Non avrei mai potuto chiedere di trovare Amici migliori. Spero che i vostri sogni possano sempre realizzarsi. A presto e AD MAIORA.*

Finally, the fortune. These two years in Delft made me realise how lucky I have been in my life for all the opportunities I was given that allowed me to become the person I am today. I was lucky enough to be born in a wonderful family, who always believed in my strength (sometimes even more than I do) and never hesitated to encourage, support and push me beyond my limits in order to pursue my dreams. Words cannot express all the love that I can feel for all and each of you. I am especially grateful to my father Marzio, my mother Elisabetta and my sister Chiara. They are simply the fuel of my days and daily source of inspiration. *Vorrei che ci fossero parole adeguate e proporzionali alla stima e affetto che nutro nei vostri confronti. Vi sono eternamente grato per avermi dato l'opprotunità di intraprendere questo percorso e per avermici accompagnato malgrado la distanza. Grazie per ogni secondo trascorso a chiacchierare al telefono. Grazie per i mille scarifici che avete fatto per permettermi di essere dove sono. Grazie per avermi insegnato a rialzarmi dalle sconfitte, ma soprattutto grazie per avermi insegnato a credere nei miei sogni. Ogni giorno mi sento fortunato di sapere di poter sempre contare su di voi. Spero che in questo giorno così importante possa rendervi orgogliosi di me. Vi voglio incommensurabilmente bene.*

Contents

List of Figures

Nomenclature

2-MBT	2-Mercaptobenzothiazole
2XXX	Aluminium series two thousand
AA	Aluminium alloy
AA%	Affected area %
BSE	Backscattered electrons
BTA	Benzotriazole
CE	Counter electrode
$Ce(dbp)_3$	Cerium dibutylphosphate
Ce(III)	Trivalent cerium
Ce(IV)	Tetravalent cerium
$Ce(NO_3)_3$	Cerium nitrate
Cr(VI)	Hexavalent chromium
DEDTC	Diethyldithiocarbamate
DMTD	2,5-Dimercapto-1,3,4-thiadiazole
EDS	Energy dipersive X-ray spectroscopy
EIS	Electrochemical impedance spectroscopy
IM(s)	Intermetallic(s)
IMCs	Intermetallic phase constituents
LT	Lower threshold
LUT	Look-up table
NaCl	Sodium Chloride
OCP	Open circuit potential
PHA	Phytic acid
RE	Reference electrode
REACH	Registration, Evaluation, Authorization and Restriction of Chemicals
REEs	Rare earth elements
ROI	Region of interest
SEM	Scanning electron microscopy
SKPFM	Scanning Kelvin Probe Force Microscopy
SSSS	Supersaturated solid solution
UT	Upper threshold
WE	Working electrode
XANES	X-ray absorption near edge spectroscopy

Chapter 1

Introduction

This chapter serves as an introduction for the reader to get acquainted with the main topics tackled throughout the manuscript. First, the problem of aluminium aerospace alloys and their susceptibility to localised corrosion is exposed based on scientific literature. Corrosion of AA 2024-T3 is especially addressed, as it will be subject of further research in the following chapters. With the same approach, a literature study on the corrosion inhibition provided by Ce(III) inhibitors is also presented, in order to justify the need for effective protection of aluminium aerospace structures, as well as the choice of Ce(III) inhibitors for further investigations. Finally, the current limitations and focus issues addressed throughout the thesis are proposed, together with the objectives and research questions of the project. The outline of the thesis and its structure are also clarified.

1.1 Corrosion of aluminium 2024-T3 in the aerospace industry

Since the 1930s, aluminium alloys have been attracting considerable attention in the aerospace industry for they satisfy two crucial structural prerequisites: i) adequate mechanical strength and ii) lightweightness [1]. Among these, the alloy AA 2024-T3, commonly used in aircraft manufacturing for structural components, belongs to the 2XXX series, meaning that Cu is the main alloying element. This alloy is especially suited for its good fatigue resistance and high strength-to-weight ratio. In order to achieve such mechanical attributes, aluminium is alloyed not only with Cu ($\approx$ 4.5 wt.%), but also with smaller additions of other alloying elements (Mg 1.5 wt%, Mn 1 wt.%, Fe and Si $<$ 0.5 wt.%). Overall, AA 20204-T3 has the highest level of alloying metals among Al alloys, which makes its final microstructure rather intricate [2]. The latter is obtained through a heat-treatment known as "age-hardening", which entails the formation of a metastable super saturated solid solution (SSSS) after quenching, followed by segregation of finely dispersed precipitates rich in alloying elements within the grains [3], as a consequence of their decreased solubility. The alloying metals-rich particles formed can have variable size, ranging from 20 nm to 500 nm, and different degree of crystallographic coherency with the matrix [3]. Partially coherent hardening precipitates (20-200 nm) generally offer strengthening by impeding dislocation slip *via* a cutting mechanism of the dislocation through the particle [4, 5]. Incoherent dispersoids (50-400 nm), on the other hand, can limit both dislocations slip with an Orowan-like mechanism and act as pinning elements to limit grain growth [3–5].

Segregates of bigger size (0.5-500 μm), which are also known as intermetallic phase constituents (IMCs) or intermetallic (IM) particles, can also be formed, sometimes even during primary ingot production [3]. Their composition is still richer in alloying elements (Cu especially) if compared to the Al-rich matrix, but they do not contribute significantly to the strengthening of the alloy. However, the difference in composition between these and the surrounding matrix makes the electrochemical activity (locally) heterogeneous once the metal is exposed to a corrosive environment. For this reason, IMCs are responsible for the issues that this alloy presents when it comes to localised corrosion. Considering that this alloy is highly employed in structural components of aircrafts (fuselage, wings, rudder, *etc.*), understanding corrosion of AA 2024-T3 and its protection have always been hot topics within the aerospace industry, in order to guarantee safety during both flight and service lifetime of aircrafts, thereby preventing catastrophic failures. Corrosion of AA 2024-T3 alloy in chlorine-containing environments is taken as a landmark in the present research, given its engineering importance in the field of aircraft manufacturing.

1.1.1 Basic principle of corrosion

With the term (wet) "corrosion", materials scientists tend to indicate a degradation process, involving mainly metals, as a result of the electrochemical interaction between the metal itself and the surrounding (aqueous) environment to which this is exposed [6]. From basic principles of electrochemistry, it is well known that corrosion phenomena make metallic substrates susceptible in presence of water and other corrodent species (oxygen, for instance), so that the general half-cell reactions involving mass and (electronic and ionic) charge transfer can be established according to the following reactions:

$$Me \longrightarrow Me^{n+} + ne^{-}, \tag{1.1}$$

$$O_2 + 2H_2O + 4e^{-} \longrightarrow 4OH^{-}. \tag{1.2}$$

Equation (1.1), represents the oxidation of a generic metal (Me) and its dissolution as a cation with valence "n". This process takes place in certain locations of the surface called "anodes" and the reaction in (1.1) is called anodic. Equation (1.2), on the other hand, represents the reduction of species generally coming from the environment and it strongly depends on the type of environment and its acidity. For neutral aerated solutions equation (1.2), also known as reduction of oxygen, is the most likely to happen, but reduction of other species may be favoured in different environmental conditions. The surface locations where this process takes place are called "cathodes" and the reaction in (1.2) is called cathodic. A corrosion process, as schematically illustrated in Figure 1.1, always proceeds when anodic and cathodic reactions are coupled together.

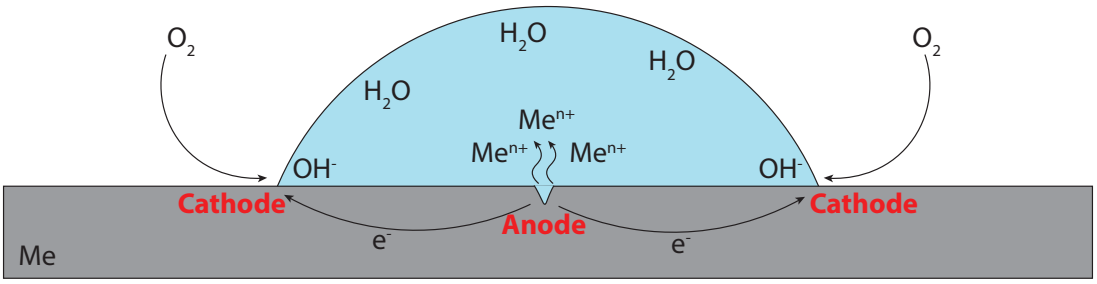

Figure 1.1: Schematic representation of the environmental corrosion mechanism for a generic metal substrate, where anodic and cathodic areas are highlighted together with their respective reactions.

1.1.2 Corrosion models for AA 2024-T3

In general, corrosion of aluminium alloys is of localised nature and AA 2024-T3 is no exception to this trend. The interaction between local active anodes and cathodes on the surface is the driving force leading to the development of different forms of localised corrosion. Generation of local anodic and cathodic areas on the surface of aluminium alloys is ascribed to the differences in composition within the alloy microstructure. For AA 2024-T3, in particular, second phase particles like the IMCs, frequently have solution potentials differing from that of the solid solution matrix, resulting in localised (micro-) galvanic cells [3]. The micro-galvanic couplings spread across the surface set the basis for initiation and propagation of different corrosion phenomena.

Corrosion of AA 2024-T3 has been extensively studied throughout the years [2, 3, 7–25] because the complexity of its process has always been source of great interest and debate. Nowadays, there is general agreement in categorising the development of AA 2024-T3 corrosion phenomena based on the temporal sequence of events, which, as a consequence, translates in studying corrosion events at different length scales. Therefore, the following structure is proposed in the subsequent sections to best describe other findings in literature related to this topic: i) initiation of local corrosion around isolated IMs (section 1.1.2.1) [9] and ii) propagation to a global scale involving interaction between multiple IMs and subsurface attack (section 1.1.2.2) [10, 11].

1.1.2.1 Localised corrosion of AA 2024-T3

In the study of A. Boag *et al.* [9], the authors showed that short immersions ($\approx$ 30 minutes) in diluted NaCl aqueous solutions (0.1 M) led to early and fast corrosive attack on the IM particles. The type, morphology and onset of the attack, however, were found to vary significantly depending on the IM particle composition and, consequently, its electrochemical activity. Despite the difficulty in pre-determining the particles' activity [2, 3, 8], the authors of [9] propose a IM phase classification into four main macro-families, which has been frequently adopted in other studies [2, 9, 12–14], consisting of:

- The Al-Cu phase (Al_2Cu), also known as θ phase, whose electrochemical potential is generally cathodic with respect to the Al matrix;
- The Al-Cu-Mg phase (Al_2CuMg), also known as S phase, whose electrochemical potential is generally anodic with respect to the Al matrix, but it turns cathodic after initial anodic dissolution of Mg;
- The Al-Cu-Fe-Mn phase, whose range of compositions is wide, but generally behaves cathodically with respect to the Al matrix;
- The Al-Cu-Fe-Mn-Si phase ($(Al,Cu)_x(Fe,Mn)_ySi$), whose electrochemical potential is generally cathodic with respect to the Al matrix.

Amongst others, S phases are believed to be one of the most active and promptly affected by corrosion due to their anodic character, which makes them undergo preferential anodic dissolution of the least noble elements (Mg and Al). After remarkable selective dissolution, however, Cu-enriched remnants are left behind, which will turn their behaviour cathodic due to the high level of Cu achieved. This assumption was confirmed by SKPFM studies on S phases, where Cu-rich sponge-like remnants were observed as a result of anodic dissolution, typically accompanied by replating of Cu nanoparticles in the immediate surroundings (Cu smut) [15–17].

On the other hand, the cathodic particles (and so the S phase when it turns cathodic due to Cu enrichment) are normally attacked on their periphery with a typical morphology known as "trenching". Trenching is attributed to the attack of the surrounding Al-matrix, rather than the particle itself, as a consequence of the local cathodic alkalinisation.

O. Schneider *et al.* [18], however, proposed an alternative (anodic) model to explain initiation of trenching, since the alkaline model cannot account for other factors like the effect of Cl^- content on trenching initiation, trenching at lower pH, and different trenching kinetics on particles with different composition/activity. They therefore proposed trenching to be ascribed to nucleation and coalescence of metastable pits around the IM particles [18] (or sometimes within the particle if phase domains are visible [13]). Nucleation of pits in a small region of the Al matrix adjacent to the IM particles becomes favoured because such region was found to be substantially depleted in Cu [19], thus causing a local lowering of the pitting potential [20]. The confirmation of metastable pitting was found in studies on electrochemical noise current transients [21], which enabled to identify populations of short-lived and metastable events in the signal during early immersion. These are believed to have different nature from stable growth of pits, which is generally characterised by big steps in the background current of longer duration [2].

Given the different composition and activity of the IM particles, A. Boag *et al.* [9] observed a certain temporal hierarchy of local corrosion in 2024-T3, which makes the onset of trenching around isolated IMs delay in time as shown in Figure 1.2. S phase is the most active, and corrosive attack such as dealloying and trenching can be seen already within the first 15 minutes of immersion. For prolonged immersion times, AlCuFeMn phase starts to be attacked, followed in turn by Si-containing phases.

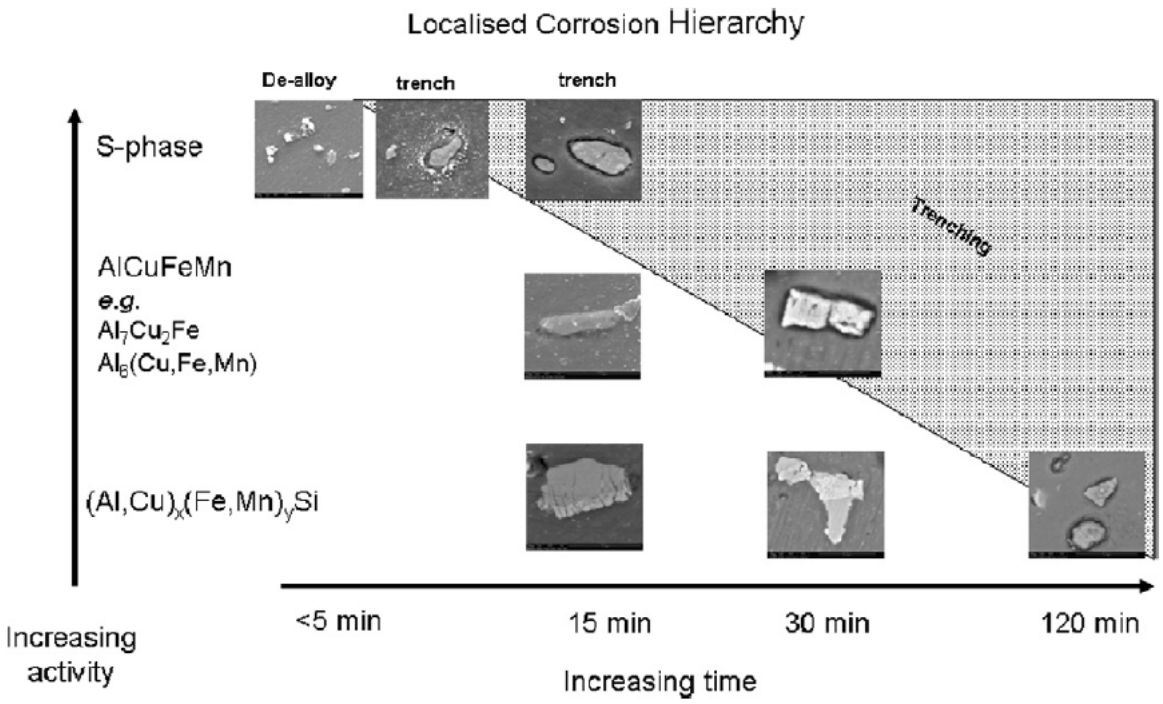

Figure 1.2: Hierarchy of localised corrosion attack [9].

1.1.2.2 Global corrosion of AA 2024-T3

Further propagation of metastable pits (trenches) into stable pitting can happen for prolonged immersion times, as long as certain conditions favouring their growth are met. In 1994 [22], it was proposed as a general condition that growth of a pit becomes favoured when the product of the current density (i) and the depth of the pit (r_{pit}) is higher than 10^{-2} A cm^{-1}. Recent studies [10, 23] propose that such condition can be satisfied in AA 2024-T3 when co-operative effects between IMs of opposite electrochemical activity start to play a role. Co-operative clustering of IMs together with Cu enrichment of the surface, for example, was found to be a driving force to increase the local activity (*i.e.* the corrosion rate), so that condition to support stable pitting ($i \cdot r_{pit}$ product) is met. Hence, surface and subsurface clustering of IMs with opposite activities have been lately emerging as essential conditions to have stable pit initiation and propagation, respectively, as discussed in [10, 23]. The co-operative clustering action between IMs is typically recognisable for the appearance of corrosion rings. These rings are normally centred on the corrosion pits (*i.e.* clustered IMs) and their size was observed to range between 50-200 μm [10, 11, 26]. Corrosion rings are also capped with copious amounts of corrosion products (also known as corrosion "domes") [10] and the centres of these rings were observed to be active anodes evolving H_2 gas, thus suggesting subsurface penetration of pits until trenches are driven to the grain boundary network. Subsurface attack of the grain boundaries (intergranular corrosion) becomes the dominant process at long immersion times ($>$ 120 min), eventually leading to grain etch-out [10, 11].

The susceptibility of AA 2024-T3 to corrosive attack and the celerity of propagation justify the need for its prevention at all levels.

1.2 Protection of AA 2024-T3 with Ce(III) salts

1.2.1 Active corrosion protection of AA 2024-T3

In the aerospace industry, diverse solutions have been adopted throughout the years to deal with the detrimental effects of corrosion. Among these, layers of organic coatings have demonstrated to be reliable options to protect structural aluminium aerospace alloys (thus including AA 2024-T3) from corrosion, especially in a long-term perspective. Organic coatings, indeed, provide passive barrier-like protection to the metal by limiting the diffusion of water, oxygen and other "corrodents" towards its surface. However, direct exposure of these coatings to the external environment often requires them to withstand harsh conditions, which make them an easy target for the occurrence of flaws and damages. When a coating is locally damaged, the metal substrate underneath becomes locally unprotected and vulnerable to corrosive attack [27].

To overcome this limitation, the concept of active corrosion protection by means of corrosion inhibitors became increasingly prominent for aerospace coatings. Water soluble inhibiting compounds can be introduced into the coating formulation (namely in a primer), so that they can i) be released from the coating matrix once a defect occurs (leaching), ii) interact with the exposed surface of the metal and iii) provide (active) corrosion protection to the damaged area. In this way, the further loss of protective properties is impeded and the coatings' protective function is self-restored [28–31].

For many years, Cr(VI)-based compounds have represented the elected inhibitor to achieve active protection of AA 2024-T3 and other aerospace alloys. Their excellent long-term protective properties made it possible to employ them not only for corrosion inhibition, but also for conversion coating pretreatments, thus becoming a robust reality for this sector. Despite their performance, Cr(VI) inhibitors have been lately raising suspicions due to the health hazards and potential carcinogenic power that they can bring about. Their usage in many other fields of applications has been prohibited by the Registration, Evaluation, Authorization and Restriction of Chemicals (REACH), but their limitation in the aerospace industry is still somewhat restrained due to the higher safety demands of this field. The need for alternative inhibitors has aroused a massive driver within the scientific community to look for "greener" and more benign replacements and, for the same reasons, the present research project attempts to fit into the same context.

1.2.2 The choice of Ce(III) inhibitors as a Cr(VI)-free alternative

New trends in literature have emerged in the pursuit of "green chemistry" of inhibitors as a replacement for Cr(VI) [32]. In the context of active corrosion protection, in particular, numerous inhibitors have been investigated with the hope of finding a suitable replacement. Efforts have been devoted to study both organic inhibitors, such as various azoles [33–36] or 8-Hydroxyquinoline [37, 38], and inorganic inhibitors, such as Li salts [39–42], salts of rare earth elements (REEs) [43–46] or different molybdates, phosphates, vanadates, tungstates, *etc.* [47].

In spite of the extensive and ongoing studies on several corrosion inhibitors, a chemical substance capable of replacing Cr(VI) compounds still struggles to be found. This happens because the various Cr(VI)-free candidates should be able to satisfy the same requirements of the highly-debated Cr(VI), especially they should provide similar performance (in terms of level of protection), ease of adaptability/implementation to the current technologies and price-friendliness (at least comparable to the one of Cr(VI)). Although some new Cr-free technologies (for example, the one based on Li salts) have already found concrete industrial application due to the satisfactory properties achieved, in the present research rare earth trivalent cerium salts (Ce(III)) were further investigated as another potential alternative. In particular:

- The fast and versatile solubility of Ce(III) salts in water makes them good candidates as leachable inhibitors for the active corrosion protection of damaged organic coatings [28]. Unlike the case of organic inhibitors, the inorganic nature and solubility of Ce(III) salts may enable prompt release from the coating matrix and a fast protection to the vulnerable AA 2024-T3. Innovative concepts for corrosion inhibitor storage are being developed in this regard, aimed at achieving controlled and on-demand release of Ce(III) species only when a damage occurs on the coating. Nanoporous silica exoskelotons of diatomaceous earths [48], electrospun nano-inhibitng networks [49], hydroxyapatite microparticles [50] and zeolitic reservoirs [51] are just a few examples of efficient carriers of Ce(III) inhibitors.
- Literature also shows that there is an emerging interest in the development of Ce-based conversion coatings baths [52–55] as a replacement of the classic Cr(VI)-based pretreatment. Conversion coatings are particularly relevant for

the aerospace industry, where they are not only used to strengthen the passive protection of aluminium structure, but they also act as a primers for the promotion of adhesive bonding with the subsequent coating system.

- Furthermore, minerals of cerium may also represent an economic alternative given both its relative abundance on Earth (almost similar to Cu) and the low price pressure due to the demand in other already well-established fields other than corrosion protection [56]. Ce is most of the times a residue during mining and primary extraction of other REEs [57], thus being cheaper than other REEs salts. It is actually also cheaper than other (inorganic) inhibitors like Li salts [58].

All these aspects make Ce(III) a close and potential alternative to Cr(VI), whose outstanding performance, however, is still difficult to emulate, since there are still several unknowns in the corrosion protection mechanism of Ce-salts. Focus of this research will be to investigate the properties of Ce(III)-based inhibitors and their limitations, in order to understand how the corrosion inhibition efficiency can be improved.

1.2.3 Different theories on the inhibition mechanism of Ce(III) compounds

Trivalent cerium compounds, as well as other REEs, are known to inhibit corrosion on different metals mainly as a precipitation film-forming type of inhibitor [59], meaning that their mechanism of inhibition relies on the precipitation of Ce(III) species on the corroding metal, that will consequently affect the anodic and/or cathodic reactions. In particular, it is generally accepted that deposition of insoluble hydroxides [60], formed in presence of an alkaline environment [61], limits further diffusion of aggressive species towards the surface of the metal, thus slowing down corrosion significantly. By looking at the Pourbaix diagram of Ce(III) (see Figure 1.3), for example, it can be seen that for alkaline pH, the hydroxide form becomes thermodynamically the most stable phase for a relatively wide range of potentials.

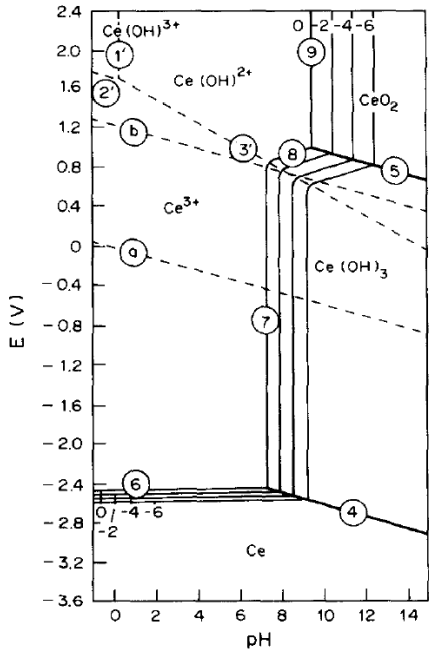

Figure 1.3: Potential (E) *vs* pH stability diagram (Pourbaix) of cerium [62].

In the case of AA 2024-T3, cathodic reactions like oxygen reduction (see equation (1.2)), supported with a higher rate on the cathodic IM particles, generate a local increase of the solution pH. Consequently, selective precipitation of insoluble $Ce(OH)_3$ over the cathodic IM sites becomes favoured according to the following reaction:

$$Ce^{3+} + 3OH^- \longrightarrow Ce(OH)_3 \downarrow \tag{1.3}$$

The insoluble precipitate limits further diffusion of oxygen towards the cathodic sites, thereby slowing down its consumption and, consequently, the corrosion kinetics [63]. Such pH-triggered precipitation mechanism and the consequent protection achieved have been confirmed in studies using simplified galvanic couples (*e.g.* pure metals coupled together), to test the selective formation of a precipitate on the cathodic metal [64–67], as well as to check the suppression of alkaline regions (made evident with pH indicators) around the cathodic metal once the Ce(III) inhibitor is added to the solution [68].

The basic inhibitory mechanism just explained for Ce is known to be the same also for other lanthanides, as they precipitate as hydroxides in high pH environments [45, 60, 69]. However, Ce(III) inhibitors are known to provide superior

protective properties compared to other REEs [46] and many studies have been trying to understand why. In the study of K. A. Yasakau *et al.* [69], polarization curves performed during immersion in $Ce(NO_3)_3$ solutions show that increased corrosion inhibition efficiencies are noticed when the time of immersion is also increased, while in the case of $La(NO_3)_3$, this increased protection with time is not as evident. For this reason, the authors envisaged that Ce(III) can provide better protective properties as a consequence of the oxidation of Ce from a trivalent to a tetravalent state, causing the formation of a stable insulating layer of cerium oxide (CeO_2). Similar observations were made by A. J. Davenport *et al.* [62], who noticed by means of X-ray absorption near edge spectroscopy (XANES) typical signal belonging to Ce in its trivalent state after 5 days and signal belonging to tetravalent Ce after 7 days of exposure to $CeCl_3$ 4 mM solution, suggesting that oxidation of Ce(III) has happened already during immersion, with time and extent of aeration being (possible) critical parameters. The authors concluded that further work is required to understand such observation.

Presence of CeO_2 in Ce inhibitive deposits was confirmed by compositional studies. In the work of D.R. Arnott *et al.* [44], for example, Auger and X-ray photoelectron spectroscopies were employed to elucidate more on the composition of Ce layers on AA 7075. They found that the deposits possess a mixed composition consisting of Ce oxy-hydroxides present in both oxidation states of Ce, namely Ce(IV) as a crystalline CeO_2 phase and $Ce(OH)_4$ phase and Ce(III) as amorphous $Ce(OH)_3$. The mixed oxide-hydroxide nature of the deposits was confirmed also in other studies [55, 70], but the formation of Ce(IV) and, consequently, the whole mechanism of Ce inhibition remained still somewhat unclear. Moreover, detection of Ce layers in their tetravalent state has been mainly relying on *ex situ* analytical techniques so far, which raises the question whether the actual oxidation could not be simply the result of samples drying before being tested. This option seems to be confuted in the work of A. J. Davenport *et al.* [62], where a clear distinction between Ce(III) and Ce(IV) XANES signals obtained *via* a similar titration-precipitation mechanism was outlined.

Assuming that Ce(III) to Ce(IV) does happen already during immersion, another question that has triggered the interest of many scientists is whether such oxidation happens before precipitation (*i.e.* Ce in ionic state) or after precipitation (*i.e.* Ce(III) first precipitates as a hydroxide and then gets oxidised) [52]. The most widely accepted model nowadays to explain formation of Ce(IV) oxide *in loco* was put forward in the work of A. J. Aldykiewicz *et al.* [71], where the authors related the oxidation of cerium to the oxygen reduction reaction kinetics. In particular, they propose two pathways for oxygen reduction to happen: the first involving the consumption of four electrons (four-electron pathway), the second involving the consumption of two electrons at a time (two-electron pathway). When oxygen is reduced by the direct consumption of four electrons (four-electron pathway), reference to following equation can be made:

$$O_2 + 2H_2O + 4e^- \longrightarrow 4OH^- \tag{1.4}$$

The same equation can be re-written as if it involved 2 stages, so that two electrons at a time are consumed (two-electron pathway) and H_2O_2 is produced as an intermediate of reaction according to the following:

$$O_2 + 2H_2O + 2e^- \longrightarrow H_2O_2 + 2OH^- \tag{1.5}$$

$$H_2O_2 + 2e^- \longrightarrow 2OH^-. \tag{1.6}$$

To couple this cathodic reactions, the authors considered the following anodic equilibrium equation, which was also reported by A. J. Davenport *et al.* [62] and represented in Figure 1.3 with the slope labelled as 3':

$$Ce^{3+} + 2H_2O \longrightarrow Ce(OH)_2^{2+} + 2H^+ + e^-. \tag{1.7}$$

In summary, the authors considered two separate scenarios in which O_2 and H_2O_2 act as oxidising agents to promote equation (1.7) according to the four- and two-electron pathways, respectively. They concluded these two pathways are favoured at different stages during Ce inhibition process, so that oxygen acquires a dual role [62, 71]:

- In the early stages of immersion, oxygen is consumed by the cathodic sites according to the four electron-pathway (equation (1.4)), because of the steady supply of 4 e^- from the metal substrate. This reaction, however, causes a prompt increase in pH, which makes the Ce^{3+} ions in solution precipitate as $Ce(OH)_3$ (equation (1.3)).
- Selective precipitation of $Ce(OH)_3$ on the cathodic sites, however, limits the cathodic reactions rate remarkably. Oxygen reduction is strongly inhibited so that it becomes more likely to happen (if it happens) *via* the consumption of 2 electrons rather than 4, thus following the two-electron model. In this way, formation of H_2O_2 is promoted for longer immersion times, which in turn may favour the fast oxidation of Ce(III) to Ce(IV) according to the following:

  $$2Ce^{3+} + 2OH^- + H_2O_2 \longrightarrow 2Ce(OH)_2^{2+}, \tag{1.8}$$

  before decomposing as described by equation (1.6).

Due to the stability of $Ce(OH)_2^{2+}$ at very low values of pH only [72, 73], this model was revised throughout the years, in which surface precipitation as hydrated cerium oxide in presence of neutral-alkaline environments has to be accounted for [74]. Some studies proposed also formation of other Ce(IV) intermediates than $Ce(OH)_2^{2+}$, like $Ce(OH)_4$ [69, 75] or $Ce(OH)(OOH)^{2+}$ [53], but eventually leading to the formation of CeO_2. The presence of H_2O_2 as a promoter of oxidation to tetravalent cerium (and so the two-electron pathway model) has gained quite some attention throughout the years [32], especially in the context of Ce-based conversion coatings [52–55, 76], where H_2O_2 is added to the conversion coating baths to accelerate and promote the formation of a Ce-based surface oxide due to its strong oxidising power.

Despite explanatory, further research is, however, needed to corroborate this mechanistic model, so that the essence of corrosion inhibition provided by Ce(III) can be better understood. The potential formation of insulating cerium oxide layers, which inhibit the charge transfer at the metal-solution interface (thus corrosion events), justifies the perennial research interest towards Ce(III) compounds as corrosion inhibitors.

1.2.4 Current limitation(s) of Ce(III) inhibitor

In spite of the extensive state-of-the-art on trivalent cerium compounds used as corrosion inhibitors (and especially for the inhibition of AA 2024-T3), a performance-related problem that still seems to be little addressed in literature concerns their reversibility. This happens because most of the studies so far have been focusing on systems where cerium is constantly available (*e.g.* continuous immersion in Ce(III)-containing electrolytes, or coatings containing cerium salts exposed to an electrolyte). It is, indeed, well known that Ce inhibitive layers passivate and protect the metal surface as long as a constant supply of Ce^{3+} ions from the environment is provided. However, less is known about what happens to these (naturally formed) layers once they are re-exposed to a corrosive electrolyte (*i.e.* without inhibitors). Despite being scarcely addressed, such topic could be of great relevance in coating applications, where the durability (thus irreversibility) of protective properties might be limited by the actual availability of cerium (or other inhibitors) from the coating itself.

A definition of "irreversibility" for corrosion inhibitors was provided by P. Visser *et al.* [77]. With such term it is mainly meant the ability of corrosion inhibitors to passivate the metal surface and, once passivated, to retain their protective properties even when the concentration of the corrosion inhibitor decreases. From this definition, irreversibility of inhibitors involves (ideally) a permanent interaction between the inhibiting species and the corroding metal, thus becoming an important parameter to achieve a long lasting protection of the metal. From literature, however, little is known about the type of interaction between Ce layers with the inhibited surface. The formation mechanism of these layers, which relies on an environmentally-triggered precipitation of Ce(III) species on the alloy surface (*e.g.* changes in pH), does not completely account for the formation of stable bonds and/or a certain affinity between cerium and the metal surface.

The understanding of these aspects is of crucial importance in order to overcome the current limitations of Ce(III)-based inhibitors and, above all, find strategies to improve the long-term protective properties of Ce(III) passive layers. This will be the focus of the thesis work.

1.3 Scope of the thesis

The scope of this thesis is to investigate and characterise the inhibition properties provided by Ce(III) inhibitors on AA 2024-T3. In particular, focus of this thesis will be to study the stability of Ce(III) passivation layers after re-immersion in non-inhibited solutions, in order to simulate conditions where Ce(III) supply is insufficient. Moreover, a possible strategy to improve this property will also be studied, namely by exploiting the interaction of Ce-inhibition layers with different organic molecules. $Ce(NO_3)_3$ was employed in this research as the model inhibiting Ce(III) salt.

The goal of the thesis can be summarised by the following question:

Can the stability and protection offered by Ce(III) inhibitive layers on AA 2024-T3 be improved?

An appropriate answer to this question was found by addressing a subset of fundamental key points:

- The first aspect addressed was related to *validating the use of highly spatial and temporally resolved optics coupled to electrochemical signals* as a feasible method to study (in)stability of passivation layers. The validation of the technique proposed helped to better understand electrochemical signals derived from the corrosion and inhibition processes of AA2024-T3.
- The second aspect was related to *understanding the inhibition of AA 2024-T3 under immersion in Ce(III)-electrolytes*. Evaluation of inhibition properties and its dissimilarity to corrosion helped in consolidating the knowledge about Ce(III) inhibition mechanism, as well as defining the requirements for subsequent investigation of (in)stability.

- The third key aspect was related to *understanding the reasons behind Ce(III) reversibility*. Provided that cerium inhibition is reversible upon re-immersion in sodium chloride solutions, shedding light on the causes of such reversibility would be helpful to identify the further actions that should be taken to improve Ce(III) inhibitory power and stability.
- The fourth aspect was related to *understanding the interaction between Ce(III) passivation layers and organic molecules for the fulfilment of Ce(III) irrevesribility*. This aspect was helpful to find an answer to the main research question, but also to unveil a new potential approach to study synergistic effects between multiple corrosion inhibitors.

1.4 Thesis outline

The thesis is structured as follows:

Chapter 2: The experimental setup to perform real-time optical and electrochemical analysis is presented, together with the samples required for such experiments and the procedure to collect and process the data. This introduction is necessary to guide the reader through the results that will be presented further on, primarily based on this technique. The type of information provided by this method is given by running corrosion tests on AA 20204-T3 in saline solution. Initial corrosion studies on this alloy helped to reveal in real-time the relation between the spatio-temporal detection of electrochemical events and the composition of the alloy, as well as to understand the requirements needed for further studies with corrosion inhibitors.

Chapter 3: As Chapter 2 proves the potential of the optical-electrochemical method, Chapter 3 focuses on understanding inhibition processes with the same technique. Therefore, the same setup and methodologies described in Chapter 2 were tested on AA 2024-T3 immersed in electrolytes containing $Ce(NO_3)_3$ at different concentrations. Studies with different inhibitor-concentrations are demonstrated to provide different degrees of protection to the alloy, but overall offering the same underlying inhibition mechanism. Finally, together with the protection supplied by $Ce(NO_3)_3$, its loss in protection after re-exposure to non-inhibited solutions is also studied by means of optics, electrochemistry and localised electrochemistry.

Chapter 4: This chapter explores how organic compounds can stabilize Ce-based passivation layers, thus enhancing their corrosion protective behaviour. In particular, the problem of Ce(III) stabilisation is tackled by looking at the interaction between cerium and three different organic compounds: sodium alginate, phytic acid and 2,5-Dimercapto-1,3,4-thiadiazole.

Chapter 5: The last chapter summarises the research project and the most important conclusions from each chapter. An answer tot he research question is looked for. Further suggestions for future research in the field are also proposed in here.

Chapter 2

Studying AA 2024-T3 corrosion in real time: an introduction to the opto-electrochemical setup and method

In this chapter, the experimental setup to perform real-time optical and electrochemical analysis is presented, together with the samples required for such experiments and the procedure to collect and process the data. This introduction is necessary to guide the reader through the results that will be presented here and in the following chapters using this analysis protocol. Validation of the information provided by this method is given by running corrosion tests on AA 20204-T3 in saline solution. Opto-electrochemical corrosion data obtained for AA 2024-T3 were compared to the other studies available in literature, so that the localised corrosion events typical of this alloy could be recognised. Initial corrosion studies on this alloy helped to reveal in real-time the relation between the spatio-temporal detection of electrochemical events and the composition of the alloy, as well as to understand the requirements needed for further studies with corrosion inhibitors

2.1 Introduction

From the previous chapter (section 1.1.1), it is clear that corrosion is essentially an electrochemical process, which can be, therefore, characterised with electrochemical methods. In addition to that, section 1.1.2 showed that some corrosive phenomena, especially in AA 2024-T3, develop with a certain time-dependency, which is difficult to grasp from electrochemical characterisation on its own. The common approach that has been adopted so far by many corrosion scientists is to combine electrochemical characterisation with other types of inspection, like imaging or surface analysis after immersion, in order to support the interpretation of the collected electrochemical data.

Reconstruction of the corrosion time-evolution can be done in two ways: i) extracting one corroding sample from the electrolytic solution at different immersion times in order to do the desired analysis, thus re-immersing the same sample in the electrolyte afterwards; or ii) analysing multiple samples at different immersion times and averaging the results. The first approach is disadvantageous since the intermediate removal from the cell not only causes the loss of time-dependent information about the ongoing electrochemical process, but, in some cases, it may also change and compromise the actual electrochemistry of the surface. The second approach, on the other hand, introduces the risk of a higher scatter in the results with scarce reproducibility due to the different composition and/or distribution of second phases between the various samples. A more appropriate type of approach would consist in coupling electrochemcial measurements and other analytical techniques together and run them in parallel, in order to enable a real-time and *in situ* inspection. In this way, correlation between the surface changes and the elctrochemical events (that are responsible for these changes) can be found more easily, thus avoiding the obstacles mentioned above.

The same idea of matching electrochemical characterisation with other *in situ* analytical techniques has actually turned out to be useful in many fields of application. H. D. Song *et al.* [78], for instance, showed the feasibility of coupling dark-field microspectroscopy with electrochemical analysis, especially with cyclic voltammetry, in order to study catalysis. F. Li *et al.* [79] used *in situ* confocal energy dispersive X-ray diffraction to study electrocrystallization processes during electrodeposition. In the study of D. H. Han *et al.* [80], *in situ* confocal microscopy is employed to investigate the formation of electrochemically generated droplets of 1-ethyl-1-methylpyrrolidiniumbromide for redox flow batteries application.

In the field of corrosion, optical imaging has always attracted great attention among all the possible analytical techniques due to the simplicity and straightforward character of the information provided. Visual inspection and optical microscopy are, indeed, still nowadays highly employed in both industry and research as powerful and non-destructive tools for corrosion inspection and many quality standards actually still rely on visual inspection to judge the safety of a corroded structure. Therefore, optical investigation has always sounded as an appealing option to provide a visible and clear interpretation of the macroscopic changes caused by corrosion. In 1971, T. Tokuda and M. B. Ives [81] were the first ones to propose a coupled optical microscopy-electrochemical type of investigation to study pitting corrosion on Ni single crystals, as well as ploycrystalline Ni. With the years, other research groups attempted to study corrosion phenomena with a combined optical-electrochemical approach, some of these studying pitting of Ni [82], localised corrosion caused by MnS inclusions in steels [83–87], or even inhibition of different nitrate salts [88]. Recent studies by P. Denissen *et al.* also focused the attention on the opto-electrochemical characterisation of aluminium 2024-T3 corrosion [89, 90]. In both of their studies, the authors proposed a novel real-time opto-electrochemical analysis with a very simple experimental setup. In their article [89], the authors managed to couple data from electrochemical impedance spectroscopy (EIS) with optical changes of AA 2024-T3 immersed in diluted NaCl soultions, as well as a series of electrolytes containing both inorganic and organic inhibitors. From the results observed, real-time optical microscopy appeared as a powerful and complementary tool for a clearer formulation and interpretation of electrochemical signals for both corrosive and inhibitive systems. In their following work [90], they corroborated their previous findings by using an upgraded opto-electrochemical setup. Here they demonstrated a substantial improvement of the readability of electrochemical noise siganls thanks to the parallel optical inspection. In particular, deconvolution of noise signal transients in the time-frequency domain, together with an accurate optical analysis of the collected pictures, made it possible to recognize typical recurrent signals over time, which can be representative of certain localised corrosion events of AA 2024-T3.

The present work attempts to establish a coupled opto-electrochemical type of analysis as a useful tool to study not only corrosion, but also inhibition of metal substrates. In order to be able to explain the apparatus and methodologies adopted throughout the research, the rest of the chapter will be dedicated to the description of the opto-electrochemical experimental setup, the preparation of samples, the various supporting techniques and the post-processing data analysis. Additionally, results related to the opto-electrochemical investigation of AA 2024-T3 in Cl^- solution will also be presented as an initial test, given its importance in aircraft manufacturing (see section 1.1). The results presented here will serve as a validation of the technique and analysis protocol, but they will be useful to get a feeling on how the AA 2024-T3 corrosion process evolves on the surface, so that it will be easier later on to assess the inhibition efficiency of Ce(III).

2.2 Experimental

2.2.1 Materials and electrolytes

Commercial bare AA 2024-T3 was supplied by Kaiser Aluminium in 2 mm thick rolled sheets and used as working electrode (WE). Cold curing epoxy resin for sample embedding (Bisphenol A and epichlohydrin, EpoFix Resin) and the respective hardening agent (triethylenetetramine, EpoFix Hardener) were supplied by Struers. Sodium chloride NaCl with purity >98% was purchased from VWR Chemicals and used without further purification. Millipore® Elix 3 UV filtered water was used to make electrolytic solutions.

The electrolytic solutions used in throughout this research were obtained from a basic solution of NaCl dissolved in water at a concentration of 0.05 M (mol L^{-1}). Unless specified, this solution is called "NaCl" and was used for corrosion tests.

2.2.2 Preparation of AA 2024-T3 micro-electrodes

The 2 mm aluminium sheets were milled out into small pillars with a very specific geometry, which can be seen in Figure 2.1. The geometry consists of a 0.5 mm thick base with an area of 4x4 mm^2, from which a pillar of 1.5 mm effective height and 2x2 mm^2 area protrudes. This shape consisting of a bigger (4x4 mm^2) and smaller surface (2x2 mm^2) was designed in such a way that the pillar can be embedded in epoxy resin, with the bigger surface serving as the back electrical contact and the smaller surface serving as the exposed surface (*i.e.* the WE).

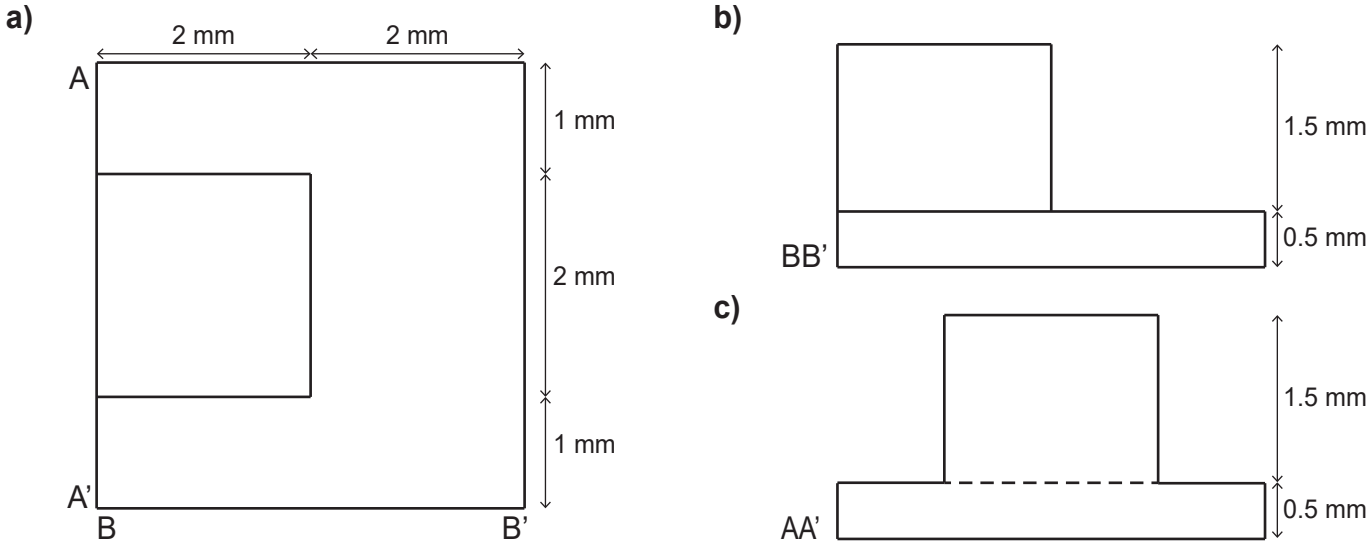

Figure 2.1: Geometry and dimensions of the milled AA 20204-T3 pillars seen from a) top, b) lateral and c) front view.

The steps of the sample preparation are depicted in Figure 2.2. After milling, the pillars were embedded in cold curing epoxy resin as represented in Step 1 of Figure 2.2. At this stage the exposed surface was still equal to 2x2 mm^2 (coloured in blue and indicated by the blue arrow). The resin:hardener weight ratio equal to 25:3 g, as suggested in the specification sheet. The epoxy/hardener mixture was degassed in a vacuum chamber at 0.5 bar for 45 minutes to get rid of most of the air bubbles, then the epoxy was let to cure for 12 h at ambient conditions (*i.e.* 1 bar and 25 °C).

After the first curing cycle, the samples were grinded with SiC paper (grit 320) on two sides of the pillar (as represented in Step 2 of Figure 2.2), in order to further reduce the size of the exposure surface. This process was carried out manually, thus making it difficult to have full control on the final size. As a reference, exposure surfaces were kept in a range between 100x100 μm^2 and 500x500 μm^2 of surface area. The exposed surface is still indicated by a blue arrow in the pictures, despite becoming hardly visible. After obtaining the desired size, the micro-electrodes were embedded a second time in epoxy resin, degassed and cured for further 12 h (Step 2 in Figure 2.2).

Once cured, the back surface of the pillars was first sputtered with a thin 15 nm layer of Au (Step 3 in Figure 2.2), then covered with two stripes of Cu adhesive tape in order to make sure that the electrical contact between the sample and the potentiostat was as high as possible.

Due to the electrical contact between the AA 2024-T3 pillar and the two stripes of Cu tape attached on the back, a galvanic couple with unfavourable anodic-to-cathodic area ratio was created (Cu being the cathode and AA 2024-T3 being

the anode), which could already lead to undesired early corrosion of the exposed surface during grinding and polishing steps. For this reason, a layer of adhesive tape was attached on the big cathodic areas (*i.e.* the Cu tape on the back) in order to limit galvanic corrosion effects during grinding and polishing operations. The exposed surface was then quickly grinded with 1000, 2400 and 4000 SiC paper (approximately 20 seconds for each grit size). After grinding, quick polishing with diamond pastes was performed to obtain 3 μm final roughness (10 seconds approximately due to the corrosiveness of the polishing paste). The sample was sonicated and thoroughly rinsed in ethanol and gently dried with compressed air before analysis. The adhesive tape was removed just before immersion in the electrolyte and the Cu tape was carefully wiped with ethanol to remove any residue of glue on the electrical contacts.

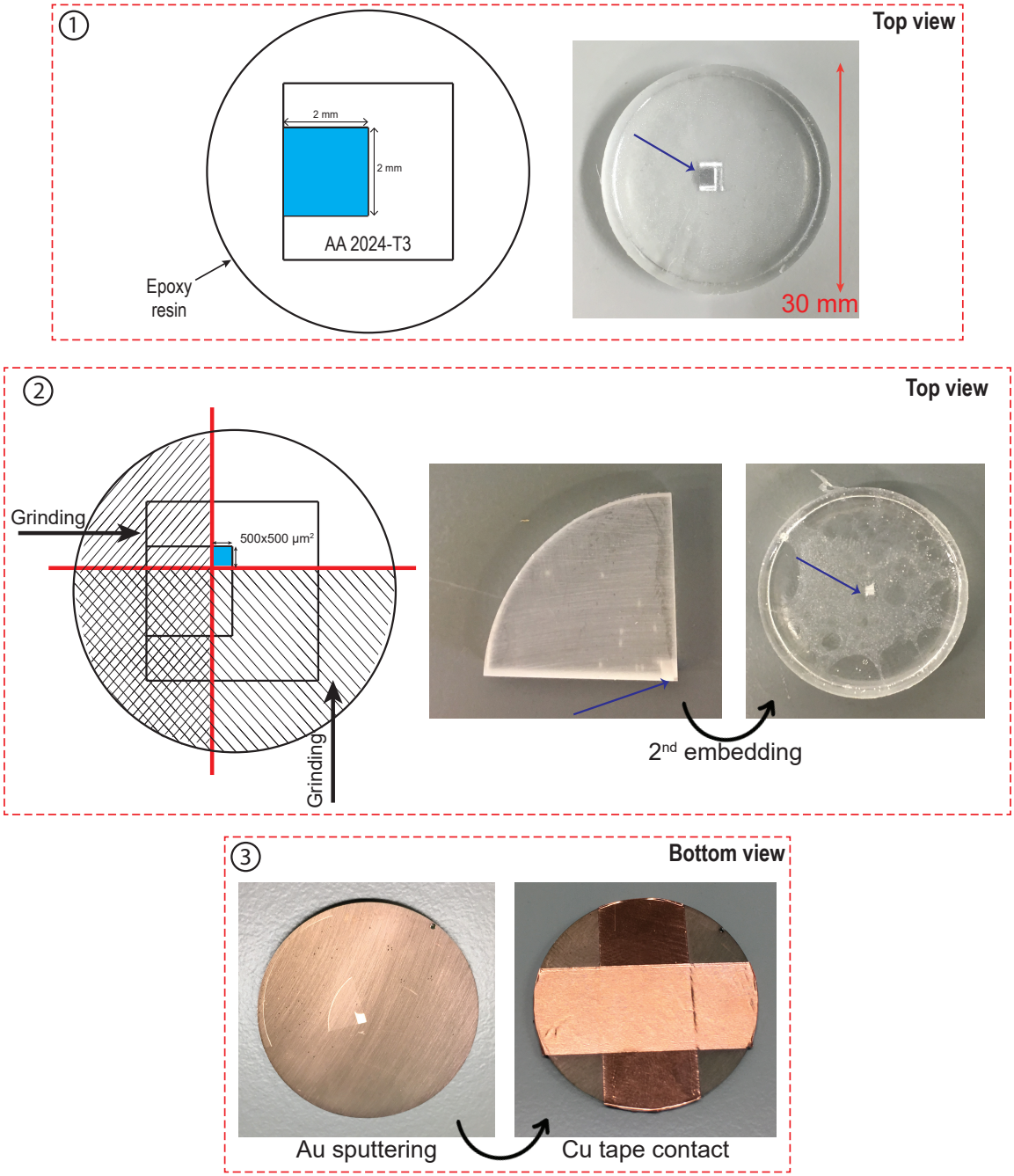

Figure 2.2: Sample preparation steps consisting of: 1) embedding pillar in epoxy resin, 2) analytical surface size reduction and second embedding of the samples in epoxy resin, 3) Au sputtering and Cu tape attachment on the back surface.

2.2.3 SEM before immersion

Before immersion in the electrolytes, scanning electron microscopy (SEM) analysis of the working electrode was carried out on the samples with a field emission scanning electron microscope (JEOL, JSM-7500F) coupled with Energy dispersive

X-ray spectroscopy (EDS). Back scattered electron (BSE) images were recorded so that the distribution of the IM phase on the surface could be localized. To achieve a higher resolution, pictures of isolated areas were taken at higher magnification (*i.e.* 500 X), so that they could be stitched together afterwards to re-create the whole surface. To this purpose, the single images were reprocessed in Adobe Photoshop and automatically stitched together thanks to the "Photomerge" command set in "Reposition" mode. The SEM images were collected with 15 kV of accelerating voltage and 10 μA of emission current. EDS analysis was carried out with the same conditions to identify the IM phase composition. Since SEM-EDS analysis is known to leave some (organic) contamination on the surface, a very quick re-polishing ($\approx$ 3 s) with 3 μm polishing paste was done before starting electrochemical measurements in order to remove these contaminants, but, at the same time, avoiding significant erosion of the just-analyzed IM phase. After repolishing, the sample was again sonicated and rinsed in ethanol, gently dried with compressed air and ready to be immersed in the electrolytic solutions for the opto-electrochemical analysis.

2.2.4 Opto-electrochemical analysis

2.2.4.1 Description of the setup

The opto-electrochemical setup adopted in this research shares the same principle as the one described in [90], but with some variations.

For immersion of samples in electrolytic solutions, a magnetic mount Raman electrochemical flow cell (MM Raman ECFC) was adopted and purchased from Redox.me. Its shape can be seen from Figure 2.3a. In Figure 2.3b, an exploded depiction of the cell is also provided to help the reader understand its complex structure and components. In summary, it consists of: i) two mounts, front and back (labelled as chamber and sample holder respectively in Figure 2.3b), in the midst of which the sample (working electrode) can be placed and kept closed by means of four magnets; ii) a circular copper electrode placed between the two mounts (precisely, between the sample holder and the WE) to allow for electrical contact between the sample and the working electrode clamp connected to the potentiostat; iii) an internal cavity of 4.5 mL inside the front mount, which is meant to be the electrolytic chamber containing the electrolyte; iv) a quartz window serving as a transparent front lid to allow for optical inspection. The electrolytic cell is designed in such a way that 3.5 cm^2 of active area are exposed to the electrolytic solution. However, in the present study, the actual active area of the working electrode was much smaller than this value, as described in section 2.2.2. In Figure 2.3b, some rubber O-rings are also shown and labelled with the general function of guaranteeing sealing and air-tightness of the cell during flushing operations of the electrolytic solutions. Two diametrically opposite plastic vessels (electrolyte inlet and outlet in Figure 2.3b) depart from the front mount of the cell, thus enabling flushing of electrolytes and filling of the chamber. The electrolyte can be filled into the cell by means of a 10 mL syringe connected to one of the two vessels by creating vacuum with a 60 mL syringe connected to the other vessel. Injection of electrolyte with this procedure helped to get rid of air bubbles as much as possible, which can compromise the optical analysis as well as the electrochemistry of the surface. On the sides of the front mount, there are also two holes for the insertion of reference and counter electrodes (RE and CE). For this research, an Ag/AgCl (sat. KCl) was always used as reference electrode, while a Pt wire was used as counter electrode when needed.

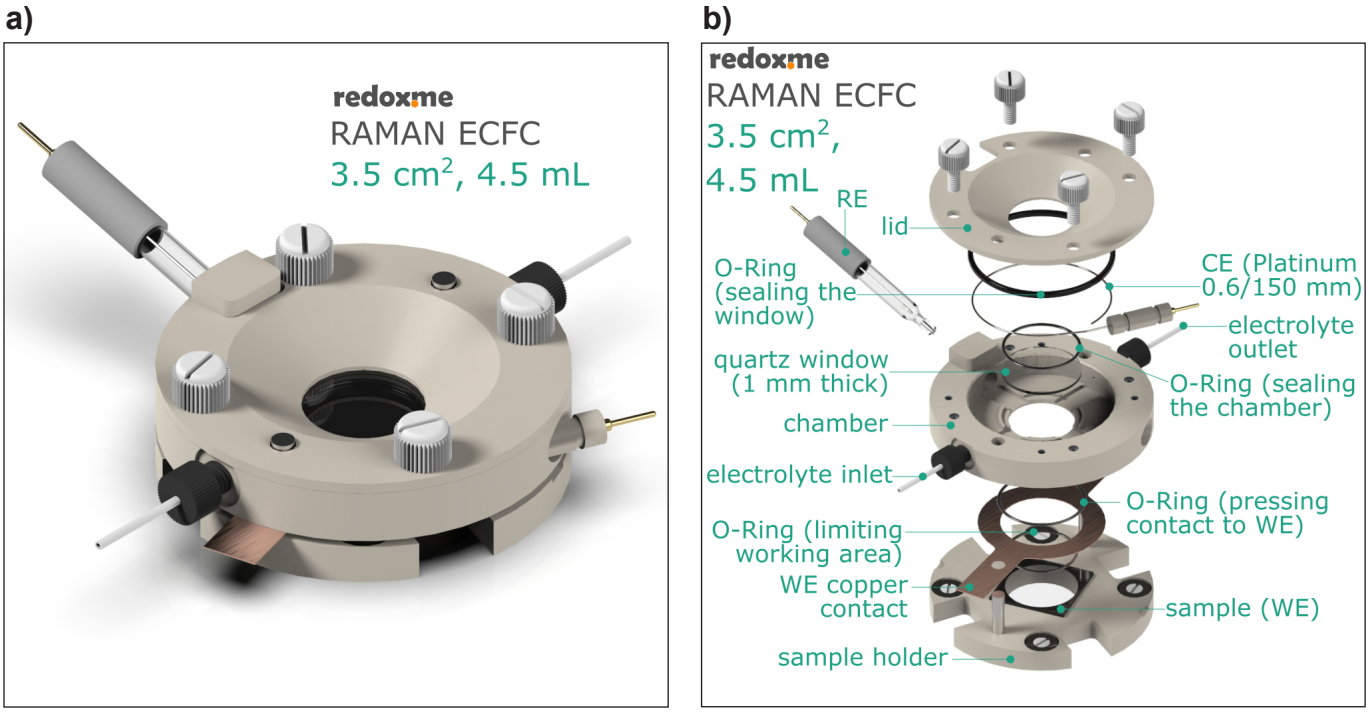

Figure 2.3: a) Representation of the MM Raman ECFC adopted for opto-electrochemical inspection throughout the research. b) Exploded representation of the MM Raman ECFC with all the relevant components highlighted and labelled. Both the pictures were taken from [91].

The optical and electrochemical inspection were carried out with the help of fixed supports assembled on an optical table (ThorLabs) and placed inside a Faraday cage to reduce external electromagnetic interference. A picture of the whole opto-electrochemical setup can be seen in Figure 2.4a and 2.4b from a front and top view, respectively. On one side (*i.e.* the right side of Figure 2.4a and 2.4b), a digital microscope camera was fixed to a support. On the opposite side (*i.e.* left side in Figure 2.4a and 2.4b), an electrically powered stage not only served as a support for the electrolytic cell, but also allowed for translational movements in the y,z directions for sample centering and in the x direction for optimal focusing.

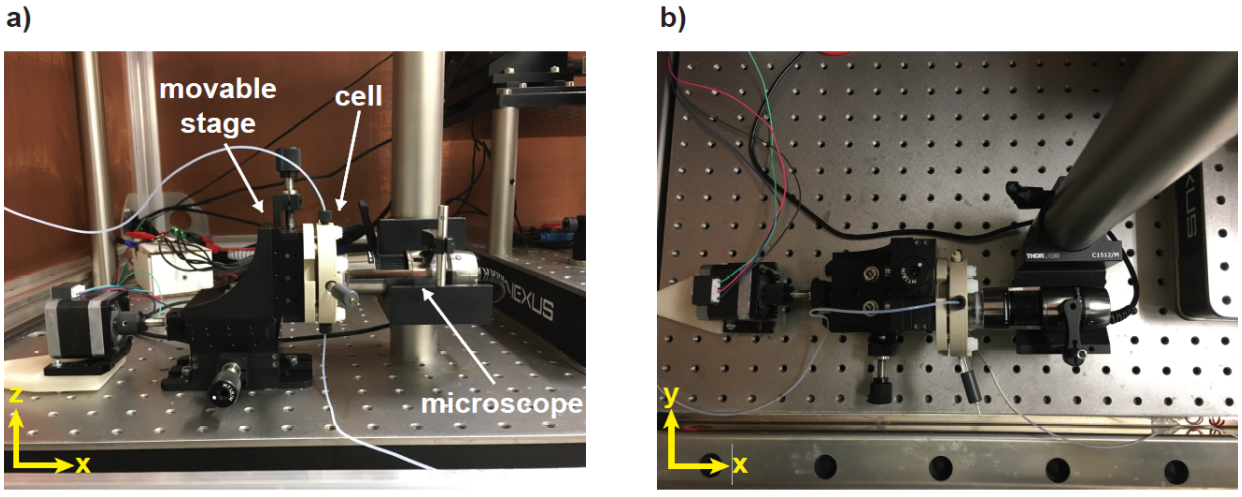

Figure 2.4: a) Front view of the opto-electrochemical setup (in the x-z plane); b) Top view of the opto-electrochemcial setup (in the x-y plane).

2.2.4.2 Real-time optical analysis

As for the optical analysis, images were recorded by means of a high-resolution (5 megapixel, 2592x1944) and high-magnification (415X-470X) digital microscope (Dino-Lite High Magnification, AM7515MT4A) endowed with CMOS sensor. The microscope allowed for two different lightening mode: i) bright field mode (coaxial illumination) and ii) dark field mode (ring of 8 LED lights). In this research, most of the information was extracted using the coaxial illumination. This

mode was selected because it allows for visualisation of surface roughness changes due to pitting and/or deposition of species, thus making it easier to distinguish between different surface phenomena related to corrosion and/or inhibition. Images were recorded via DinoCapture 2.0 software, programmed to record pictures at a certain frequency (typically 1 picture every 10 seconds for corrosion studies and 1 picture every 60 seconds for inhibition studies). The auto-exposure setting was turned off before every measurement and the exposure per second adjusted to a specific value (lx/s) to avoid under or over exposure during the measurement. The pictures were recorded in parallel with the electrochemical test.

2.2.4.3 Electrochemical analysis

Electrochemical potential was chosen as the electrochemical signal to be coupled to the optical data, based on recent work validating the approach [90]. Besides, the electrochemical potential, which represents the electrode's surface thermodynamics, may help further assessment of the system stability.

For the measurement of electrochemical potential, an Ivium Compactstat controlled with the software IviumSoft V2.86 was employed. The electrochemical potential was measured in open circuit condition (open circuit potential, OCP) between the working electrode (AA 2024-T3 surface) and the Ag/AgCl (sat. KCl) reference electrode. The interval time between data points was set to 0.05 s (*i.e.* sampling frequency of 20 Hz) combined with a low-pass filter of 10 Hz (Nyquist frequency for this sampling frequency). The potential range was set to $\pm$ 1 V *vs* Ag/AgCl.

2.2.4.4 Post-processing image analysis

Qualitative and quantitative (optical) image analysis

To be able to give qualitative and quantitative data about the time-dependent macroscopic surface changes, an iterative image analysis was developed. The codes for the analysis were written in such a way that they can be used as macros on ImageJ software. The analysis consisted of four steps mainly, which will be described more in detail in the following lines. The image analysis was also very similar to the one reported in [90] with some minor modifications.

The first step of the image analysis is schematically represented in Figure 2.5. It consists in the conversion of the collected images into 8-bit format of 256 bins (*i.e.* grey-scale), so that the pixels' intensity distribution can be plotted in an histogram as a frequency-distribution plot ranging from bin 0 (black) to bin 255 (white). The distribution of pixels intensity appears in the histogram as a series of peaks, each of them centered at a certain bin corresponding to a certain nuance in the image (see Figure 2.5). The 8-bit converted pictures were then subject to a recursive repositioning process, meaning that each image was repositioned with respect to the initial one by applying planar rigid body rotation and translation, so that all optical effects caused by small movements during the test can be discarded. The equation describing the mapping of coordinates through rigid-body approach is the following and it was described elsewhere [90, 92]:

$$x, y = \{\{cos\theta, -sin\theta\}, \{sin\theta, cos\theta\}\} \cdot \mathbf{u} + \Delta\mathbf{u}. \tag{2.1}$$

In Figure 2.5, the repositioning process is further explained with an example, where a reference image (img_{ref}) and another generic image (img_i), which is almost equal to the reference image, are shown. The two images are characterised by the same features, *i.e.* red rectangle and three "#" markers. The markers in the pictures are reference points pre-defined by the algorithm and they must be present in both pictures, otherwise the algorithm will look for other reference points to successfully achieve the repositioning. It can be noted that the three markers in img_i are rotated and translated compared to img_{ref}. The repositioning algorithm applies rigid-body transformations, so that img_i is repositioned to img_{ref} with the markers as reference points. After repositioning, the images were cropped around the area of interest, *i.e.* the aluminium sample, so that only changes relative to the metal surface are quantified and the final results get normalized to this area.

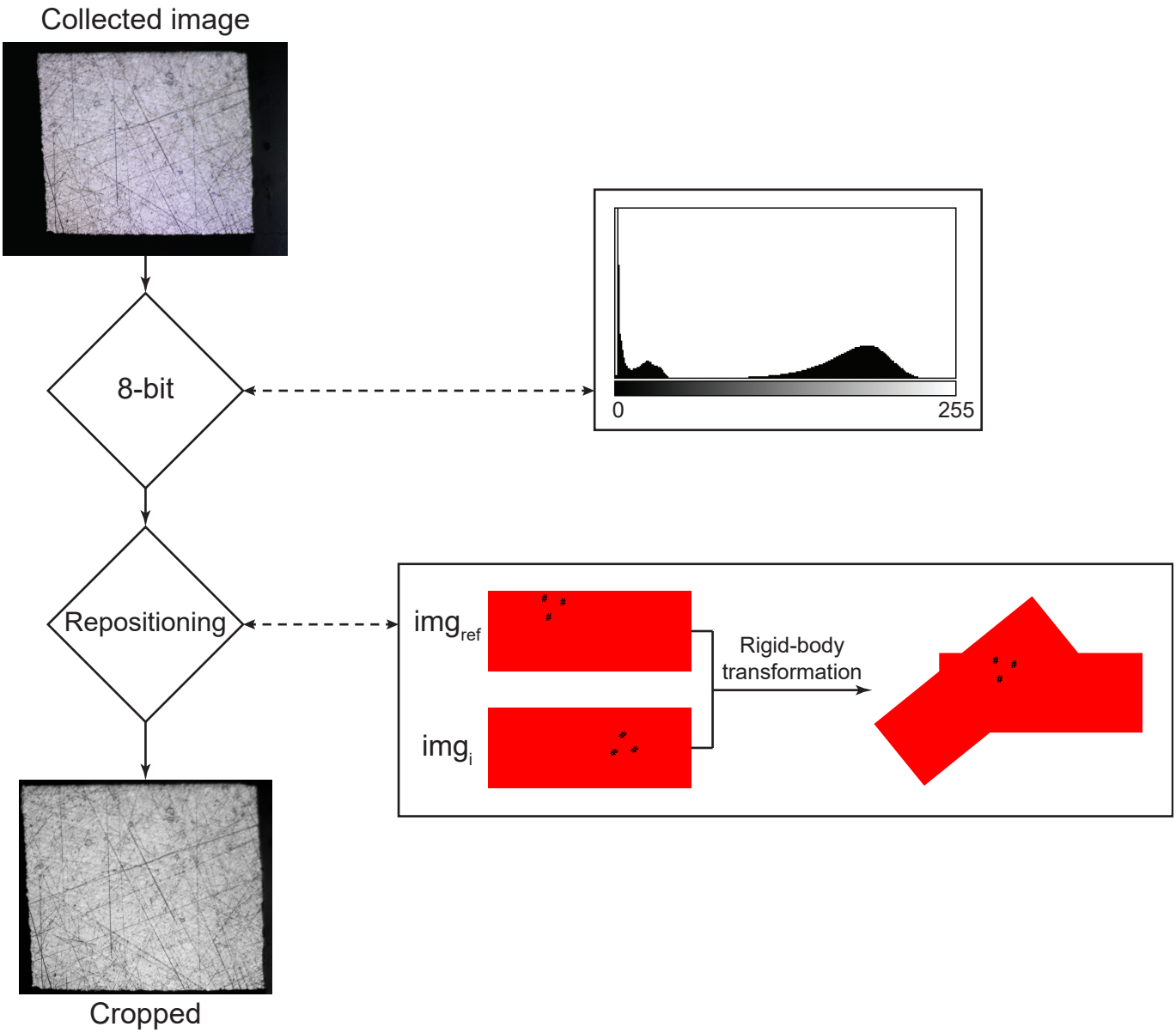

Figure 2.5: First step in the image analysis consisting of converting the images in grey-scale (8-bit), repositioning the images with respect to the initial one, cropping the images around the area of interest.

In the second step of the analysis, the spatio-temporal optical differences between images were evaluated. This evaluation (adopted also in [90]) was carried out pixel by pixel by means of the "Difference" operation in ImageJ. The operation, which is also visually clarified in Figure 2.6 consists of taking the same pixel with the same (x,y) coordinates in both the initial image (img_0) and the n^{th} image in time (img_n), calculating their intenisty (i_0 (x,y) and i_n (x,y), respectively), calculating the difference in intensity and taking the absolute value of the result. The intensity needs to be meant in terms of bin of the optical histogram (*i.e.* 0-255). The equation describing the "Difference" operation is the following:

$$i_{Difference}(x,y) = |i_0(x,y) - i_n(x,y)|. \tag{2.2}$$

In this way, it is possible to distinguish the pixels that have changed in time and the ones that have not, because the unchanged pixels will display a result equal to 0 (*i.e.* black), whereas the changed pixel will give a result > 0 (*i.e.* not black). The more this result discloses from 0, the more the intensity of such pixel has changed in time. In other words, the locations that changed significantly in time, tend to become more white, while the locations that did not undergo changes will remain black. In Figure 2.6, it can be seen how the result between img_0 and img_n displays black areas as unchanged, while the optically-changed areas became brighter. It is important to note that at each time step, the changes were still evaluated with respect to the initial image (*i.e.* between img_0 and img_n first, then between img_0 and img_{n+1}, and so on).

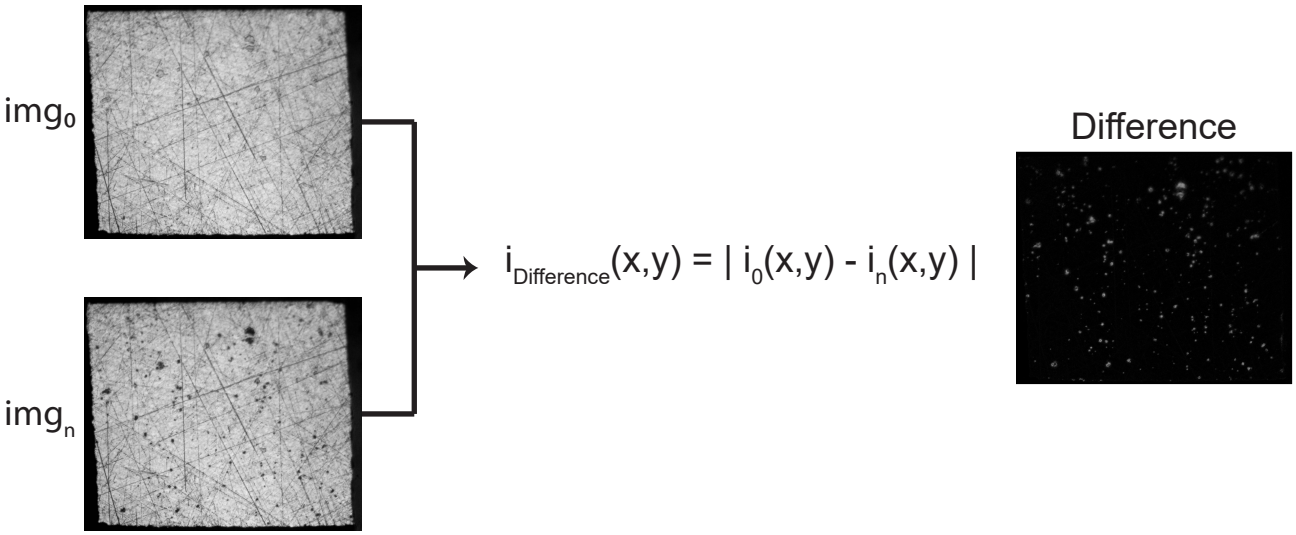

Figure 2.6: Second step in the optical analysis, consisting of the spatio-temporal differences evaluation between images.

The "Difference" calculation enables to: i) visualise the locations that optically changed during the test, ii) quantify the degree of such change per pixel (from the magnitude of $i_{Difference}$). Before counting all the pixels that have undergone changes (to estimate the percentage of changed area), a small correction should be introduced to discern the effectively changed areas from the unchanged ones. The strategy adopted was to re-adjust the lower threshold of the histogram [90]. By increasing the lower threshold of the "Difference" images from 0 (black) to 1, all the unchanged pixels are taken as background. However, a higher value for the lower threshold was set (namely, 30), so that background statistical noise effects are also discarded. These pixels (between 1-30), which in principle have also undergone changes, were discarded because they are unlikely to be related to surface electrochemical events, but rather to the sensitivity of the optical detector. All the pixels with a bin $>$ 30 are, therefore, regarded as effectively changed areas due to electrochemical/surface processes. The whole thresholding process is further clarified in Figure 2.7, where the histogram with a lower threshold set to 30 is shown. This operation, however, returns a binary image (*i.e.* black and white only) with black areas as optically changed and white areas as unchanged. It is desireable for the following step of the analysis to keep the unchanged areas as black, as it will be explained later. For this reason, the "Invert LUT" command was also applied as shown in Figure 2.7. With this command the histogram's grey scale is inverted, so that the black becomes white, and *vice versa*. The result of this process displays binary images with black areas (unchanged in time) and white areas (changed in time).

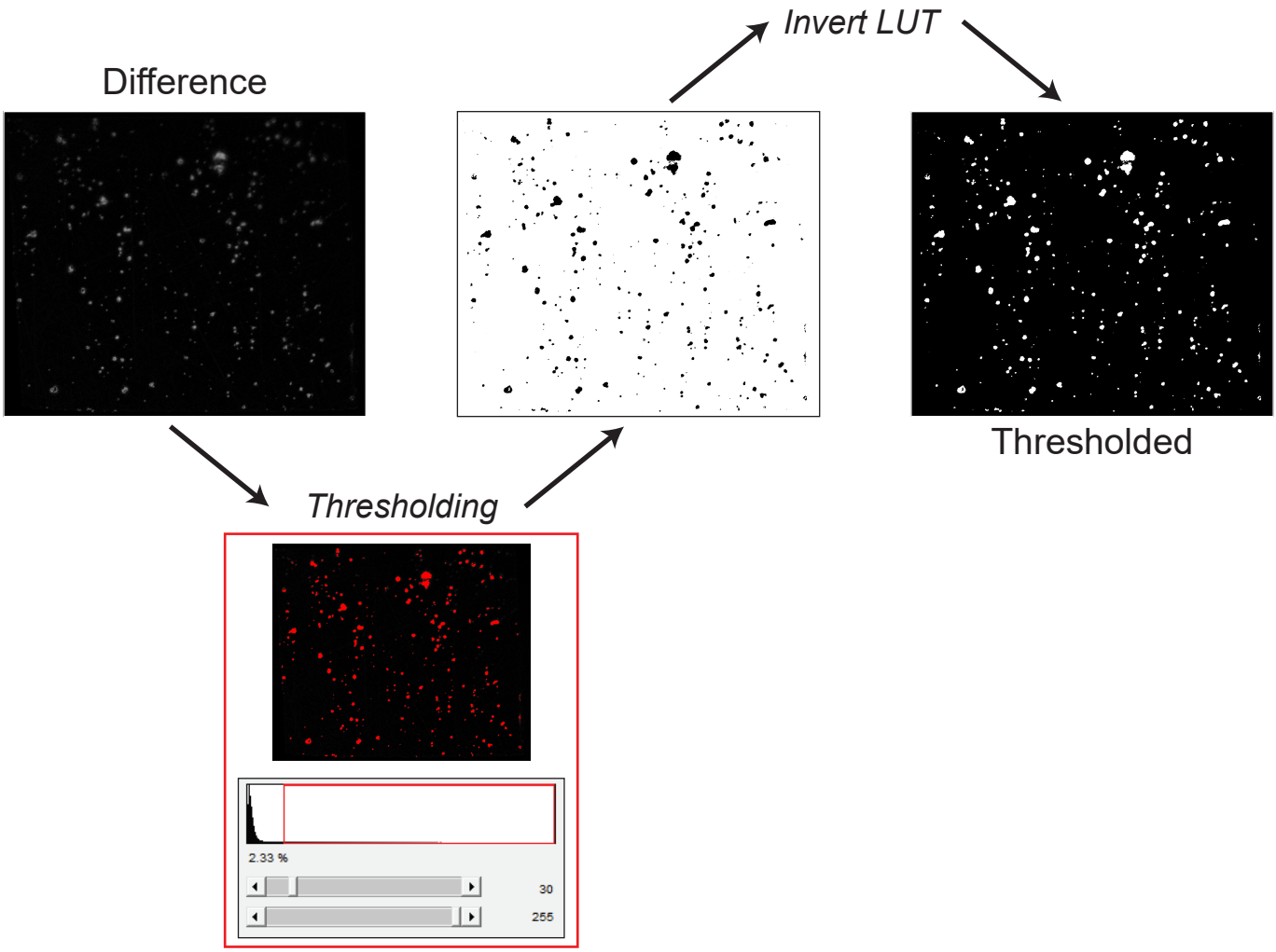

Figure 2.7: Third step in the image analysis consisting of resetting the lower threshold to return a binary image.

From the binary thresholded image, easier counting of the white pixels (*i.e.* changed pixels) can be performed so that a quantitative information about the total changed area, or affected area (AA%), can be provided at each time step according to the following equation, as reported in [89, 90]:

$$AA\%(t) = \frac{N(t)}{N_{TOT}} * 100\%, \tag{2.3}$$

in which N(t) is the number of changed pixels at time "t", while N_{TOT} is the total number of pixels in the images. Such value is calculated for every picture, so that a plot of AA% *vs* time can also be made to see the rate of optical changes.

In order to provide a qualitative description of the optical changes, another step in the analysis was developed and it is schematically represented in Figure 2.8. In this step, the thresholded images ($img_{n\_threshold}$) and the original cropped images ($img_{n\_original}$) at the same n^{th} moment in time were subject to the "Transparent-zero" operation. With this operation, $img_{n\_threshold}$ is first superimposed to the $img_{n\_original}$ (*i.e.* the thresholded image is placed above the original image). Then, all the pixels of $img_{n\_threshold}$ are made transparent, exception made for the zero ones (*i.e.* black or unchanged pixels). The black pixels that do not become transparent have a masking effect on the image underneath, while all the other pixels ($\neq 0$) allow to see the picture underneath through them. In this way, the optical changes of $img_{n\_original}$ are qualitatively evaluated and spatially confined to the white spots of $img_{n\_threshold}$, so that effects caused by background noise or unchanged areas are systematically excluded in the resulting image. The degree of change can be estimated through a grey-scale intensity bar as shown in Figure 2.8. For a better interpretation of the results, the grey-value of each pixel was further transposed to a colour-gradient (Fire-LUT), in which the unaffected pixels are coloured white and the highly affected pixels are coloured dark purple. It was shown in [89] that this colour scale is (in a first order approximation) helpful in the association process of a certain nuance to a certain surface feature, thus discerning between corrosion pits or oxides.

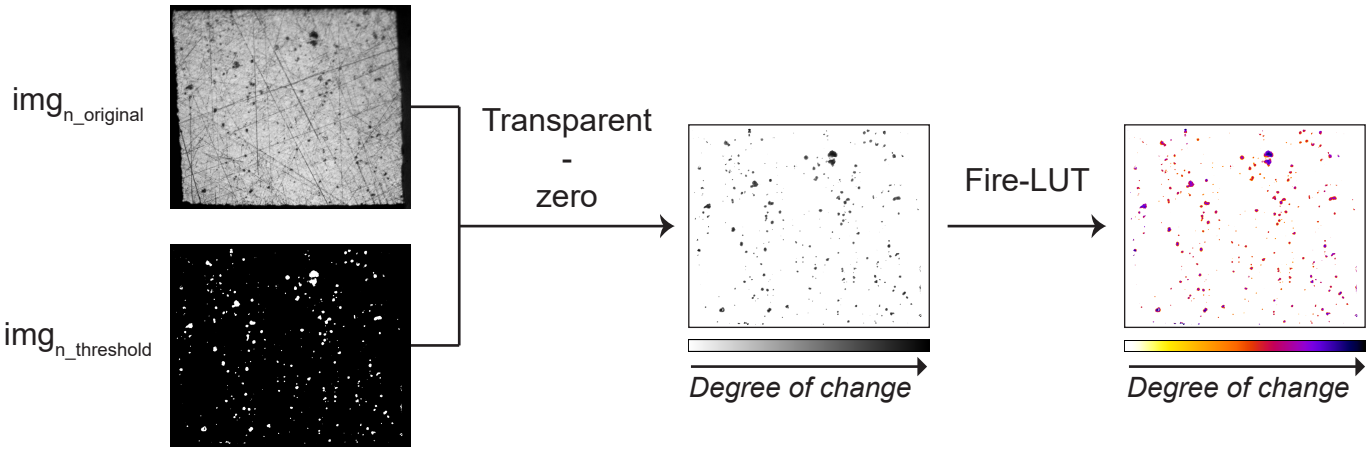

Figure 2.8: Fourth and final step of the image analysis consisting of a systematic background removal and qualitative evaluation of the optical changes.

Identification of IM phase

The SEM-BSE images, collected as described above, enable to make a distinction between the Al matrix (dark) and the Cu-rich IM phase (bright) on the working electrode's surface, because of the higher content of heavy elements (like Cu) in the IMs compared to the matrix. However, it is also desirable to know where this IM phase is located when the corresponding optical images are analysed. For this purpose, the SEM-BSE pictures needed to be fitted to the optical images first. In doing this, the software Adobe Photoshop was employed and the procedure is schematically shown in Figure 2.9. The SEM-BSE image was first overlapped to the optical image (one of the repositioned and cropped optical images) and rotated accordingly so that both the images have the same spatial orientation (Step 1). Then, the opacity of the SEM-BSE image was decreased sufficiently ($\approx$ 50%), so that contours of the optical image underneath were made visible as well (Step 2). The "Warp transformation" mode was then applied to the SEM-BSE image above. With this command, the software defines a grid of control points on the SEM-BSE image. These points can be dragged independently from one another, resulting in a distortion (*i.e.* warpage) of the original image. With this method, the SEM-BSE image was manipulated accordingly until a good fit with the optical image was achieved. Figure 2.9 provides an example of the warp transformation, where the distortion of the SEM-BSE image was exaggerated to help the reader better understand this concept. Warping of SEM-BSE images was necessary to find a good fitting with the optical ones, which could not be found by simple rotation/translation. This happens because of the different curvature of images as a consequence of optical effects (like the curvature of lenses, for example), a non perfect flatness of the surface during SEM and/or optical analysis or maybe even the stitching procedure of SEM images discussed above. The opacity of the SEM-BSE picture was finally increased again to obtain an optically-fitted SEM-BSE image (Step 3).

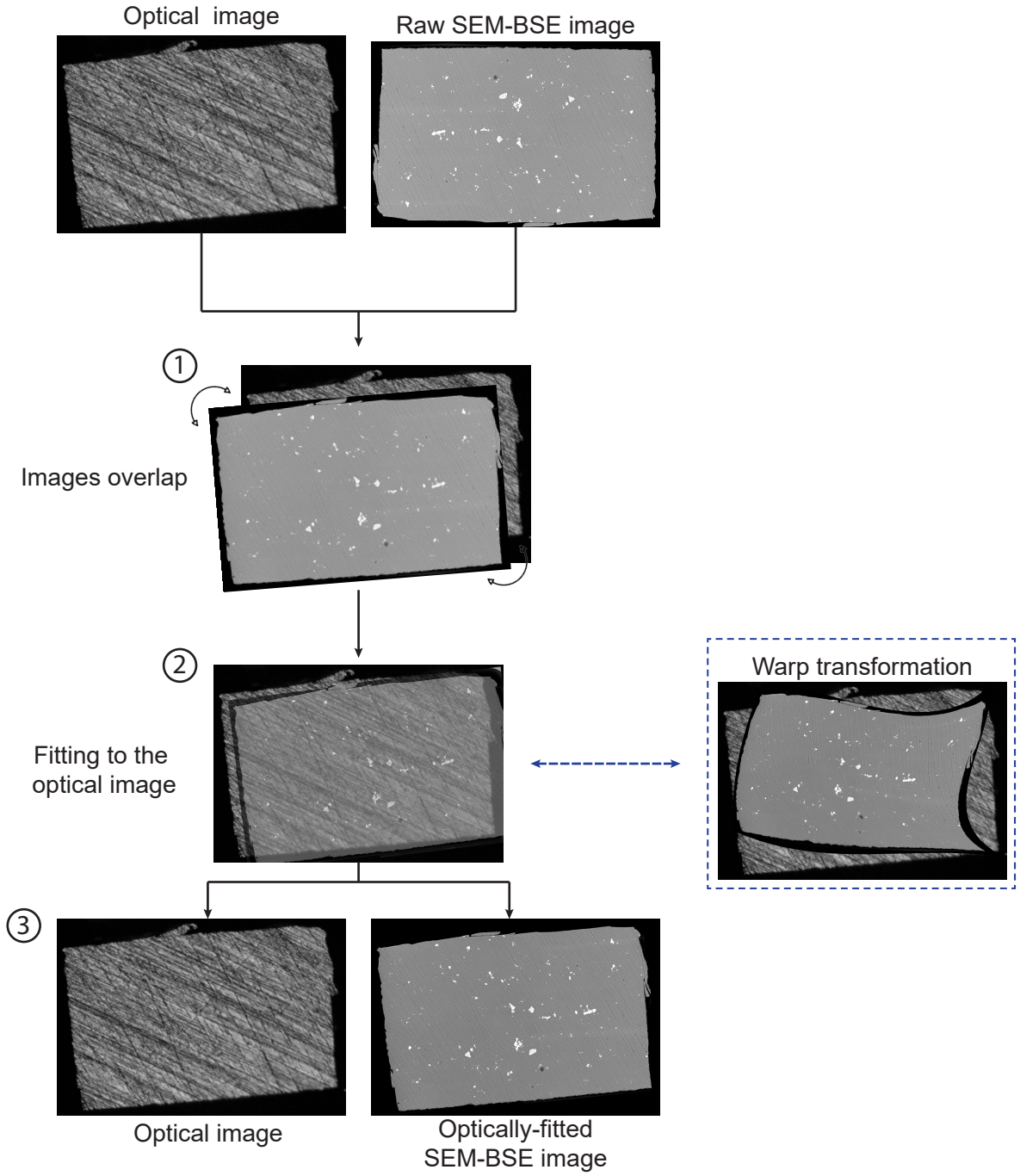

Figure 2.9: Schematic representation of the procedure followed to fit the SEM-BSE images to the optical ones.

As for the identification of the IM phase, the software ImageJ was employed to optically isolate the IM particles from the rest of the Al matrix. In this regard, the SEM-BSE image was first converted to an 8-bit format of 256 bins (*i.e.* grey-scale, bin 0 = black and bin 255 = white, as described above). An example of the 8-bit histogram for a typical SEM-BSE image is shown in Figure 2.10. It can be seen that four different peaks of different intensity appear in the histogram and each of them can be associated with a certain nuance in the image analysed. In order to clarify the association of these peaks to the respective regions in the SEM-BSE image, the histogram was divided in 4 bins and each of them was given a certian colour. The bins were taken in such a way that the 4 peaks were separated from each other. The lowest bin (yellow), which entails the peak centered at 0, highlights the black background of the SEM-BSE image. The second lowest bin (magenta) highlights the epoxy matrix surrounding the sample. The blue bin entails the most intense gaussian peak and highlights the (abundant) Al-matrix. Finally, the red bin highlights the brighter IM phase.

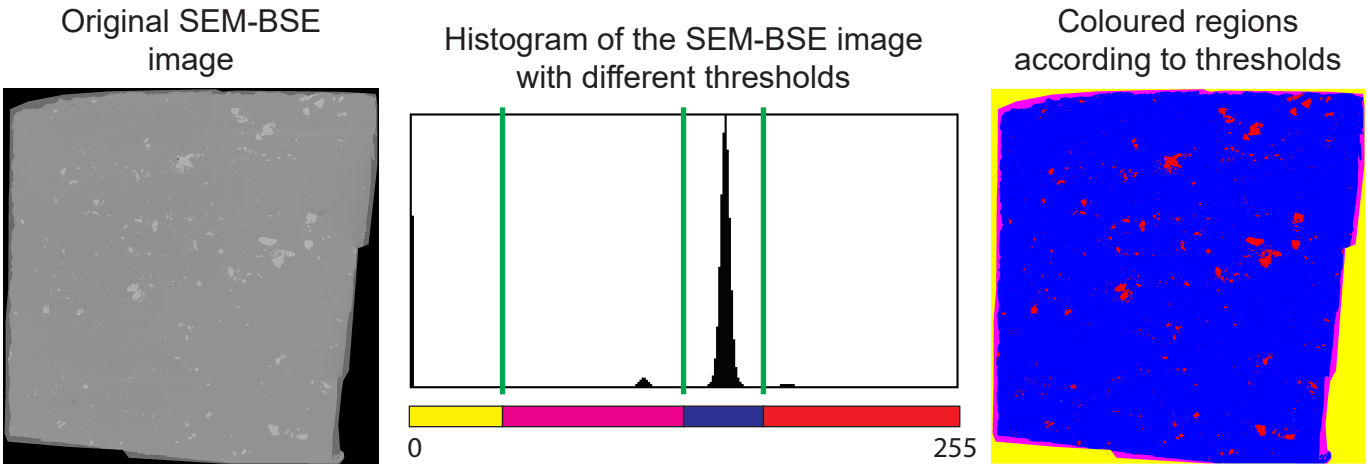

Figure 2.10: Typical 8-bit histogram for an AA 20204-T3 SEM-BSE image, consisting of four peaks. The peaks were separated from each other and assigned a colour which highlights specific regions of the SEM-BSE image.

In a similar way as the one described above, thresholds can be assigned within the 256 bins of the histogram, so that only specific areas corresponding to certain peaks can be isolated from the rest. The schematics of this process is depicted in Figure 2.11, where the lower threshold (LT) and upper threshold (UT) were set to values such that the background, epoxy matrix and Al matrix peaks resulted below the LT. The outcome of this "thresholding" process is a binary image (only black=0 and white=255 pixels, see Figure 2.11), in which the black spots are representing the IM particles and the white area is comprehensive of the Al matrix + epoxy matrix + background.

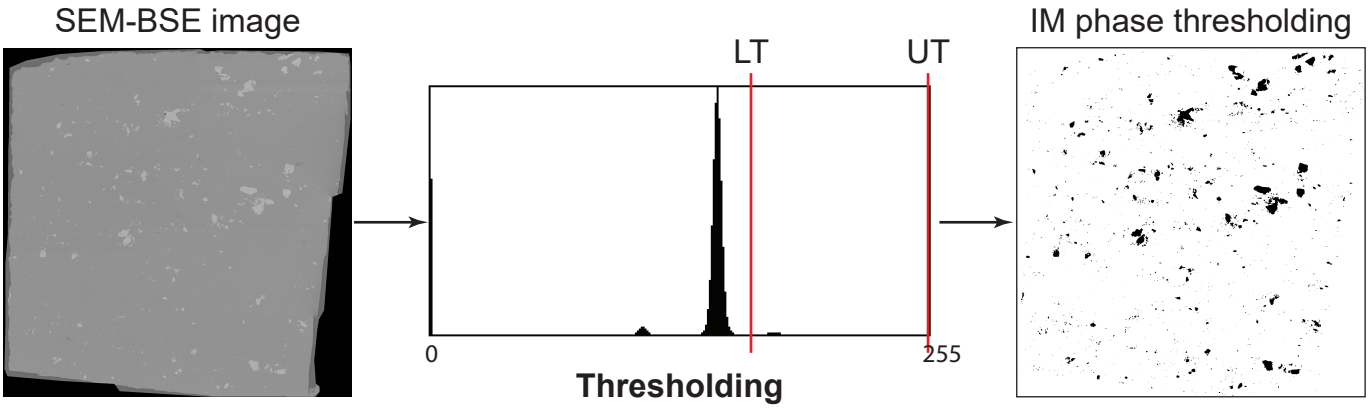

Figure 2.11: Schematic representation of the IM phase thresholding explained with the 8-bit histogram.

The black IM particles of the obtained binary image were subject to the "Fill holes" command, aimed at filling the remaining white pixels left behind within the boundaries of the same particle. After this, the particle analysis based on size (pixels^2) and circularity of particles was carried out on ImageJ. This analysis allows to recognise clusters of black pixels in the binary image as singular entities and denote each of them as a particle. All the particles are counted and listed, as long as they satisfy the imposed constraints in size and circularity. In order to identify all the particles in the image, no constraints in size and circularity should be taken. However, imposing no constraints in size might introduce some errors, because very small clusters of pixels (*i.e.* 1-2 pixels^2) are also counted, despite being unlikely to actually represent active IM areas. Therefore a lower constraint of 10 pixels^2 was chosen instead, as it seemed to be a good approximation to identify adequately the distribution of IM particles across the surface. The result of the particle analysis is displayed on the image as a contour around each of the identified particles, which was then given a certain colour depending on the composition determined with EDS analysis. Figure 2.12a and 2.12b, as an example, represent the raw SEM-BSE image of a sample's analytical surface and the same surface with the IMs yellow contours in evidence, respectively.

The contours of the IM particles can be saved in a ROI (*i.e.* Region of Interest) file so that it can be re-opened and overlapped to the optical images as well (see Figure 2.12c), thanks to the previous fitting explained in Figure 2.9. Although

the fitting procedure is not perfect and may introduce some inaccuracies, it represents a good approximation for localising the IM phase on the optical images as well.

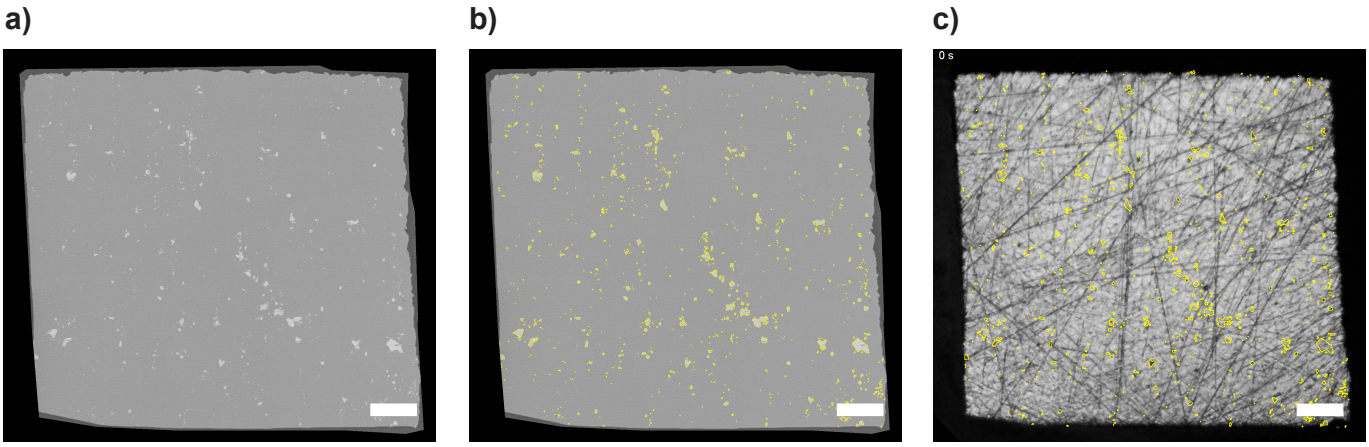

Figure 2.12: SEM-BSE image of an AA 2024-T3 surface a) without and b) with IMs yellow contours as a result of the particle analysis. c) Optical image with the (fitted) IMs overlays in evidence. The scale bar in all images is 50 μm.

2.3 Results and discussion

As an initial test, aluminium alloy 2024-T3, prepared as described above, was exposed to a 0.05 M NaCl solution to monitor its behaviour under immersion condition. Before immersing the sample in the saline electrolyte, SEM-EDS analysis was performed, so that the IM particles could be located on the surface and their composition be determined. For a higher accuracy of EDS analysis, only the bigger IM constituents were analysed (*i.e.* > 5 μm). Depending on their composition, the EDS-analysed particles were assigned a certain colour (see Figure 2.13a as an example). Three phases containing Cu were detected: i) a Mg rich phase, also known as S phase, which was assigned a blue contour, ii) a FeMnSi rich phase, which was assigned a green contour and iii) a Fe-Mn rich phase, which was assigned a red contour. The EDS spectra for each of these phases are shown in Figure 2.13b. θ phase (Al-Cu with no further alloying elements), which has been reported elsewhere as a recurrent phase in 2024-T3 [14], was not detected in these samples. Although a more diversified range of compositions is believed to exist within each of these groups of IMs, a classification similar to the one proposed in [9] was also employed here.

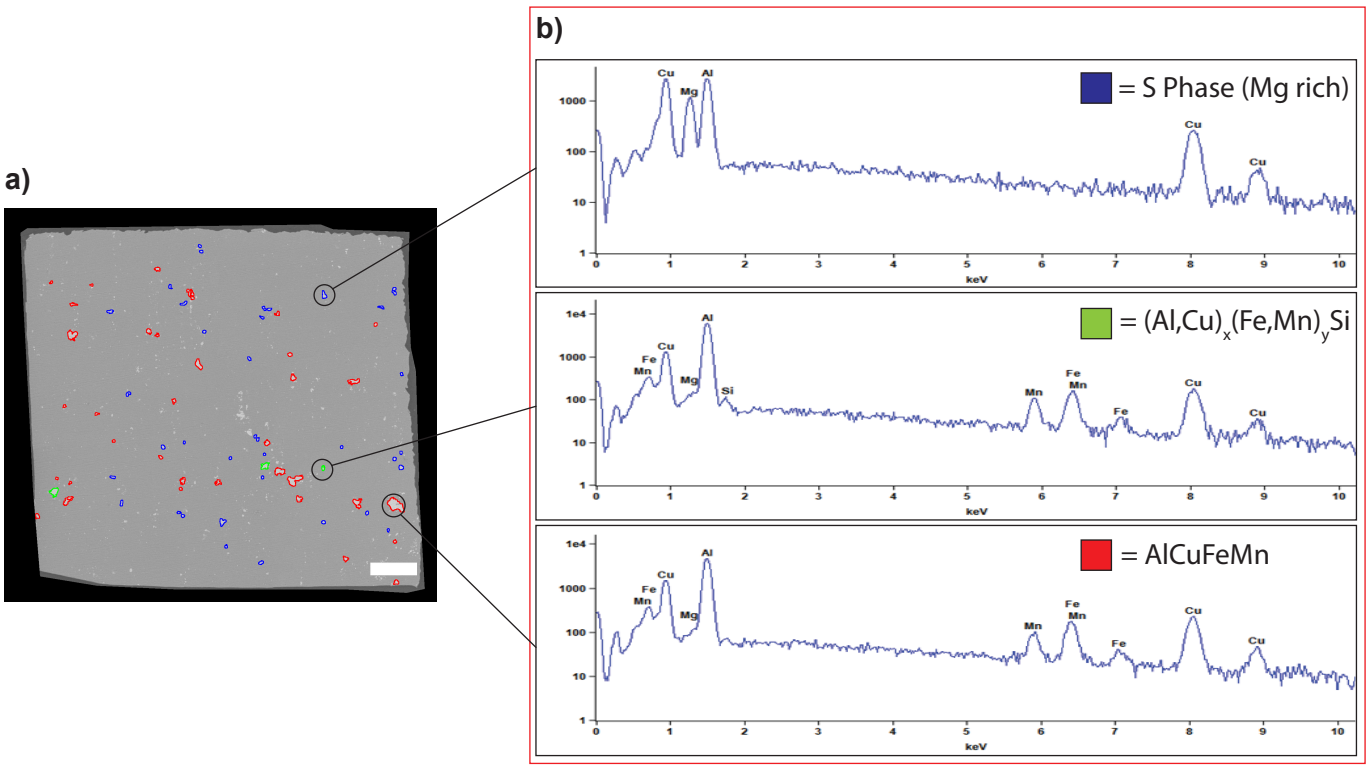

Figure 2.13: a) SEM-BSE image with the EDS-analysed IMs in evidence. The colour of the overlays represents the composition of the particles. b) EDS spectra of three model IMs belonging to three different compositional families: blue = S phase, red = AlCuFeMn and green = $(Al,Cu)_x(Fe,Mn)_ySi$. The scale bar in the picture is 50 μm.

Once the IM phase distribution across the surface was known, corrosion of 2024-T3 was tested with opto-electrochemical analysis. Samples were immersed for 3 hours (*i.e.* 10800 s). The opto-electrochemical data were recorded throughout the 3 h, but for the sake of clarity the data are reported in Figure 2.14 and 2.15 for the first 2000 s and after 2000 s, respectively. Together with the OCP fluctuations, the trend of AA% *vs* time was also plotted as a red line (Figure 2.14a and 2.15a), which quantifies the total percentage of degradation with time, as well as the rate of optical changes. The optical images, recorded in parallel with the electrochemical signal, are reported in Figure 2.14b and 2.15b, respectively, for 6 different immersion times: 0, 100, 600, 1800, 3600 and 10800 s. Both the original (row 1) and processed (row 2) images are shown. It is important to note that the optical images of Figure 2.14b and 2.15b do not show the entire surface of the working electrode, but they were cropped around a few representative IM particles, so that a clearer evaluation of the optical changes could be made. On both the original and processed images, the contour of EDS-analysed IM particles was overlapped in order to qualitatively evaluate the changes undergone by the IMCs. The colours identifying the composition are specified in the legend. The OCP signal from Figure 2.14a and 2.15b shows three different regimes, therefore the results will be presented according to the temporal transition from one regime to the other:

* **0 – 200 s**: In the first 200 s of immersion, Figure 2.14a shows a steady increase of OCP from -0.63 V (*vs* Ag/AgCl) to -0.46 V (*vs* Ag/AgCl) accompanied by a limited amount of affected area ($\approx$ 1%). The original optical image at 100 s (Figure 2.14b) does not seem to show many differences from the beginning. However, the image treated with the designed protocol at the same time reveals that a small amount of localised optical changes has occurred only inside the blue particles (as indicated by the arrows), which represent the S phase. These changes do not have high intensity (red in the colour bar), but they seem to be well confined to the S phase, while the other IMs and the Al matrix are still unaffected (white).
  An analogous OCP trend was observed in the work of P. Denissen *et al.* [90] for similar immersion times. In this study, this stable increase of OCP was ascribed to local anodic and cathodic processes on the IM particles leading to, amongst others, de-alloying of copper-rich S-phase. The AA% value reported in [90] (3-4%), however, was higher than the one observed here (1%), but this difference might be related to the substantial difference in size of the immersed 2024-T3 surface (2x2 mm^2 in [90] *vs* $\approx$ 400x400 μm^2 in this work), which might imply a different number density of exposed IM particles. Localised optical features spread across the exposed surface appeared also in [90] at this stage of immersion, but a relation of these features with the IM phase composition was not proposed due to the lack of an IM composition analysis prior to immersion as performed in this work. The results shown in Figure

2.14, suggest that onset of electrochemical activity can be optically observed within the first 100 s of immersion already. Preferential activity confined to the S phase can be revealed with the optical analysis, underlining a relation between the IM phase composition and its electrochemical behaviour. The selective and localised attack suggests that S phase dealloying might be the dominant process of the first 200 s, in which less noble elements (like Mg and Al) are dissolved, while Cu-rich remnants are left behind. The overall Cu-enrichment of the surface makes the S phases more cathodic leading to more positive OCP values.

* **200 – 700 s**: After 200 s, the OCP in Figure 2.14a becomes unstable and fluctuations, also known as "transients", start to become visible in the signal. Transients are characterised by fluctuations covering a range of $\approx$ 200 mV with individual events shaped as spikes of large amplitude. The AA% keeps growing linearly between 200 and 700 s from 1% to 2.5% (constant rate of $\approx$ 0.003 %/s). In Figure 2.14a, a green dotted line centered at a value of 2.26% was additionally plotted, indicating the optical surface percentage of IMs exposed to the electrolytic solution. It is interesting to observe that the plot of AA% curve intercepts the IMs-green line at a time of approximately 600 s, which is very close to the transition time to a different OCP regime (*i.e.* 700 s). The optical images in Figure 2.14b show that all the big IMCs of known composition have been optically affected at 600 s (both in the original and processed images) and the extension of degradation is still confined to the IM boundaries.
  The appearance of instability in the electrochemical noise has been previously ascribed to the appearance of pitting corrosion in Al alloys [21, 90, 93]. As discussed in section 1.1.2.1, the nucleation of (metastable) pits has also been associated to the initiation of trenching around the IM phase [18]. Therefore, instabilities observed after 200 s in the OCP signal of Figure 2.14a can be related to the nucleation and growth of corrosion pits as well. A neat distinction between metastable and stable pitting events (as described in [90]) is not clear from this OCP signal, perhaps due to the small exposed surface leading to a superposition in time of the two events. At 600 s, the optical images showed all the big IMCs to be affected and the AA% also reaches a value equal to the optical percentage of exposed IMs. The proximity of these events in time (600 s) to the transition to another OCP regime (700 s) suggests that nucleation of pits and trenching around the single IMs might still be dominant processes between 200 s and 700 s, leading all the IM phase to be optically attacked. The delayed attack of IM phases other than S phase (*i.e.* red and green), which becomes visible only after the appearance of OCP intabilities, might indicate their cathodic character.
* **700 – 10800 s**: After 700 s, the OCP signal (Figure 2.14a) fluctuates in a range of $\approx$ 50 mV but overall stabilises around an average value ($\approx$ -0.5 V *vs* Ag/AgCl). This trend of OCP will be pretty much constant until the end of the immersion (*i.e.* 10800 s, see Figure 2.15a). The same applies to the AA %, which also keeps increasing linearly with at constant rate ($\approx$ 0.003 %/s) reaching a final value of 30% degradation. The optical images at three different immersion times (1800, 3600 and 10800 s) show different optical features. At 1800 s (see Figure 2.14b) the optical changes have slightly extended further and become more intense: in the original images, in particular, the IM phase became black, while in the processed images changes of high intensity (purple-blue) are located at the centre of the IM particles, while the boundaries are less severely affected (orange-red). At 3600 s (see Figure 2.15b) the processed image shows propagation of optical changes (orange-red-pink intensity) to the Al-rich matrix between the IMCs. At 10800 s (see Figure 2.15b), on the other hand, optical images show coalescence of the degraded IMs into a single spot of high intensity (purple-blue, approximately 60 μm in size) surrounded by a halo of mild intensity changes (orange-red) spread across the matrix phase.
  For similar immersion times, literature reports a more global type of corrosion to be dominant [10, 23, 89, 90], characterised by the co-operative activity between IMs of different composition and their clustering into larger pits. These clusters, which were observed to be capped with corrosion products, were reported to extend the penetration of pits to the grain boundaries network, thus initiating intense subsurface corrosion forms like intergranular corrosion, exfoliation and grain etch-out [11]. The reduction in OCP transients' amplitude after 700 s and its consequent stabilisation around an average value (-0.5 V *vs* Ag/AgCl) suggest that stable pit growth might become favoured as all the exposed IMs have been already attacked and fewer sites for pit nucleation become available. Corrosion of AA 2024-T3 can propagate at an equilibrium value of potential, *i.e.* the free corrosion potential (E_{corr}). In spite of the featureless OCP from 700 to 10800 s, the optical images show different phenomena to be dominant. At 1800 s the optical changes have become more intense, but their extension still seems to be confined to the IM particles, thus suggesting that co-operative effects might start to play a role between 700 and 1800 s as subsurface events. From 1800 s to 3600 s, propagation of mild intensity degradation to the Al matrix denotes that clustering of IMs is still ongoing and becomes more evident as a surface event. At 10800 s of immersion, on the other hand, the Al matrix around between the IMs becomes severely degraded providing evidence of fully clustered IMs and, perhaps, the formation of a corrosion ring capped with a corrosion dome. It can be concluded that between 3600 s and 10800 s subsurface corrosion and its propagation to the grain boundary network (like intergranular corrosion and grain etchout) become dominant.

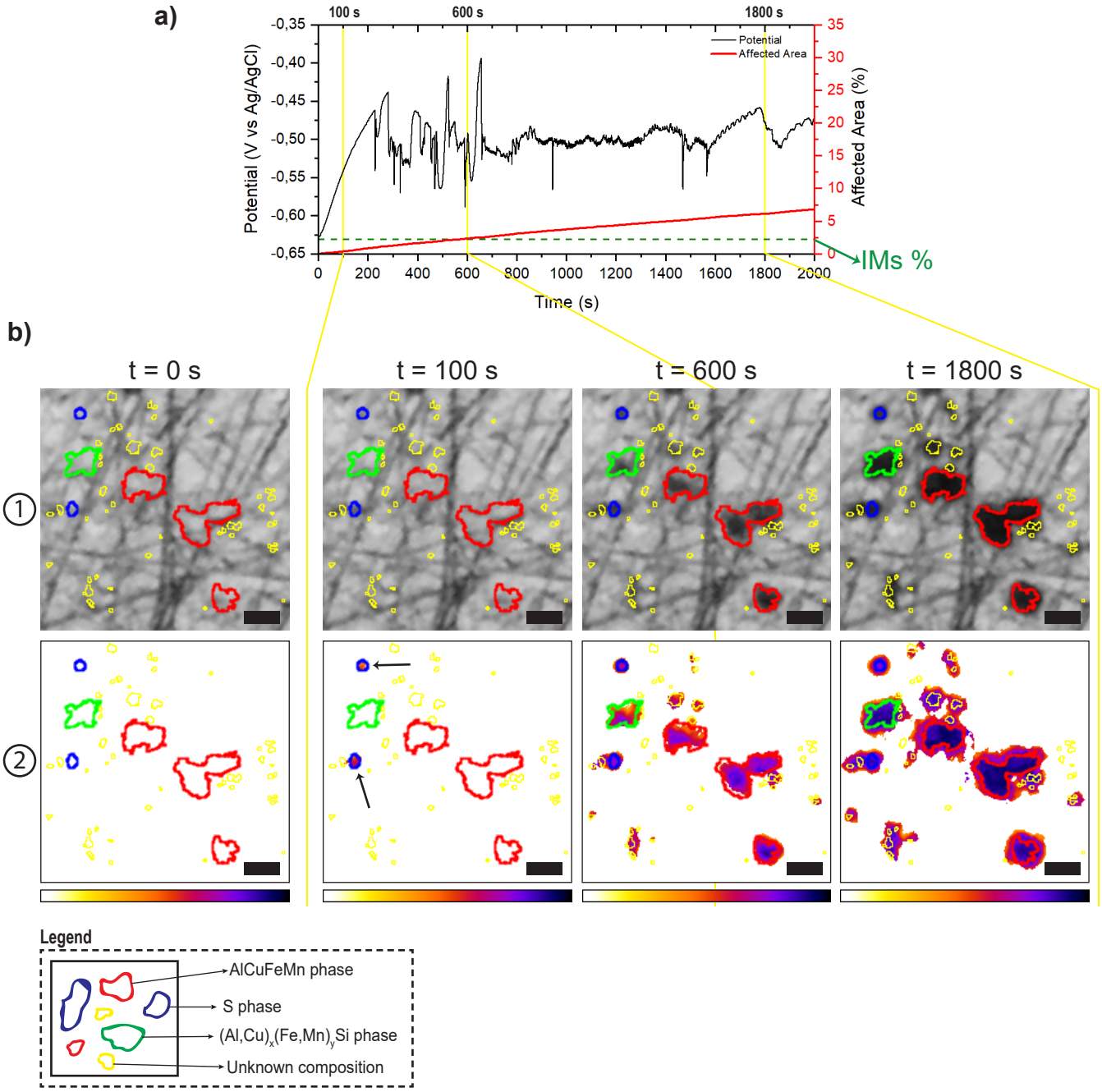

Figure 2.14: Opto-electrochemical data for AA 2024-T3 immersed in 0.05 M $NaCl_{aq}$ from 0 s to 2000 s. a) OPC-AA% plot and b) optical images at different immersion times. Row 1 represents original images, while row 2 represents processed images with image analysis. Scale bar shown in all images is 10 μm.

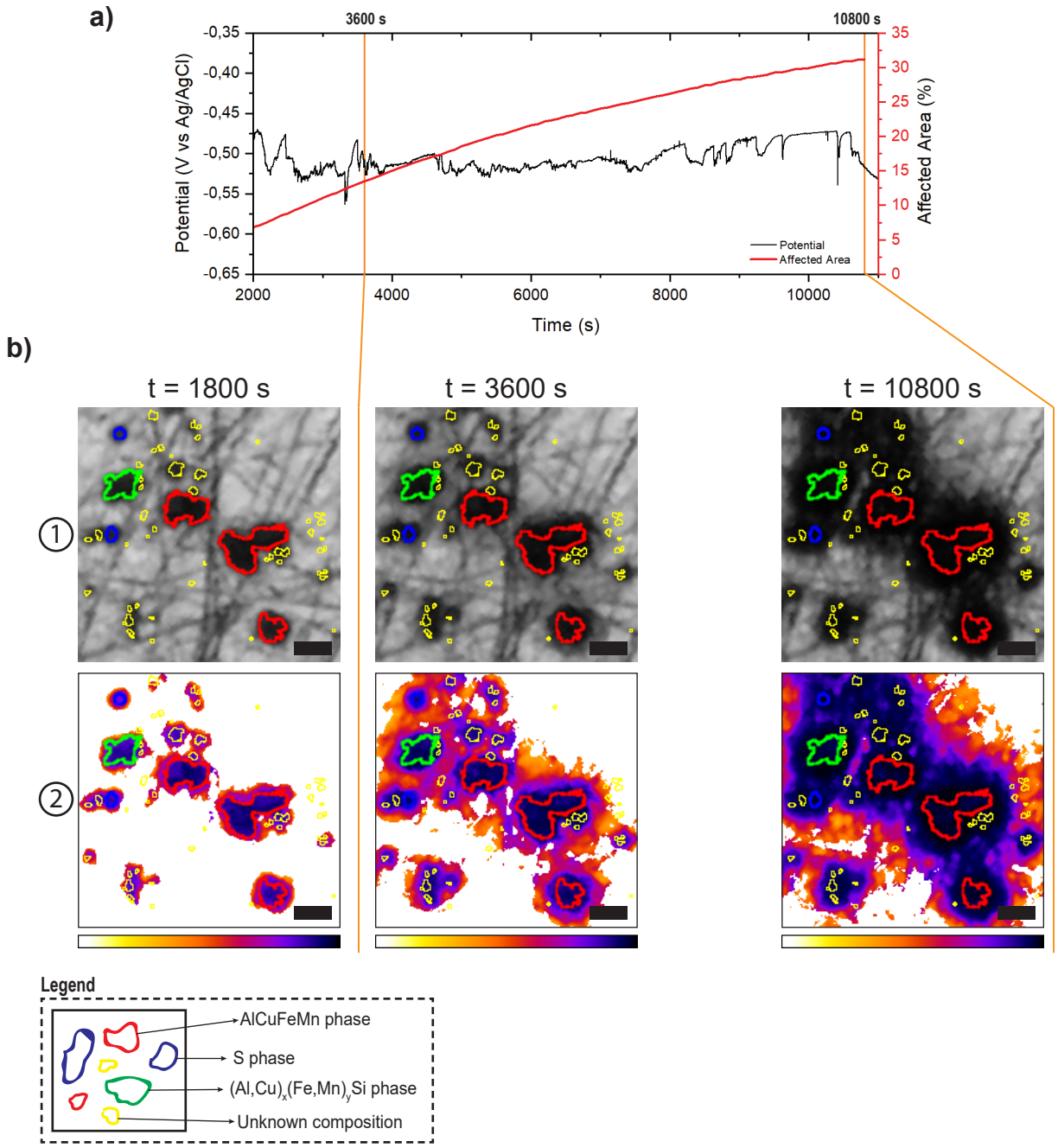

Figure 2.15: Opto-electrochemical data for AA 2024-T3 immersed in 0.05 M $NaCl_{aq}$ from 2000 s to 10800 s. a) OPC-AA% plot and b) optical images at different immersion times. Row 1 represents original images, while row 2 represents processed images with image analysis. Scale bar shown in all images is 10 μm.

2.4 Final Remarks and Conclusions

Figure 2.16 relates in a schematic figure the different OCP features to the optically detected changes. This figure helps to identify the macroscopic process based on the changes and features observed in the OCP. The data collected in real time helped to understand where the corrosion activity is located during the first stages of immersion, its relation to the surface composition, as well as the kinetics of each process without the need to rely on extensive and supplementary *post mortem* characterisation.

Corrosion, indeed, develops from a merely local scale, namely on the IM particles first (0-1800 s), to a more global scale involving both the IM phase and the matrix solid solution. The S phase, especially, was shown to be the most susceptible as it was the first, amongst others, to be attacked (after 100 s already). The IM phases with other compositions showed a delayed attack in time compared to the S phase, but eventually leading to the formation of corrosion pits. The delayed onset of the attack allowed to assign different electrochemical characters to the IM phase, especially the S phase is

believed to act as local anode, thus dealloying the least noble elements before the onset of OCP instability (*i.e.* trenching) is observed, while the other phases are presumed to act as local cathodes, thereby undergoing trenching. Corrosion is also characterised by a linear increase of the optical changes (AA%) in time with a constant rate (%/s). The entirety of results obtained underlined the high susceptibility of AA 2024-T3 if exposed to corrosive environments and the need to have it protected when in service. Optical macroscopic changes resulting from local electrochemical activity of the microstructure can promptly be detected on the IM phase (100 s), thus suggesting that further protection with corrosion inhibitors must have an equally fast and efficient action, primarily on the IM phase. The opto-electrochemical analysis may be helpful for the evaluation of corrosion inhibition efficiency depending on the suppression/enhancement of i) quantitative and qualitative optical features and ii) unstable fluctuations in the electrochemical potential.

The accurate reconstruction of the AA 2024-T3 corrosion process through the parallel analysis of optical and electrochemical data, allows to conclude that the opto-electrochemical analysis with high spatio-temporal resolution and the analysis protocol developed are feasible tools to further study corrosion inhibition properties on this alloy.

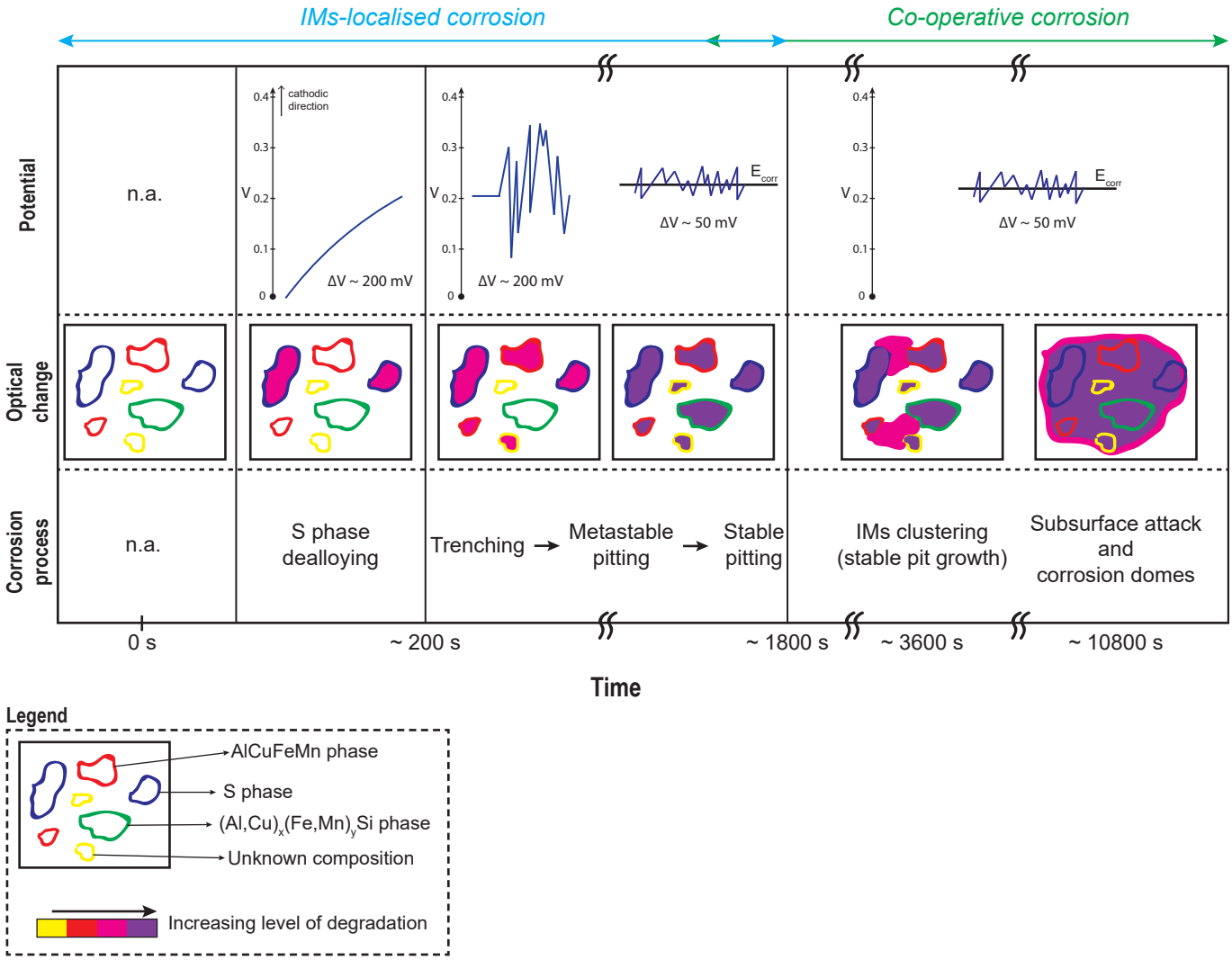

Figure 2.16: Hierarchical corrosion of AA 2024-T3 explained and summarised with real-time optical analysis and electrochemical potential noise.

Chapter 3

Inhibition properties of $Ce(NO_3)_3$ studied with opto-electrochemical techniques

The opto-electrochemical setup provides useful information about surface (electrochemical) processes and their relation to electrochemical potential (Chapter 2). Therefore, in this chapter, systems where corrosion of AA 2024-T3 is stopped by inhibiting compounds, namely $Ce(NO_3)_3$, are investigated with the same method. Studies with different $Ce(NO_3)_3$-concentrations are demonstrated to provide different degrees of protection to the alloy, but overall offering the same underlying inhibition mechanism. Together with the protection supplied by $Ce(NO_3)_3$, its loss in protection after re-immersion in inhibitor-free electrolytes is also studied by means of optics, electrochemistry and localised electrochemistry.

3.1 Introduction

In the previous chapter (Chapter 2), the opto-elctrochemical setup was presented and described in detail. Its suitability to study corrosion of AA 2024-T3 in Cl^- containing solutions was also demonstrated thanks to the image analysis protocol used, which helps and improves the information obtained from the OCP signals.

In this chapter, a step forward is taken by studying inhibition processes of 2024-T3 alloy with the same opto-electrochemical setup. An attempt is made to match the macroscopic optical changes to the electrochemical potential and, consequently, relate these pieces of information to the (thermodynamic) stability of the system studied.

$Ce(NO_3)_3 \cdot 6\ H_2O$ was chosen for this research as a model inhibitor to represent the general behaviour of Ce(III). The potential of Ce(III) inhibitors for the replacement of Cr(VI) has been discussed in Chapter 1, but many aspects of the actual protection mechanisms are still debated, especially on its stability during re-immersion conditions. This chapter will therefore focus on gaining a better understanding of cerium film formation and cerium passive layer stability with the help of combined optical and electrochemical analysis.

3.2 Experimental

All the test methodologies reported in this chapter were carried out with the same opto-electrochemical setup and protocol described in Chapter 2. The sample preparation steps, test parameters and post-processing analysis are the same as described in section 2.2 and, therefore, they will not be reported here. Conversely, the additional materials, methods, experimetal details and protocols of analysis presented in this chapter will be described more in detail.

3.2.1 Materials and electrolytes

Sodium chloride (NaCl) with purity >98% was purchased from VWR Chemicals and used without further purification. Cerium(III) nitrate hexaydrate ($Ce(NO_3)_3 \cdot 6\ H_2O$) with a purity of 99% was purchased from Sigma Aldrich and used without further purification. Hydrogen Peroxide (H_2O_2) with a concentreation of 30% (w/w) in H_2O was also purchased from Sigma Aldrich. Millipore® Elix 3 UV filtered water was used to make electrolytic solutions.

NaCl electrolytes were prepared by dissolving NaCl in water to obtain a concentration equal to 0.05 M. The inhibition properties of Ce(III) inhibitor were tested by immersing the samples in NaCl solutions doped with different additions of $Ce(NO_3)_3 \cdot 6\ H_2O$. In particular, Ce(III)-containing electrolytes were tested and compared at three concentrations: 0.01 mM, 0.1 mM and 1 mM. For tests with hydrogen peroxide, an additional solution of H_2O_2 was prepared by diluting the 30% (w/w) as-received solution to a concentration of 0.1 wt% with the NaCl solution.

3.2.2 Immersion protocols for opto-electrochemical analysis

Figure 3.1 shows the protocols of immersion for the different opto-electrochemical studies presented in this chapter. For all the protocols shown in Figure 3.1, the electrolytic cell (described in section 2.2.4.1) was flushed three times with demineralised water before immersion to wash it from possible contamination.

Figure 3.1a refers to the opto-electrochemical study about the effect of $Ce(NO_3)_3$ concentration on the protection of AA2024-T3, consisting of a 15 h immersion in $Ce(NO_3)_3$-doped solutions at different concentrations. These tests were carried out at least three times.

Figure 3.1b, on the other hand, refers to the study of Ce(III) inhibitive layers stability. Stability was tested after a first 15 h immersion in $Ce(NO_3)_3$ electrolyte (1 mM), followed by a 5 h re-immersion in NaCl electrolyte. Between the two immersion steps, the sample was removed from the electrolytic cell and gently dried with N_2. The electrolytic cell was also flushed three times with demineralised water to clean it from Ce(III) contamination before further testing. These tests were carried out at least three times.

Figure 3.1c represents the immersion protocol for support tests with H_2O_2 solutions, consisting of a first short immersion in a $Ce(NO_3)_3$ 1 mM solution (2 h), followed by an immersion in the 0.1 wt% H_2O_2 electrolyte for further 30 minutes. For these tests, however, the samples were neither removed from the electrolytic cell nor dried with N_2 after the first exposure to Ce(III). At the moment of changing electrolyte, the Faraday cage was opened and the new electrolyte was flushed in the cell while the potentiostat was still measuring. This procedure allowed to record the OCP with continuity and estimate the effect of the addition of an oxidising agent without introducing factitious effects (*e.g.* oxidation) due to intermediate drying. The sample was only removed and dried with N_2 at the end of the test for further analysis. These tests were performed at least three times.

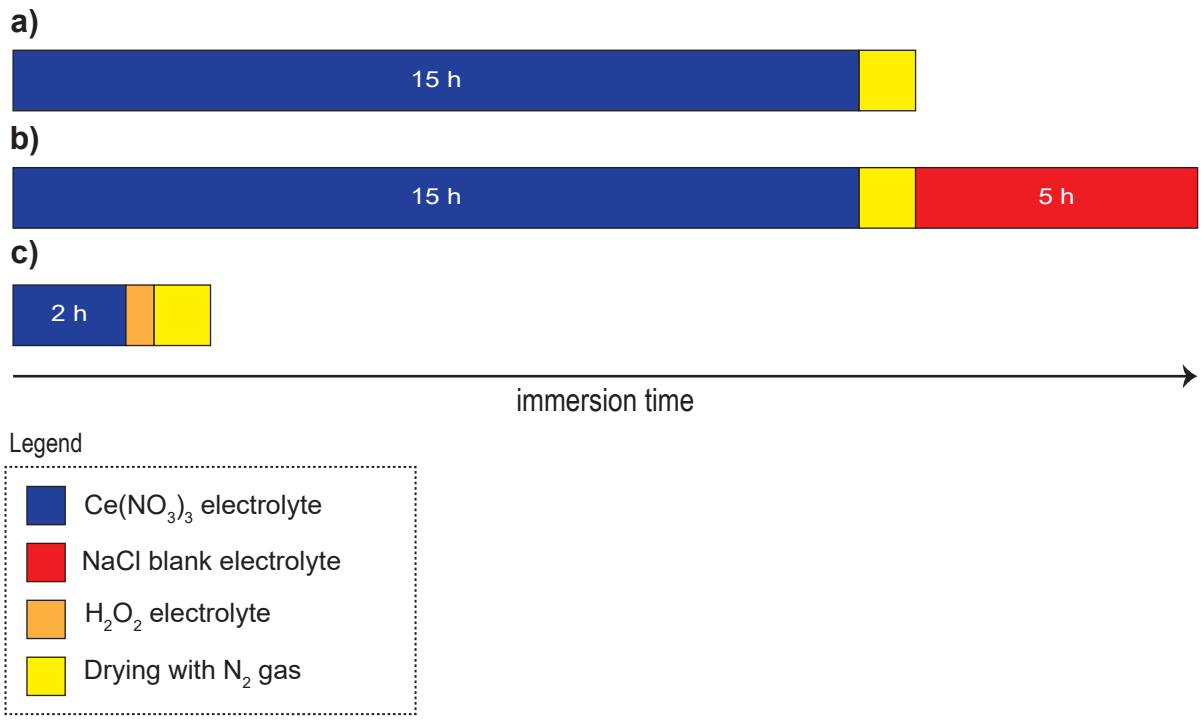

Figure 3.1: Test protocols for a) studies at different $Ce(NO_3)_3$ concentrations and EIS b) stability to re-immersion in NaCl c) tests with H_2O_2 electrolyte.

3.2.3 Support testing to the opto-electrochemical analysis

3.2.3.1 SEM-BSE *post mortem*

SEM-BSE images *post mortem* were collected by means of a scanning electron microscope (JEOL JSM-IT100), with the same working conditions mentioned in section 2.2.3. Also for *post mortem* analysis, the same stitching procedure was applied to reconstruct the exposed surface, as well as the same optical-fitting procedure mentioned in section 2.2.4.4.

3.2.3.2 Electrochemical impedance spectroscopy

Electrochemical impedance spectroscopy (EIS) was employed to characterise the evolution of the protective properties of Ce(III) inhibitors during the same immersion time used for concentration tests, *i.e.* 15 h. To this purpose, only Ce(III)-doped electrolyte with a concentration of 1 mM was tested and the same protocol of analysis shown in Figure 3.1a was adopted. The first EIS measurement was done after 1 h of immersion to get a stable OCP. EIS plots at 1 h, 7 h and 15 h of immersion were collected as representative of the beginning, middle and end of the test, respectively. As a reference for comparison, EIS measurement in a blank solution was done with the same conditions, with the only difference that the total immersion time was kept to 3 h, as it was considered enough to get all the information needed from the results presented in section 2.3. The tests were repeated three times.

EIS measurements were carried out with a Metrohm PGSTAT 302 potentiostat fitted with FRA32M module and controlled through NOVA V1.11.1 software. A three-electrodes configuration was adopted, in which the 2024-T3 sample served as the WE, Ag/AgCl (sat. KCl) was the RE and the Pt wire was the CE. The frequencies scanned ranged from 10^{-2} Hz to 10^{5} Hz. The number of frequencies scanned in this range was equal to 50 with a logarithmic frequency step between each data point. The polarization applied had the shape of a single sine wave with an amplitude equal to $\pm$ 10 mV (root mean square) with respect to open circuit potential.

3.2.3.3 Ce(III) layers stability studied with Scanning Kelvin Probe Force Microscopy

Stability of Ce(III) inhibitive layer was studied also Scanning Kelvin Probe Force Microscopy (SKPFM). For this technique, the samples used and their preparation differed from the ones previously described. Samples for SKPFM analysis were cut from a 2 mm thick sheet of AA 2024-T3 with a surface area of 8x8 mm^2. The samples were grinded with 1000, 2400 and 4000 SiC paper. Unlike the previous samples, polishing was done with both 3 μm and 1 μm diamond-based polishing

pastes. Due to the high surface resolution of SKPFM, indeed, surface roughness is an important factor to be controlled, because high roughness can generate artifacts in the Volta potential measurements.

Measurements were carried out with a Kelvin Probe Force Microscope (Dimension Edge with ScanAsyst™, Brüker), equipped with a Pt-Ir coated electrically conductive tip (SCM-PIT-V2) of 25 nm tip radius and 10-15 μm tip height. The same tip was used for all the measurements. All the experiments were carried out at ambient condition, with a 5 V bias voltage applied and a tip lift of 100 nm. The pixel resolution of the acquired images was equal to 256x256 pixels^2 for measurements before and after immersion in $Ce(NO_3)_3$, while after immersion in NaCl this was increased to 512x512 pixels^2.

3.3 Results and Discussion

3.3.1 Effect of $Ce(NO_3)_3$ concentration on the protection of AA 2024-T3

Figure 3.2 and Figure 3.3 report the results of AA% *vs* time for different immersion times and different $Ce(NO_3)_3$ concentrations. Figure 3.2, in particular, shows the plot for the first three hours of immersion, so that the AA% could be also compared to the reference sample immersed in a NaCl solution shown in Chapter 2. This graph clearly shows that presence of Ce(III) strongly affects the degree of optical changes already in the first 3 h of immersion, because for all the Ce(III) concentrations tested, macroscopic changes do not involve more than 2.5% of the exposed surface, which is one order of magnitude lower than for the reference sample (30% degraded area) at the same immersion time.

Figure 3.3 shows the AA% trends of Ce(III)-doped electrolytes at different concentrations for 15 h of immersion. This graph confirms the low variation in the affected area even after 15 h immersion in the presence of cerium ions, not even reaching values above 4% at the end of the immersion time. However, the three curves display two different processes based on their kinetics:

- Ce(III) at a concentration of 0.01 mM shows an initial fast increase of the AA%, which tends to flatten into a plateau after $\approx$ 10000 s until it starts to increase again (after 30000 s) with a slower rate towards the end of the test.
- Ce(III) at 0.1 and 1 mM concentration, on the other hand, show a similar S shape of the AA% curve, characterised by an initial flatness close to 0%, followed by an increased optical activity after some time, which keeps growing albeit slowing down again towards the end of the test (this trend being more pronounced for higher cerium content). The onset of optical activity is also delayed in time for the highest concentration tested, *i.e.* 1 mM.

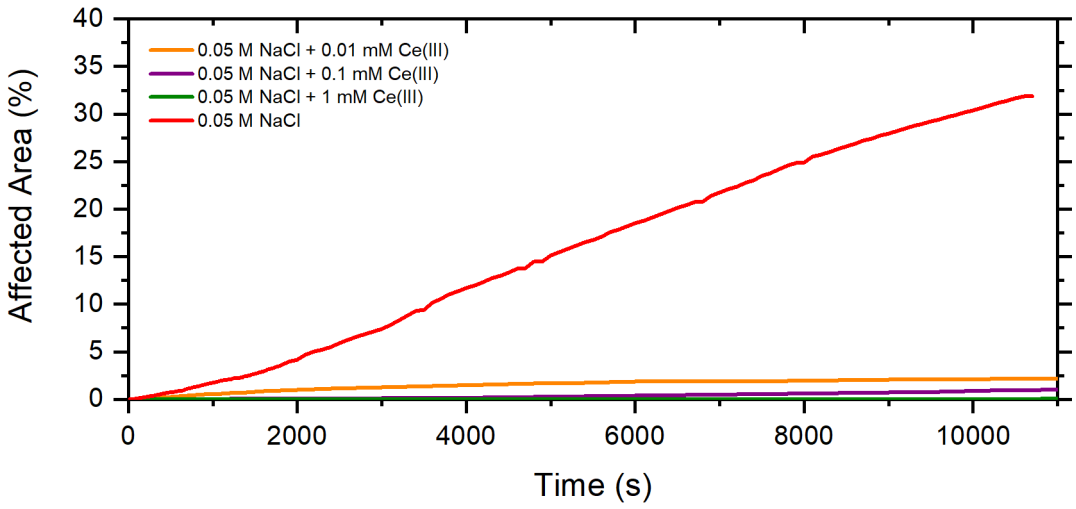

Figure 3.2: Curves of the calculated affected area % *vs* time for the fisrt 3 h immersion in 0.05 M NaCl and 0.05 M NaCl + 0.01/0.1/1 mM $Ce(NO_3)_3$.

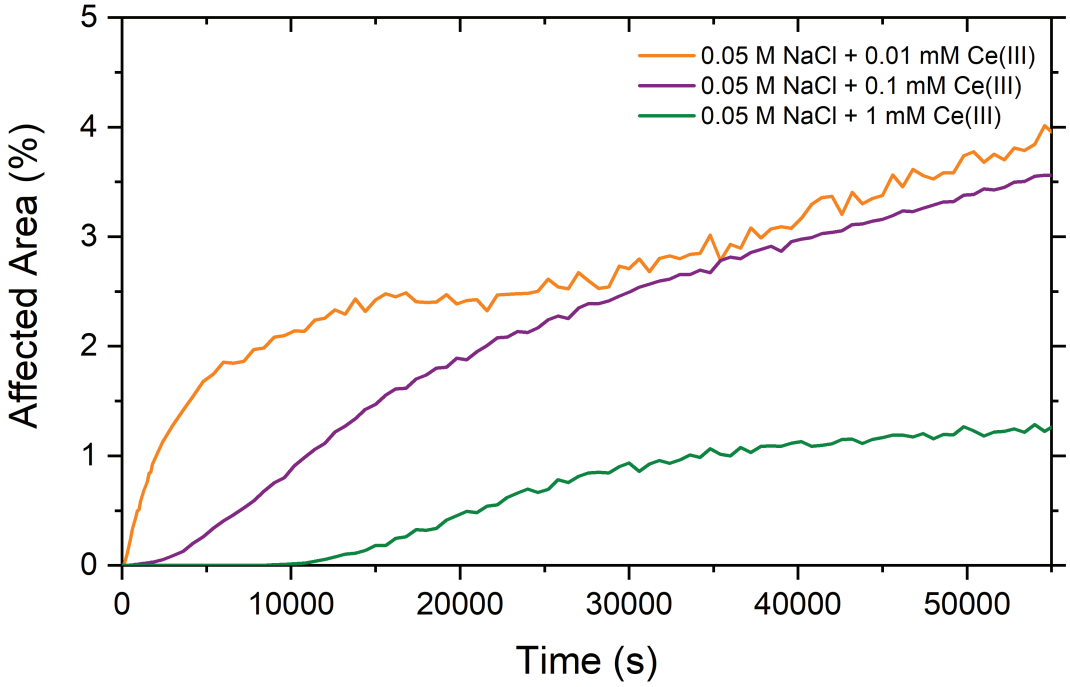

Figure 3.3: Curves of the calculated affected area % *vs* time for 15 h immersion in $Ce(NO_3)_3$ saline solutions at 0.01, 0.1 and 1 mM concentrations.

The trends of OCP fluctuations were also analysed for different concentrations and they can be seen in Figure 3.4. From these graphs, OCP fluctuates in a range of approximately 50-100 mV, but there is a remarkable decrease (or even lack) of transients compared to the one observed in Figure 2.14a. In addition to that, Figure 3.4 displays OCP trends sharing some similarities in spite of the difference in Ce(III) concentration. The global trend of OCP can be summarised as follows: there is an initial decrease towards more anodic values until a minimum value is reached, after which the potential starts to increase again towards more positive values. These observations might suggest that the addition of Ce(III) to the solutions causes a stabilisation of the system studied regardless of the concentration, most likely with the same underlying mechanism.

In order to understand and justify the different kinetics of optical changes for different concentrations, the optical and electrochemical data were analysed together. Figure 3.5 and 3.6 represent the optical-electrochemical data for the lowest (0.01 mM) and highest (1 mM) concentrations, respectively. The AA% curves were plotted together with OCP as shown in Figure 3.5a and Figure 3.6a. The change in slope (blue dotted lines), and thereof kinetics, of the AA% curve allowed to identify salient transition times for the two concentrations, which in both cases split up the immersion time in three stages. These transition times are depicted in Figure 3.5a and Figure 3.6a as vertical bars in the OCP-AA% plot, and the three stages were labelled with roman numbers (I, II and III). The optical (original and processed) images of the samples in immersion at these transition times were also reported in Figure 3.5b and Figure 3.6b.

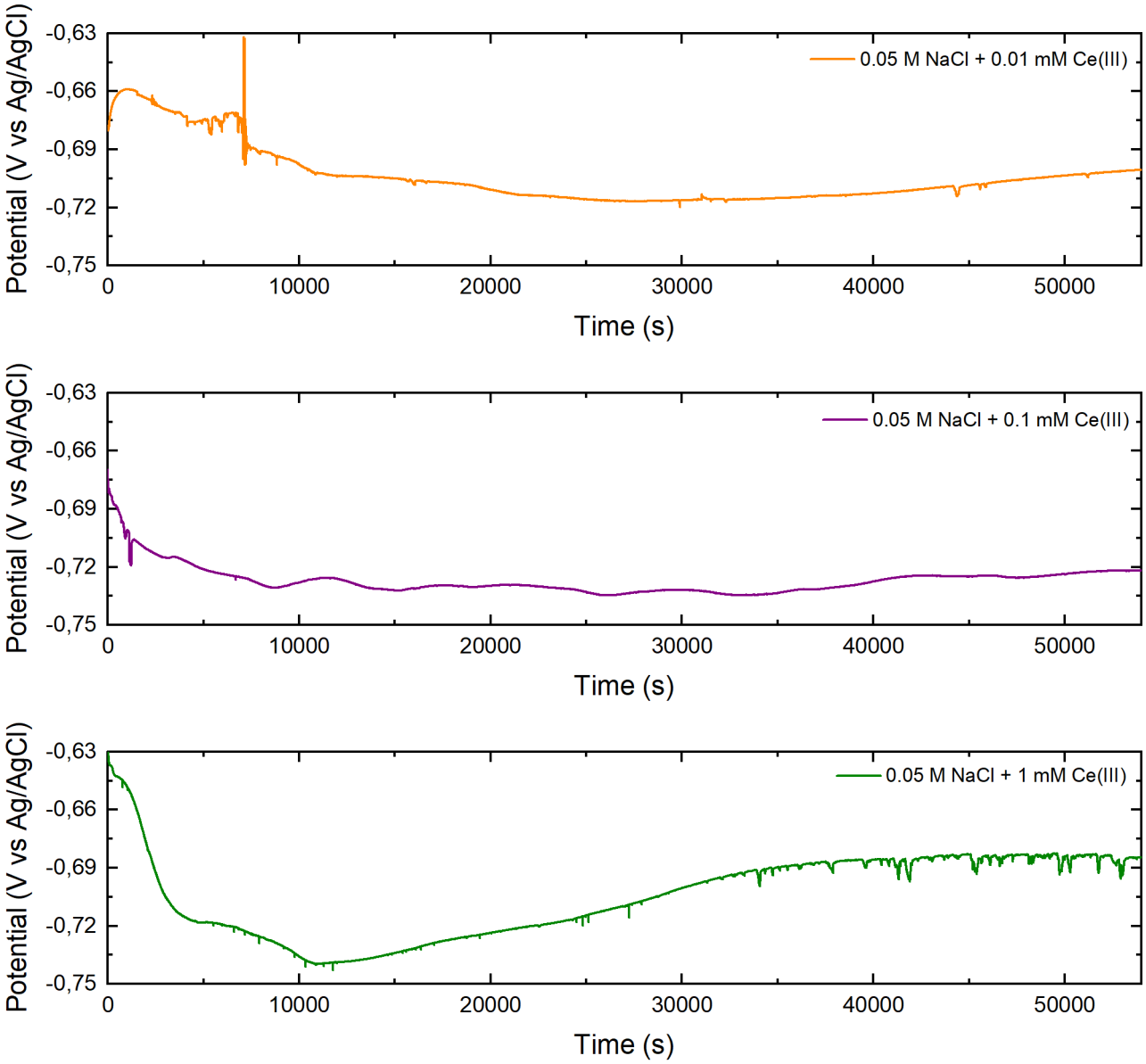

Figure 3.4: Open circuit potential trends for 15 h of immersion in $Ce(NO_3)_3$ at 0.01, 0.1 and 1 mM concentrations.

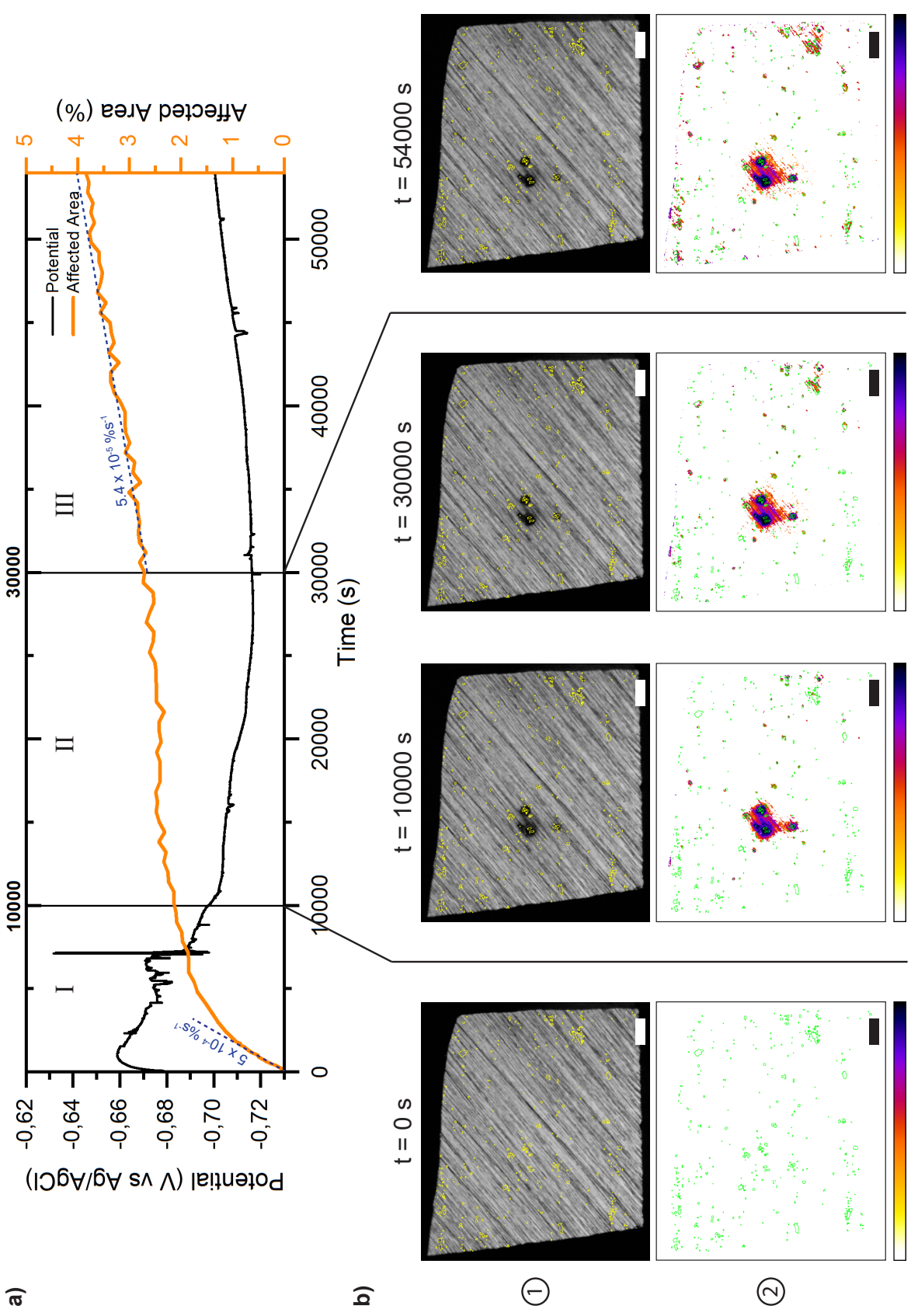

Figure 3.5: Opto-electrochemical data for AA 2024-T3 immersed in 0.01 mM $Ce(NO_3)_3$ consisting of a) OCP-AA% plot throughout the 15 h immersion time and b) optical original (row 1) and processed (row 2) images at 0, 10000, 30000 and 54000 s. The scale bar in the images represent 50 μm.

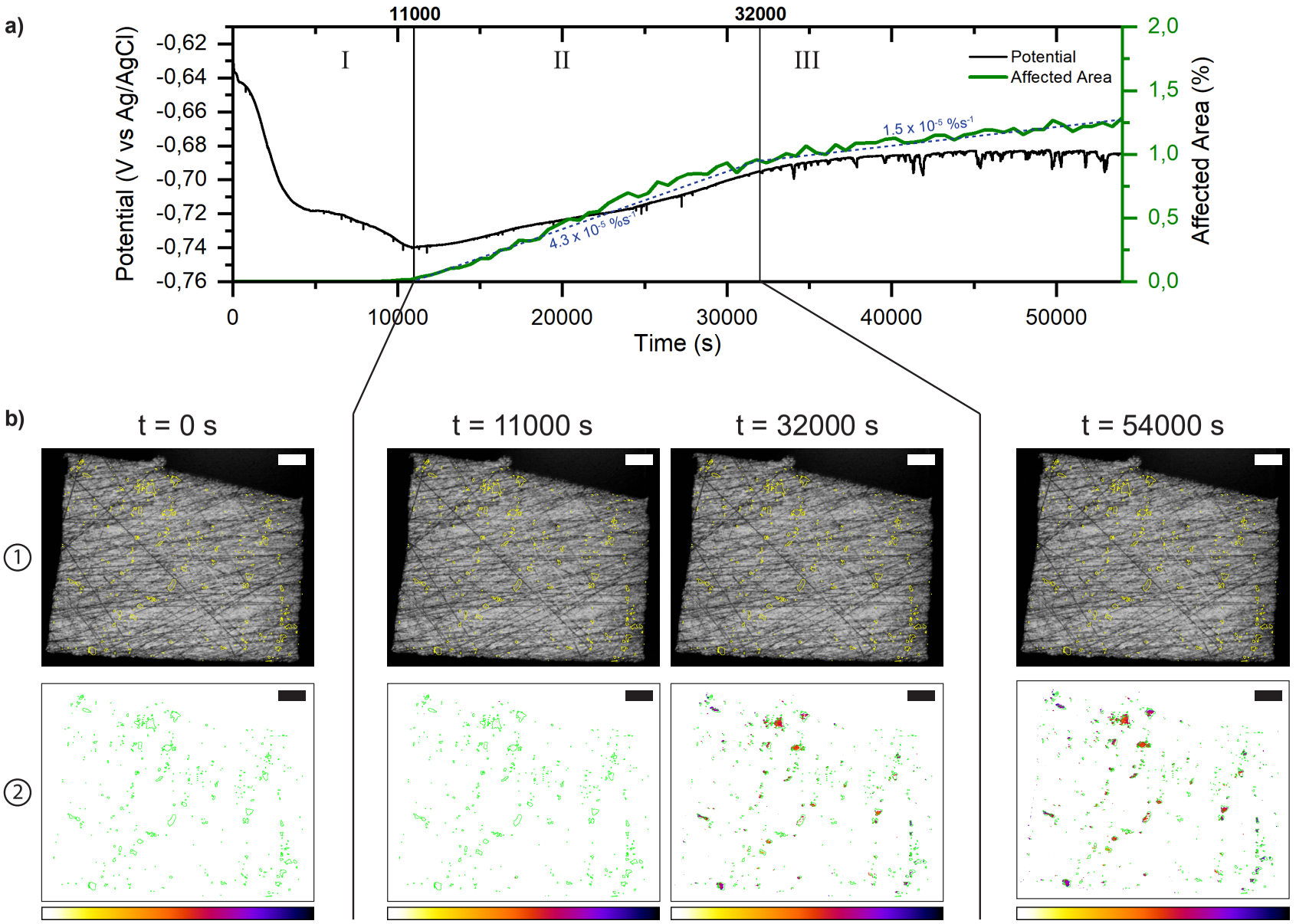

Figure 3.6: Opto-electrochemical data for AA 2024-T3 immersed in 1 mM $Ce(NO_3)_3$ consisting of a) OCP-AA% plot throughout the 15 h immersion time and b) optical original (row 1) and processed (row 2) images at 0, 11000, 32000 and 54000 s. The scale bar in the images represent 50 μm.

The results can be summarised as follows:

* **0.01 mM $Ce(NO_3)_3$**: Figure 3.5a shows a fast intial growth of the AA% ($5 \cdot 10^{-4}$ %/s) in the first 10000 s (Stage I) accompanied by an unstable potential with some individual peaks similar to transients ($\approx$ 70 mV). It has to be noted that the optical rate is still significantly lower than the one observed for a Ce-free electrolyte (0.003 %/s, see section 2.3). In this stage optical images (3.5b) also show an intense activity of the surface confined to a limited number of locations, reaching a high degree of change (purple-blue in the colour intensity bar). Additionally, these changes have almost circular shape and seem to be centered around a few IM particles. Nevertheless, the AA% involved after 10000 s is only limited to $\approx$ 2.2%, meaning that the remaining surface exposed (and actually the majority of it) is not affected. In the second stage of immersion (10000-30000 s, Stage II), characterised by a stabilisation of AA% into a plateau (2.2-2-7 %), the OCP stabilises (*i.e.* no transients visible) and decreases from -0.70 V *vs* Ag/AgCl to -0.72 V *vs* Ag/AgCl towards more negative values. The optical images, indeed, do not show many new significant changes on the surface apart from the ones already observed during stage I. Finally, Figure 3.5a shows that Stage III (30000-54000 s) the AA% starts to increase again from 2.7% to 4% but more slowly than in Stage I ($5.4 \cdot 10^{-5}$ %/s), while the OCP signal changes its direction towards more positive values (from -0.72 V *vs* Ag/AgCl to -0.70 V *vs* Ag/AgCl). The original images in Figure 3.5b at this immersion time still do not show significant changes, but the image analysis reveals pixels belonging to some IMs (and the immediate surroundings) have undergone mild intensity changes (orange-red).
  The initial instability of OCP combined with a high optical activity confined to a few IM particles suggest that early pitting has occurred on these particles. The rest of the exposed surface (the IMs especially) is not significantly affected during the first 10000 s, thus suggesting a general protection process provided by $Ce(NO_3)_3$. Corrosion inhibition, indeed, might become dominant during the second stage of immersion (10000-30000 s), in which the growth of the previously nucleated pits seems to be inhibited and the potential becomes more negative and free of transients. This is in line with the idea that cathodic inhibitors block the cathodic sites, leading to an increase of the anodic area, thus the drop of OCP [94]. The nature of the activity observed in finale stage (30000-54000 s) is not completely clear, especially because the IM phase seems to be optically affected. However, the total low percentage of AA% (4%) at the end of the test allows to conclude that corrosion processes are remarkably slowed down.
* **1 mM $Ce(NO_3)_3$**: Figure 3.6a shows barely any optical change detected for the first 11000 s (AA% = 0%) matched with a stable and decreasing OCP from -0.64 V *vs* Ag/AgCl to -0.74 V *vs* Ag/AgCl. As expected, also the optical images in Figure 3.6b do not show any change from 0 to 11000 s. Figure 3.6a during Stage II (11000-32000 s), on the other hand, shows the onset of a slow AA% activity ($4.3 \cdot 10^{-5}$ %/s) going from 0% to 0.9%, accompanied by an increasing potential from -0.74 V *vs* Ag/AgCl to -0.70 V *vs* Ag/AgCl. The original images of Figure 3.6b still seem to show a pristine surface, but the image analysis reveals once again that pixels within the IMs boundaries have undergone changes of mild intensity (red). These changes seem to spread and consolidate on the IM phase during Stage III (32000-54000 s), which is also charcaterised by a slower rate of optical changes ($1.5 \cdot 10^{-5}$ %/s) compared to Stage II. The potential also stabilises around -0.69 V *vs* Ag/AgCl, although small individual spikes seem to reappear ($<$ 10 mV).
  From these observations, it can be concluded that corrosion inhibition is achieved for sure during the first stage of immersion as the optical activity is practically null and the potential is free of transients. Despite changing direction throughout the 15 h of immersion, the potential indicates a general stability of the system studied. Optical activity becomes more substantial after the first 11000 s, but its nature is still not very clear from these results, especially due to its preferential localisation on the IM phase. However, the low amount of optical changes detected at the end of the test (1.25%), which is even lower than the surface percentage of exposed IMs ($\approx$ 2.6%), makes it possible to conclude once again that corrosion processes are remarkably slowed down also at this concentration. In comparison, a concentration equal to 1 mM seems to provide better inhibition compared to 0.01 mM because of a lower optical activity, a more stable potential throughout the immersion time and the absence of localised corrosion events (*e.g.* corrosion pits).

Overall, this opto-electrochemical analysis does not provide information about corrosion rate, *i.e.* on the corrosion current density, which makes it hard to quantify the corrosion inhibition efficiency. However, the low amount of AA% at the end of the test (Figure 3.3), combined with a transient-free OCP (Figure 3.4) and the almost total suppression of corrosion-related optical features observed in section 2.3 (Figure 3.5 and 3.6), makes it possible to say with good approximation that corrosion rate is also decreased.

From the conclusions obtained in Chapter 2, a fast and efficient protection was outlined as an important prerequisite for a successful inhibition, because corrosive phenomena such as S phase dealloying can be already established within the first 100 s on this alloy. The results showed above suggest that this is not the case of $Ce(NO_3)_3$ at a concentration of

0.01 mM, because early pitting at a few IMs was still observed (Stage I of Figure 3.5). To explain the initial activity witnessed at this Ce(III) concentration, the Langmuir adsorption theory was employed as a first order approximation model to describe the first seconds of immersion in Ce(III) solutions. The derivation, discussion and implications of this theory are reported in Appendix A.1.

The modelling of the system through Langmuir's adsorption allows to assume the existence of a critical value of Ce(III) concentration (C_{crit}), above which protection of 2024-T3 is achieved and below which inhibition is only partially achieved. This critical concentration and its effect is clarified in Figure 3.7, where Ce concentration profiles are plotted in the vicinity of the electrode's surface as a function of distance (x). It is reasonable to assume that the precipitation of $Ce(OH)_3$ on the surface creates a diffusive layer (δ) close to it, in which the concentration of Ce^{3+} becomes lower than the nominal electrolyte concentration. If the concentration of cerium in the diffusion layer crosses the line of C_{crit}, then the concentration of cerium at the surface would not be enough to have an homogeneous and protective layer. This might explain well the case of $Ce(NO_3)_3$ at 0.01 mM, where nucleation and growth of corrosion pits is seen in the first hours of immersion. However, it is also important to note that stabilisation of pits is also witnessed for prolonged immersion (stage II, Figure 3.5), implying that formation of protective precipitates is still possible at low Ce concentrations, but it simply takes more time to develop coherent layers due to the lower supply of Ce from the electrolyte. Ce(III) at 0.1 and 1 mM, on the other hand, is above C_{crit}, thus showing an optically-unaffected surface already during the first hours of immersion.

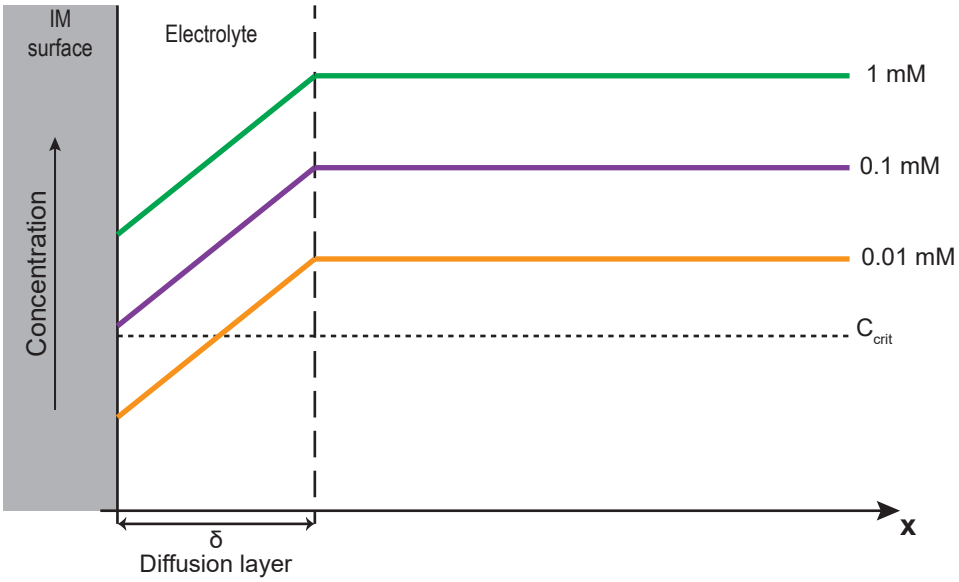

Figure 3.7: Concentration profiles of Ce^{3+} in the vicinity of the electrode's surface as a function of the distance (x). The effect of $Ce(NO_3)_3$ concentration on the protection of AA 2024-T3 is represented in relation to the critical value (C_{crit}).

3.3.2 Identification of optical-electrochemical data during immersion in Ce(III)-based solutions

Opto-electrochemical analysis at different $Ce(NO_3)_3$ concentrations was successful in demonstrating different degrees of protection on AA 2024-T3, especially during the first hours of immersion (stage I of Figure 3.5 and 3.6). The main outcome of these tests was that best protection is achieved with 1 mM $Ce(NO_3)_3$. For longer immersion times (stages II and III of Figure 3.6), however, mild intensity optical changes located on the IM particles were detected, typically accompanied by an increase in OCP towards the more cathodic direction.

There are three possible explanations to interpret these optical changes:

- Formation of $Ce(OH)_3$ deposits on the (cathodic) IM phase and their progressive thickening in time.
- Oxidation of Ce(III) to Ce(IV) deposits and consequent formation of CeO_2 phase on top of the IM particles.
- Corrosion attack of the IM phase, significantly slowed down and delayed in time due to the presence of Ce^{3+} ions in solution.

In order to clarify which of the three options better explains the optical changes observed, a set of dedicated tests was performed.

First, SEM-BSE *post mortem* analysis, which is reported in Appendix A.2 for the sake of clarity (Figure A.2), showed absence of corrosion (*e.g.* trenching around IMs, pitting, *etc.*) after 15 h immersion in 1 mM $Ce(NO_3)_3$. This directly indicates that the surface changes observed are not related to corrosion but possibly to one or both of the other options related to the inhibiting process. EDS analysis, however, was not successful in detecting Ce-layers on top of the IMs either. To shed some extra light on this issue both EIS and a controlled oxidation test with hydrogen peroxide were designed.

Electrochemical impedance spectroscopy was tested on AA 2024-T3 in two different electrolytic solutions, namely 0.05 M NaCl and 0.05 M NaCl + 1 mM $Ce(NO_3)_3$. The results of this test and their discussion are reported in Appendix A.3. On balance, EIS results suggest that $Ce(NO_3)_3$ protects the AA 2024-T3 surface when added in small amounts to a NaCl solution by creating a thin layer with capacitive behaviour, which tends to improve both its capacitive properties and the charge transfer resistance during the immersion time (15 h), in a similar way as the one observed in [69] with polarisation curves.

It is still unclear from EIS whether the optical changes on the IM phase observed in Figure 3.6 could be related to a thickening effect of the Ce(III) layers or maybe to the formation of a more stable oxide phase: the results from this technique, indeed, do not exclude neither one nor the other option. What is more clear is that EIS excludes the option of delayed corrosion within the test time, otherwise for long exposures (15 h) a more substantial decrease in impedance would have been noticed. Therefore, the IM-localised optical changes observed during immersion in Ce(III) solution (see Figure 3.6) are most likely not associated to corrosion.

The opto-electrochemical mesurement with hydrogen peroxide solutions is an *in situ* test designed to prove or confute the hypothesis of IM-localised optical changes as a consequence of oxidation of cerium inhibitive layers from Ce(III) to Ce(IV) and the consequent formation of ceria (CeO_2). Hydrogen peroxide is added to the system because it acts as a strong oxidising agent, thus promoting the oxidation of Ce(III) to Ce(IV) species. The idea behind such test is to use the same setup and conditions as before (*i.e.* immersion in a $Ce(NO_3)_3$-doped solution while monitoring OCP fluctuations together with real-time optical changes) to see if the addition of an oxidizing agent like hydrogen peroxide causes similar OCP signal and optical changes as the ones observed in Figure 3.6. The results from this test are reported and discussed in Appendix A.4.

In summary, addition of H_2O_2 to the solution caused the following effects:

- Appearance of mild intensity optical changes located on the IMs (similar to the ones observed in Figure 3.6 after 11000 s) soon after the introduction of H_2O_2 to the system ($\approx$ 5 min);
- Increase of OCP towards the more positive values;
- Protection of the IM particles after 30 minutes immersion in H_2O_2, albeit clear signs of corrosion spread on the Al-matrix.

On balance, the results obtained seem to suggest that the optical changes detected can be ascribed to the selective deposition of Ce-inhibitive layers on the IM particles, which protect them from corrosion. In particular, the accelerated detection of these optical changes after the addition of H_2O_2 ($\approx$ 5 minutes after H_2O_2 addition) together with the prompt increase in potential to more noble values, suggests that formation of a passive Ce(IV)-oxide layer (CeO_2) occurs on the IMs, as a consequence of the peroxide-promoted oxidation from Ce(III) to Ce(IV) species.

It is, again, difficult to say whether the optical signal observed on the IMs is only caused by a progressive thickening effect of the deposits or just due to the oxidation itself as a change in refractive index. It is reasonable to assume that both these processes are actually occurring simultaneously, so that a progressive build-up of a passive oxide phase on top of the IMs leads to an increased protection. This explanation is also in agreement with the conclusions made with EIS. On the other hand, the lack of Ce detection with EDS and Raman spectroscopy underline the substantial thinness of these protective layers, which raises questions about the optical detection limit due to thickening.

In any case, the *in situ* opto-electrochemical analysis with hydrogen peroxide confirmed itself to be a powerful tool to corroborate the active role of H_2O_2 during the inhibition mechanism provided by $Ce(NO_3)_3$ (and Ce(III) inhibitors in general) through the two-electron pathway, as it was discussed in section 1.2.3. In this way, we confirm that oxidation of Ce(III) to Ce(IV) and CeO_2 formation is possible due to peroxide oxidation, and that the surface changes observed in Figure 3.6 after 11000 s can be related to passive CeO_2 layer thickening in time.

The combination of optical-electrochemical analysis, SEM-EDS, EIS and the H_2O_2-test allows proposing a mechanism of inhibition and layer build-up provided by Ce(III) inhibitors. The mechanism proposed corroborates the one discussed in section 1.2.3 and it is schematically shown in Figure 3.8, considering the expected signals from an optical-electrochemical measurement.

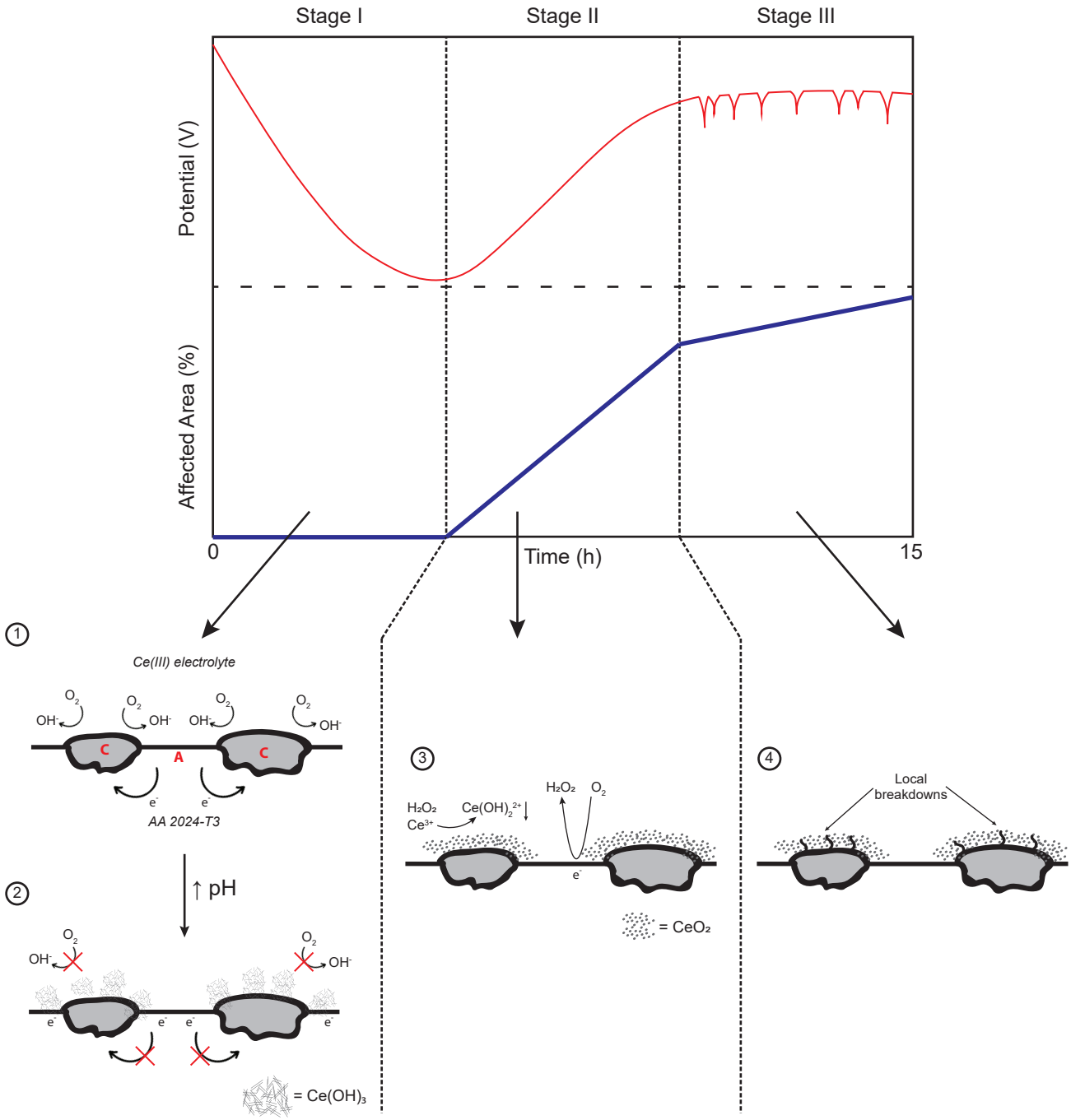

Figure 3.8: Inihibition mechanism of Ce(III) inhibitors explained by means of real-time optical-electrochemical characterisation.

Figure 3.8 shows that the 15 h of immersion in Ce(III) electrolyte can be split into 3 stages, each of them being represented by a certian trend in optical changes and OCP (as witnessed in Figure 3.6). The three stages can be summarised as follows:

- **Stage I**: As soon as AA 2024-T3 is exposed to the electrolyte local anodic and cathodic areas together with conductive paths between these two are established. In neutral aerated electrolytes, the (predominantly) cathodic IM particles will support oxygen reduction (step 1), thus causing a fast local increase of the solution pH in their surrounding. The local increase in pH triggers the precipitation of $Ce(OH)_3$, so that its selective deposition over the cathodic areas occurs (step 2). The formation of a thin layer of $Ce(OH)_3$ on the cathodic IMs limits the diffusion of oxygen towards these, so that its consumption is remarkably decreased and so the electrochemical and optical activity (AA% $= 0$). Stifling of the cathodic sites by $Ce(OH)_3$ precipitation causes a larger percentage of anodic surafce to be exposed to the electrolye, which might explain the stable decrease of OCP to more anodic values.
- **Stage II**: Formation of ceria layers as a consequence of oxidation of Ce(III) to Ce(IV) start to be favoured after some time. Oxidation of Ce(III) is promoted by the production of H_2O_2 from oxygen reduction reactions: the cathodic

reaction, inhibited by the $Ce(OH)_3$ layer formed in Stage I, becomes more likely to happen in stages (two-electron pathway, instead of four-electron pathway), thus favouring the production of H_2O_2 as an intermediate of reaction (see equation (1.5)). The strong oxidising power of H_2O_2 can in turn promote the prompt oxidation of Ce(III) to Ce(IV) (according to equation (1.8)) and, afterwards, the precipitation on the IM particles into a stable oxide (CeO_2) form (step 3 in Figure 3.8). Evidence of this phenomenon is provided by a linear but slow increase of the AA% (IM-localised optical changes of low intensity) and by the OCP change towards the more noble direction.

- **Stage III**: Towards the end of the immersion time, the rate of optical changes (AA%) slows down and the OCP flattens into a plateau with small instabilities shaped as spikes ($\approx$ 10 mV). Since a loss in protection was discarded from the experimental observations (see Figure A.2 and section A.3) it can be envisaged that this stage is dominated by a thickening and consolidation of CeO_2 layers with the occurrence of small localised breakdowns of the oxide phase, which promptly re-passivate thanks to the fast supply of Ce^{3+} from the electrolyte (step 4 in Figure 3.8).

3.3.3 Stability of Ce(III) inhibitive layers after drying and re-immersion in salt solution

3.3.3.1 Effect of drying and re-immersion in salt solution on the inhibiting layer stability

(In)stability of Ce(III) layers formed on AA 2024-T3 surface was studied by drying and re-immersing the samples in non-inhibited NaCl solution as described by the immersion protocol in Figure 3.1b. Figure 3.9 shows the opto-electrochemical data for a re-immersion in NaCl of the sample previously exposed to 1 mM $Ce(NO_3)_3$. Figure 3.9a, in particular, displays the OCP and AA% plot during the 5 h re-immersion time in NaCl solution. Figure 3.9b shows the original (row 1) and processed (row 2) images at the beginning (t = 0 s) and at the end (t = 18000 s) of the immersion. Figure 3.9c is a comparison of a sample exposed to a NaCl solution for 3 h with (red) and without (blue) previous exposure to $Ce(NO_3)_3$.

Exposure to NaCl after drying shows an increasing OCP during the 5 h immersion (see Figure 3.9). The OCP signal is slightly noisy but overall free of transients. It also seems to increase more rapidly in the beginning by forming a sort of "shoulder" during the first 1800 s (indicated by a green vertical bar in Figure 3.9a), then it keeps increasing of approximately 150 mV until it progressively stabilises around -0.45 V *vs* Ag/AgCl after 10000 s. The AA% curve (Figure 3.9a) shows a slow and limited increase in the first 1800 s (see green vertical bar in Figure 3.9a), after which it starts to grow more distinctively in a linear trend, taking the value of AA% just above 6% at the end of the 5 h immersion.

Optical images in Figure 3.9b confirm the re-gained optical activity of the aluminium substrate. The original and processed images at 1800 s show optical changes of high intensity (purple-blue) already at this time, but only confined to a few IMs. The changes spread to a larger number of IMs after 1800 s with high intensity. It has to be pointed out, though, that a good number of IMs is still unaffected at 18000 s (*i.e.* 5 h), in spite of the high degree of change (purple-blue) observed in other areas.

Figure 3.9c shows that 3 h of exposure to NaCl solutions causes a linear kinetic of optical changes both with and without previous exposure to $Ce(NO_3)_3$. However, the the exposure to cerium remarkably slows down the rate of optical changes ($3.7 \cdot 10^{-4}$ %/s) compared to a pristine surface ($\approx$ 0.003 %/s).

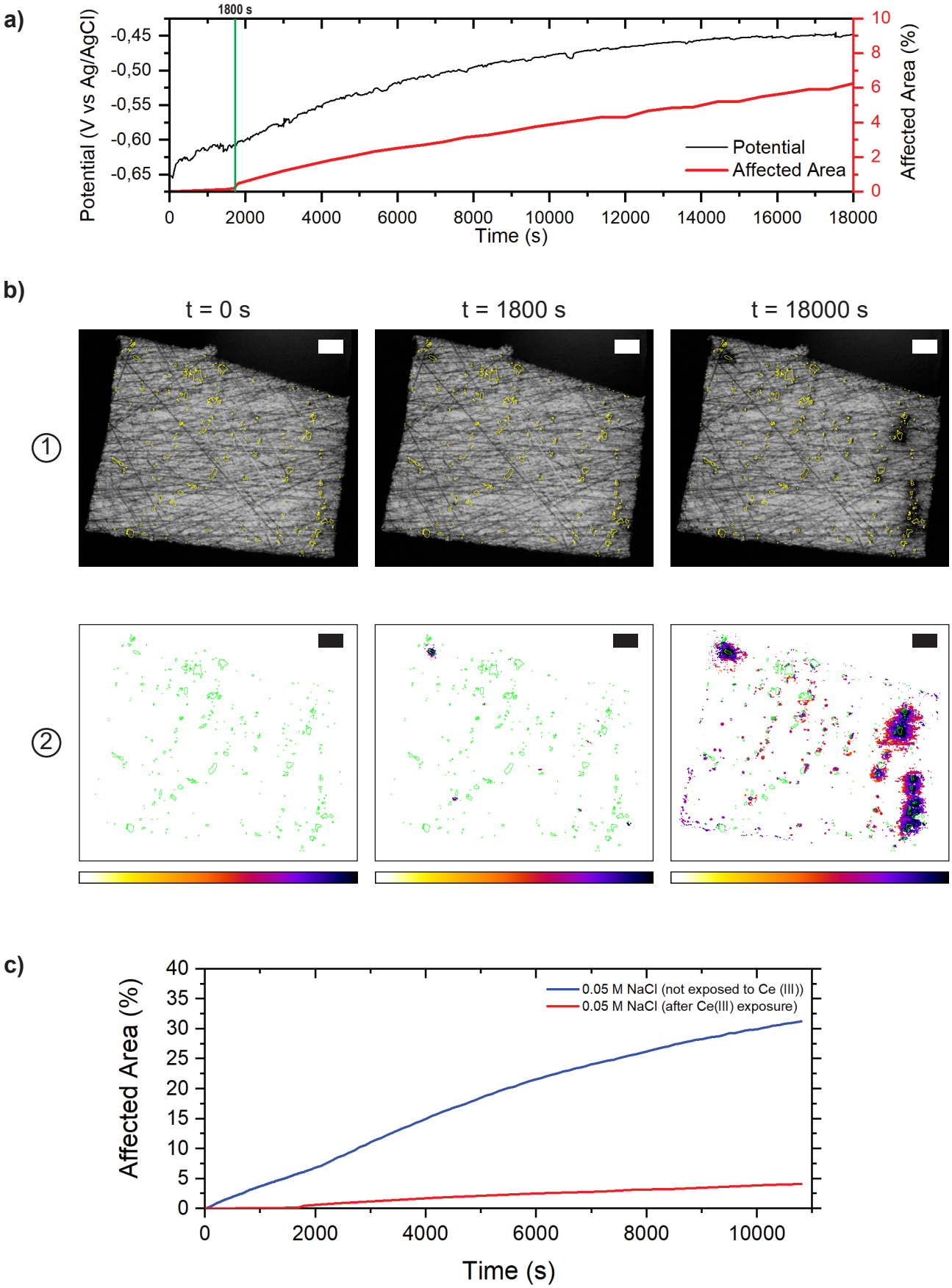

Figure 3.9: a) OCP-AA% plot and b) optical original (row 1) and processed (row 2) images for 5 h re-immersion in 0.05 M $NaCl_{aq}$. The scale bars in b) represent 50 μm. c) Comparison of AA% in the first 3 h of immersion in blank solution for samples with and without previous exposure to $Ce(NO_3)_3$.

Overall, the opto-electrochemical results suggest that re-exposure to an inhibitor-free solution of the Ce(III)-passivated

samples causes a re-activation of the surface after short immersion times. The only partial attack of the IM phase, however, denotes that the protection provided by Ce(III) inhibitor is just progressively and locally lost in time, so that the onset of corrosion on some IM particles might be observed with a certain delay. This observation is confirmed by Figure 3.9c, where a linear trend of AA% is observed in both corroding samples, but with much slower kinetics (lower slope) in case of the sample previously exposed to $Ce(NO_3)_3$.

Different hypotheses were thought of to explain these observations:

- Ce-based inhibition layers are lost due to a poor adhesion of the deposits to the AA 2024-T3 surface. This option sounds reasonable, because the nature of the Ce-IM interface (thus the adhesive properties) is not completely understood.
- Ce oxy-hydroxide layers undergo a progressive re-dissolution after re-exposure to NaCl, which causes the IM phase to be slowly uncovered, thus reactivating micro-galvanic effects. This option would explain both the non-uniformity of the attack (depending on the thickness of the deposits at each IM particle) and the slower but linear optical kinetics (Figure 3.9c).
- Ce(III) inhibitive deposits do not completely erase the micro-galvanic effects between IMs and the Al-matrix, so that they become again influential once the supply of Ce^{3+} ions from the environment becomes scarce.

In general, the topic of instability of Ce-layers is so little addressed in literature that it is difficult to give a correct interpretation to the observed re-appearance of corrosion. Furthermore, the possible scenarios described above take place at such a localised scale (*i.e.* on each single IM particle) that it is also arduous to understand the actual reason behind this loss in protection with only optical and/or electrochemical techniques. For this reason, it is attempted in the following paragraph to shed some light over this problem with the approach of localised electrochemistry.

3.3.3.2 IM-matrix local potentials studied with Scanning Kelvin Probe Force Microscopy

Local changes in surface Volta potential ($\Delta\psi$) after exposure to $Ce(NO_3)_3$ and subsequent re-exposure to NaCl solutions were monitored with scanning Kelvin probe force microscopy (SKPFM). Due to the sub-micron (< 0.1 μm) lateral resolution of this technique, the area scanned with SKPFM can be very small, thus allowing to study the changes in Volta potential at a very local scale, *i.e.* on the single IM constituent.

Figure 3.10 shows the results of SKPFM measurements on the same IM particle at different immersion steps, namely after polishing (*i.e.* before immersion in $Ce(NO_3)_3$, Figure 3.10a), after 15 h immersion in $Ce(NO_3)_3$ (Figure 3.10b) and after 30 minutes of subsequent re-immersion in NaCl (Figure 3.10c). The results are expressed in terms of Volta potential maps and Volta potential profiles. Figure 3.10a clearly displays the IM particle on the Volta potential map, which is characterised by a more negative Volta potential (black in the colour bar) compared to the surrounding Al-matrix (orange-red). The potential profiles along the lines labelled as 1 and 2 quantify such Volta potential difference ($\Delta\psi$) between the IM particle and the Al-Matrix to be of approximately 60 mV. Figure 3.10b shows that after 15 h immersion in $Ce(NO_3)_3$ the Volta potential map displays a uniform colour spread all over the analysed surface. Figure 3.10c shows that a difference in potential between the IM particle and the surrounding matrix has become clear again after 30 minutes of re-immersion in NaCl from the Volta potential map. The particle still has a more negative potential (brown) compared to the solid solution matrix (orange), but the potential profile (Profile 1) across the IM particle, not only denotes a $\Delta\psi$ of $\approx$ 60 mV across the IM-matrix interface, but also a $\Delta\psi$ of $\approx$ 30 mV within the particle.

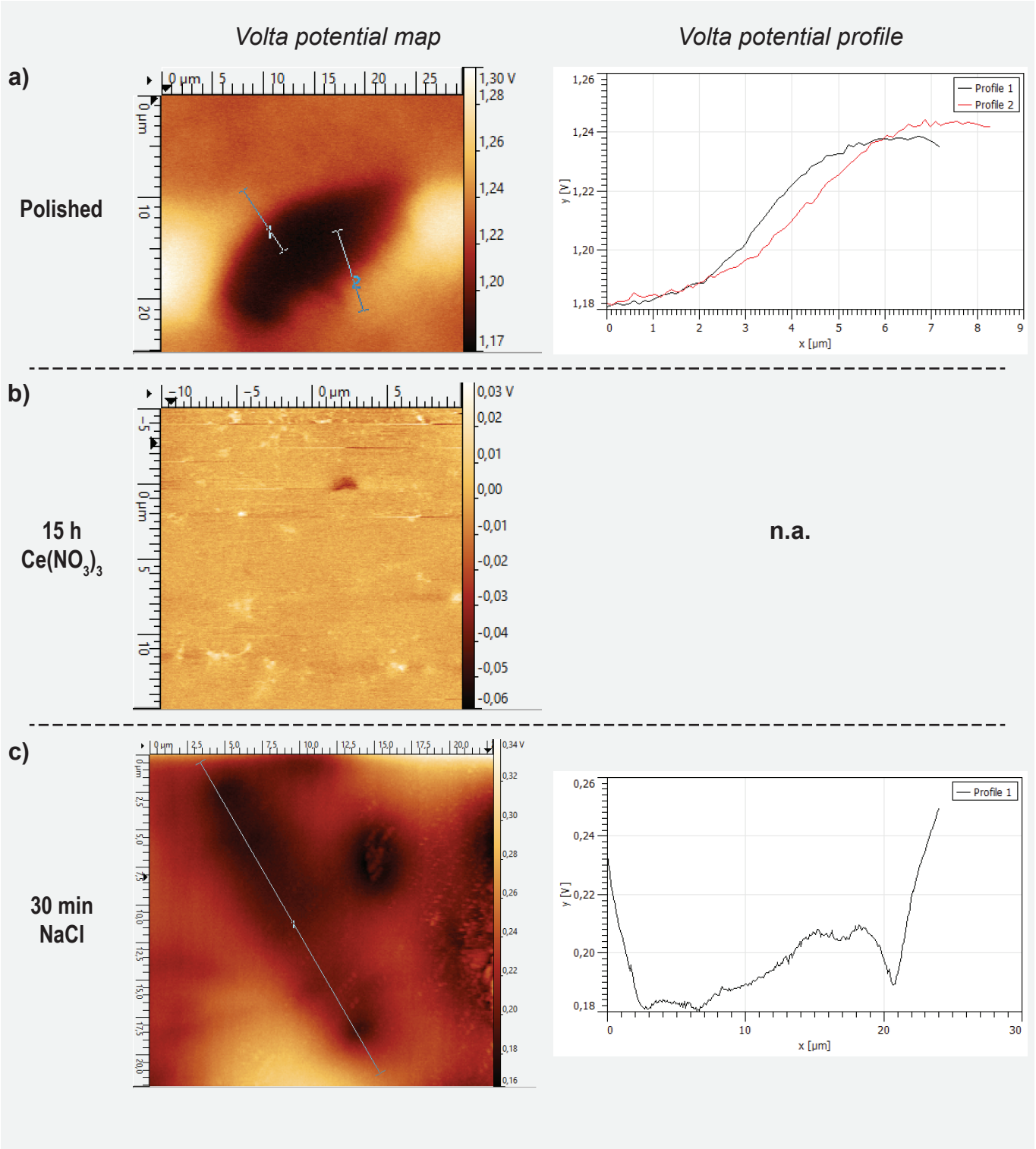

Figure 3.10: Volta potential map and profiles for a single IM particle a) before immersion (*i.e.* after polishing), b) after 15 h immersion in $Ce(NO_3)_3$ and c) after re-immersion in 0.05 M $NaCl_{aq}$ for 30 min.

The more negative potential of the particle analysed before immersion (Figure 3.10a) could underline its anodic character with respect to the matrix (*e.g.* S phase). Although a correlation is believed to exist between the corrosion potential and the Volta potential measured with SKPFM, there are some other studies [95, 96] suggesting that the S phases after polishing have an initial more positive potential than the matrix, which tends to become more negative after progressive exposure to NaCl solutions [97]. Considering the high surface sensitivity of SKPFM, the conflict between the observed data and the ones reported in literature may depend on several factors, for example the nature and dielectric properties of the surface oxide formed on the IMs [98], surface contamination from polishing [98], the lack of solvatation from solvent molecules and the establishment of an electrical double layer [99], *etc.*. However, it is more important to see that a difference in potential between the IM phase and the Al-matrix is visible, thus confirming the existence of local galvanic

interactions between these two phases. This difference in potential before immersion is, indeed, the driving force that triggers corrosion phenomena, as well as protection by Ce(III) inhibitors. The uniform colour in the Volta potential map after 15 h in $Ce(NO_3)_3$ represents an artifact returned by the machine due to the impossibility of measuring the Volta potential across the scanned area. This result is likely to be ascribed to the formation of a non-conductive phase (most likely an oxide) on top of the analytical surface, thick enough to impede the successfulness of the measurement. Such outcome might confirm the formation of an inhibitive cerium oxide phase during immersion in $Ce(NO_3)_3$, which is not only deposited on the IM phase, but also on the Al-matrix. In order to explain the effect of immersion in $Ce(NO_3)_3$ on the SKPFM measurement, shorter immersion times were also performed (20 minutes) and the results are displayed in Appendix A.5 (Figure A.7). It can be concluded that progressive build-up of Ce(III) deposits decreases the $\Delta\psi$ between the IM an the matrix (from 60 mV to 40 mV), until they become too thick to enable the measurement.

More interestingly, re-immersion in NaCl for 30 minutes reveals that a $\Delta\psi$ can be once again measured between the IM and matrix phases, with the IM being more anodic than the matrix. The recurrence of $\Delta\psi$ after re-exposure can only be explained by postulating a dissolution of the Ce(III) deposits from the surface. Had these deposits not been lost, a signal similar to the one observed in Figure 3.10b could have been expected due to the non-conductive nature of the oxide formed. Moreover, the heterogeneities in potential within the same particle ($\Delta\psi \approx 30$ mV) induce to think that Ce(III) dissolutions also occurs progressively in time, so that some regions are more cathodic than others due to some Ce(III) undissolved remnants. This result might also corroborate the linear trend of AA% observed in 3.9c, as a sign of an optical re-activation of the surface slowed down and limited by the progressive re-dissolution of Ce(III) inhibitive deposits. Measurements were also conducted after 5 h re-immersion in NaCl, but the high degree of pitting did not allow to finalize the measurement (see Figure A.8).

On balance, it can be concluded that localised electrochemistry suggests a progressive dissolution of Ce inhibitive deposits to be occurring once the Ce-inhibited surfaces are re-immersed in inhibitors-free electrolytes. The Ce oxy-hydroxide deposits might get into a hydrated state upon further exposure, thus increasing their solubility. They, therefore, will undergo a progressive thinning process, which is still capable of providing protection by delaying the onset of corrosion until all the deposits are lost. Complete loss of inhibitive deposits will favour nucleation and growth of corrosion pits localised at the IM phase. The localised electrochemistry approach is also well in agreement with the results obtained with the opto-electrochemical analysis, where an heterogeneous but delayed onset of localised corrosive phenomena was observed.

3.4 Final Remarks and Conclusions

In this chapter, the use of opto-electrochemical analysis was employed on studies with $Ce(NO_3)_3$-doped electrolytes, in order to extend its use to study systems with corrosion inhibitors. Protection on AA 2024-T3 was tested under immersion for 15 h at three different $Ce(NO_3)_3$ concentrations. The opto-electrochemical results not only showed different degrees of protection at different Ce(III) concentrations, but also similar and reproducible electrochemical (OCP) and optical (AA %) trends, as a sign of the identical underlying inhibition mechanism provided by Ce(III). The Langmuir adsorption theory resulted in being a good approximation to explain the different degrees of protection during the initial stages of immersion: the main outcome is that there is a critical value of concentration (C_{crit}) that determines the protection or non-protection of the alloy, depending on the supply of Ce^{3+} ions from the solution.

Further characterisation was employed to understand the optical and electrochemical data observed during 15 h immersion in 1 mM $Ce(NO_3)_3$. EIS and opto-electrochemical analysis with H_2O_2 allowed us to associate the IM-localised optical changes and the increase in electrochemical potential to the H_2O_2-promoted oxidation of Ce(III) into Ce(IV) and its precipitation as CeO_2. A comprehensive mechanism for Ce(III) inhibition process was also proposed, confirming the two-electron pathway theory proposed in literature. These findings not only prove the feasibility of studying corrosion inhibition with an optical-electrochemical approach, but also enormously strengthen the power of this type of analysis, as it might enable to acquire fundamental information regarding the phenomenology of inhibition.

Stability of Ce(III) passivation layers on AA 2024-T3 was finally studied by means of opto-electrochemical analysis and SKPFM. Localised electrochemistry techniques, such as SKPFM, enabled to confirm and corroborate the observations made from opto-electrochemical tests, specifically that re-exposure of Ce-inhibited surface to a sodium chloride solution causes a progressive re-dissolution of Ce(III) inhibitive deposits, which delays the onset of pitting corrosion in time, but eventually leading to a total loss in protection. The global optical data of the whole exposed surface and the optical information gained in real-time have demonstrated to be key aspects in the determination of the causes for inhibition reversibility, thus consolidating the complementarity of optical imaging and electrochemistry.

Chapter 4

Stabilisation of protective Ce(III) layers with organic compounds

Since Ce(III) inhibitive layers demonstrated to be unstable upon re-immersion in NaCl, in this chapter, a step forward is taken by trying to make them more stable on the surface, thus preventing their re-dissolution and enhancing their long-term protective properties. In particular, the problem of Ce(III) stabilisation is tackled by looking at the interaction between cerium and three different organic compounds: alginate, phytic acid and 2,5-Dimercapto-1,3,4-thiadiazole.

4.1 Introduction

The problem of irreversibility of inhibitors is not new to the field of corrosion science, although most of the time is not very well addressed, since in practice a continuous supply of inhibitor is expected (*e.g.* primers with Cr(VI) salts). From the results shown in section 3.3.3, it seems clear that Ce-based inhibitive layers do not possess this property, in fact protection was shown to be lost after drying and re-immersion in a non-inhibited salt solution.

Many studies in literature already propose to exploit the synergistic action of multiple corrosion inhibitors to efficiently increase the protection of metals and delay the onset of corrosion. For example, in the work of E. L. Ferrer *et al.* [100], a synergistic effect between Ce(III) and diethyldithiocarbamate trihydrate (DEDTC) is suggested as a consequence of the improved active corrosion protection achieved on aluminium 2024-T3 at both short and long immersion times. These results were accomplished by studying a new concept of double inhibition process by controlling the release of different inhibitors from zeolitic microcarriers. Analogous conclusions were also reached in the work of M. AbdolahZadeh *et al.* [101], in which a synergistic effect between Ce(III) and 2-Mercaptobenzothiazole (2-MBT) was successfully demonstrated. In the works of L. B. Coehlo *et al.* [66, 102], on the other hand, synergy between Ce(III) and benzotriazole (BTA) was investigated on Al-Cu model systems and it was concluded that constructive effect between these two inhibitors can only be seen after 24 h of immersion in the inhibitor-containing electrolyte, while in the first 24 h a deconstructive effect was revealed, perhaps due to the competition between Ce and BTA in the early blocking of the Cu-rich cathodic areas. Time of Flight Secondary Ion Mass Spectrometry (ToF-SIMS), moreover, enabled to attribute such synergistic effect to the formation of Cu-BTA complexes on top of Ce deposits after 24 h, which implies Cu to still be able to pass into the solution.

Similar synergetic protection can be achieved with multifunctional rare earth compounds as corrosion inhibitors, like rare earth organo-phosphates or organo-carboxyalte [103, 104]. In a few works [94, 105], cerium dibutylphosphate ($Ce(dbp)_3$) was especially found to provide good active corrosion protection to aluminium 2024-T3, most likely due to the selective protection of the IM phase by Ce(III), while the organo-phosphoric counter ion passivates both the Ce(III) deposit and the Al-matrix.

Despite opening promising perspectives for future research, studies on synergetic effects between Ce(III) and other inhibitors still mainly focus on continuous immersion testing in inhibitor containing solutions or using coatings loaded with inhibitor, thus providing continuous supply during the immersion time. Achieving and proving a synergistic effect between Ce(III) and other inhibitiors, indeed, does not necessarily imply the achievement of an irreversible system - the protection provided by Ce(III) combined with other compounds can be lost when the metal substrate is re-exposed to a corrosive environment if such complex layers themselves are not stabilised or passivated on the surface. For this reason, in this chapter it is attempted to find strategies to make such layers more stable by investigating not necessarily the synergy, but rather the interaction and permanence of Ce(III) with other organic compounds. The idea is to use these compounds to "passivate" and fixate Ce inhibitive layers so that they will have an increased stability upon further exposure to corrosive electrolytes, providing protection for prolonged time. To this scope, three chemical species, which from now on will be called "passivators", were selected for further investigation because of their potential affinity with cerium. These are: sodium alginate, phytic acid (PHA) and 2,5-Dimercapto-1,3,4-thiadiazole (DMTD). The nature of these organic compounds is quite different from one another, as well as their mechanism of interaction with cerium species, therefore the reason behind their selection will be discussed more in detail in the following paragraphs.

4.1.1 Alginate

Strictly speaking, "alginate" is a collective term for a family of polysaccharides produced by brown algae. It is, therefore, used to indicate a natural and water-soluble polymer consisting of polysaccharide-like linear chains with typical sugar moieties and many pending hydroxyl and carboxylic groups [106]. In essence, alginate is recognised to be a copolymer, made up of β-D-mannuronic acid units (M units) and α-L-guluronic acid units (G units), whose chemical structures are shown in Figure 4.1a. The sequence of these units along the chain is not always homogeneous - it is accepted that sequential M-M or G-G blocks can occur, as well as alternating M-G blocks [107, 108] (see Figure 4.1b).

In the last decades, alginate has been extensively studied as a material for many different reasons. It has a great interest in the biomedical/pharmaceutical field [109–112], as well as food industry [113], because of its biocompatiblility and non-toxicity. Most recent research has shown its potential also in other fields, like anticorrosion coatings [114, 115] and self-healing composites [116, 117], asphalts [118, 119] and concrete [120].

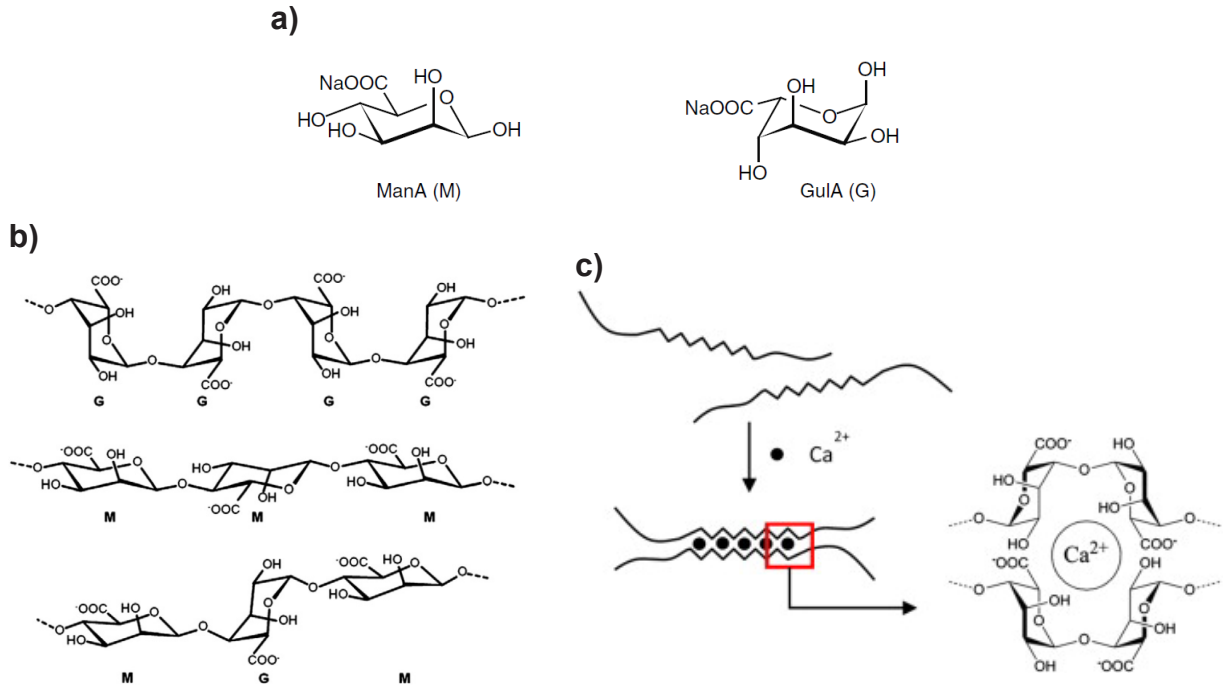

Figure 4.1: a) Building blocks (units) of alginate molecules, precisely mannuronic acid (ManA, M) and guluronic acid (GulA, G) [106]. b) Representation of the possible chain sequences of alginate (G-G, M-M and M-G) [121]. c) Schematic illustration of the ionic crosslinking process in alginates and the formation of "egg-box" structures around multivalent cations [121].

For the present research, sodium alginate was chosen for its capability to cross-link and become insoluble in presence of multivalent cations. It is well-known that G-units of alginates can orient their functional groups in such a way that typical "egg-box" structures around cations are created, thus achieving a gel state (Figure 4.1c). The gelling of alginate in calcium chloride has been thoroughly explored in literature, but gelling in presence of Ce^{3+} ions is less common. Early own lab experiments with alginate solutions showed evidence of cross-linking of the latter in presence of Ce^{3+}, hence the choice of investigating alginate as a passivator for Ce inhibitive layers. If cross-linking can be achieved with small additions of alginate in solution, fixation of Ce layers on the surface before they completely dissolve in the solution can be reached. Moreover, alginate functional groups may provide further interaction with the entire 2024-T3 surface, thus a multi-functional type of passivation.

4.1.2 Phytic acid

Myoinositolhexakisphosphate, also known as phytate or phytic acid (PHA), is an organic compound widely distributed in the plant kingdom, serving as the main storage of phosphorous in vegetal tissues like cereals, seeds and grains [122, 123]. Its chemical structure is shown in Figure 4.2a. It can be seen from here that phytic acid entails six pending phosphoric groups per molecule. Metal - phosphate interactions have always been attractive in the field of corrosion protection, as they proved to bind to the metal substrate and form stable and protective mineral/ceramic-like films, as in the case of phosphate conversion coatings [124, 125]. In a similar way, PHA can be employed for corrosion inhibition studies thanks to the high number of phosphoric groups capable of achieving metal-(organo)phosphate complexation. Previous research studies showed the suitability of PHA in the formation of a PHA-based conversion coating on AA 2024-T3 [126] and as a sealing agent for anodized aluminium [127]. It was also demonstrated to provide synergetic protective properties in combination with polyaniline as a co-synthesized pigment for the protection of Q235 carbon steel [128, 129]. Extensive reasearch using PHA was also carried out by the research group pf H. Yang *et al.* [130–137]. In particular they studied the effect of PHA on the corrosion inhibition of Cu surfaces [130–133], as well as its adsoprtion behaviour on Ag and Au surfaces for biosensing applications [134–137]. From studies on corrosion inhibition of Cu, especially, it was demonstrated that PHA forms self-assembled chemisorbed monolayers *via* interaction between both P-O groups and the cyclohexyl ring with the Cu surface [130, 131].

Also in this case, early lab own experiments showed that mixing same volume of equimolar concentrations of PHA and $Ce(NO_3)_3$ solutions gave evidence of the increased turbidity of the solution, as a sign of the formation of Ce(III)-PHA precipitates. The interaction between PHA and Ce(III) was also investigated in the research of J. Ou and X. Chen [138], where they exploited a layer-by-layer approach to form Ce-PHA nanocomposite coatings on Mg alloys endowed

with superhydrophobic properties. For these reasons, PHA was studied in the present research to test if organo-phosphate complexes with Ce inhibition layers can be formed and if they provide fixation of Ce(III) on the surface.

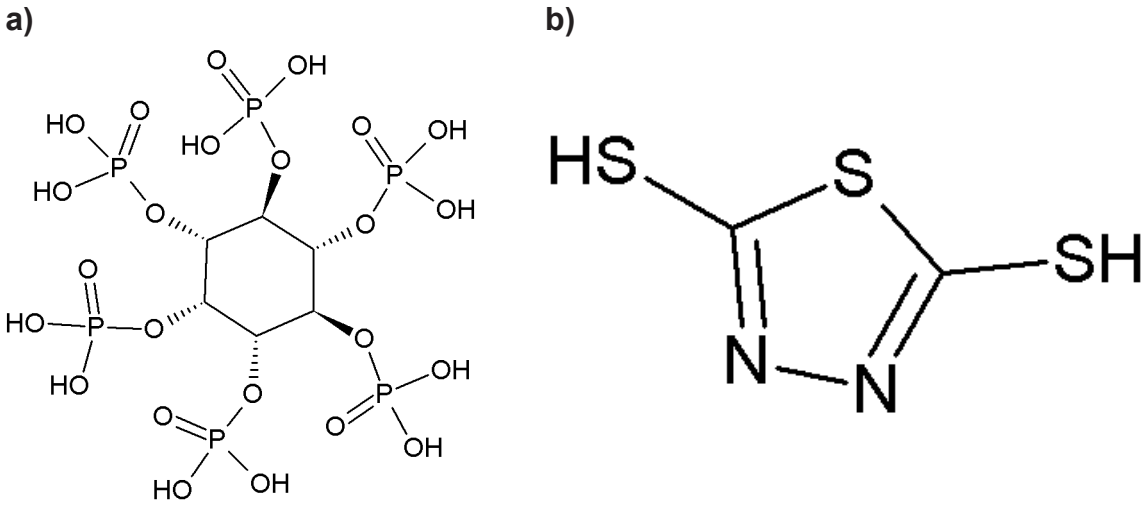

Figure 4.2: Molecular structures of a) phytic acid and b) DMTD

4.1.3 2,5-Dimercapto-1,3,4-thiadiazole

2,5-Dimercapto-1,3,4-thiadiazole (DMTD) is a thiadiazole derivative consisting of a conjugated heterocyclic ring with sulfur and nitrogen atoms (chemical structure shown in Figure 4.2b), which has been gaining quite some interest lately as a corrosion inhibitor for different metal alloys, like AA 2024-T3 [89, 139, 140], bronze [141], silver [142, 143] and mild steel [144]. Its effective inhibition is provided by the abundance of heteroatoms in the molecular compound (like N and S), which promote the adsorption *via* complexation with the atoms of the metal. DMTD, especially, shows higher affinity for chelation with Cu [145], thus stifling oxygen reduction reaction on pure Cu thanks to the low solubility of the so-formed complexes [139]. The formation of metal-organic complexes on the surface was demonstrated to be exotermic ($\Delta H < 0$) and spontanoues ($\Delta G < 0$), leading to a chemisorption process of the species on the metal substrate, which involves both an electrostatic interaction and a donor-acceptor interaction between the metal substarte and the oragnic molecule [144]. In the study of D. Snihirova *et al.* [140], inhibition of AA 2024-T3 with DMTD was studied, together with the synergetic effect between DMTD and Ce(III) inhibitors. They concluded that the combination of these two inhibitors is capable of providing a synergistic effect, especially in long-term immersion tests, perhaps as a consequence of the cathodic nature of both Ce(III) and DMTD in suppressing the cathodic reactions on Cu-rich IMs. Although this result was expected as both inhibitors show long-term protection *per se* [140], the reason behind such synergistic effect is still unclear, especially it is questioned whether the synergy stems from an interaction between Ce(III) and DMTD, or simply because of their summed inhibiting action. For this reason, passivation of Ce layers with DMTD was decided to be investigated further in this research.

4.2 Experimental

All the test methodologies reported in this chapter were carried out with the same opto-electrochemical setup described in Chapter 2. The sample preparation steps, test parameters and post-processing analysis are the same as described in section 2.2 and, therefore, they will not be reported here. Conversely, the additional materials, methods, experimetal details and protocols of analysis presented in this chapter will be described more in detail.

4.2.1 Materials and preparation of electrolytes

Alginic acid sodium salt from brown algae (medium viscosity), Phytic acid sodium salt hydrate and Cerium(III) nitrate hexaydrate (99% trace metal basis) were purchased from Sigma Aldrich. 1,3,4-Thiadiazole-2,5-dithiol for synthesis (DMTD) was purchased from Merck Millipore. Sodium chloride was purchase from VWR Chemicals. All the chemicals mentioned were used without any further purification. Millipore® Elix 3 UV filtered water was used to make electrolytic solutions.

Starting from 0.05 M $NaCl_{aq}$ electrolytes (NaCl), electrolytic solutions with additions of different inhibitors/passivators were prepared: $Ce(NO_3)_3$ was used at a concentration equal to 1 mM, sodium alginate was diluted at a concentration

equal to 0.1 wt.% ($\approx$ 5-8 $\cdot$ 10^{-6} mol L^{-1}), PHA was used at a concentration of 1 mM (pH $\approx$ 5), while DMTD was used at a concentration equal to 0.1 mM due to its lower solubility.

4.2.2 Protocols of analysis and methods

4.2.2.1 Immersion protocols for opto-electrochemical analysis

The protocols of analysis used to test all three passivators are reported in Figure 4.3.

First, the potential of the passivators was tested (*i.e.* without previous exposure to Ce(III)) as shown in Figure 4.3a. This test consists of an 8 h immersion in the passivator solution followed by a re-exposure to NaCl for 15 h.

The Ce(III)-passivator interaction was tested with the protocol shown in Figure 4.3b. This consists of a first immersion in cerium solution for 15 h, followed by an immersion in the passivator solution for 8 h, followed in turn by a re-immersion in NaCl solution for further 15 h. Before the test and at every change of electrolyte, the electrolytic cell was flushed 3 times with demineralised water in order to clean it from contaminants and remove the excess of inhibitor/passivator. During the change of electrolyte, the sample was removed from the cell and gently dried with N_2 gas. Each test was repeated at least twice (for each passivator).

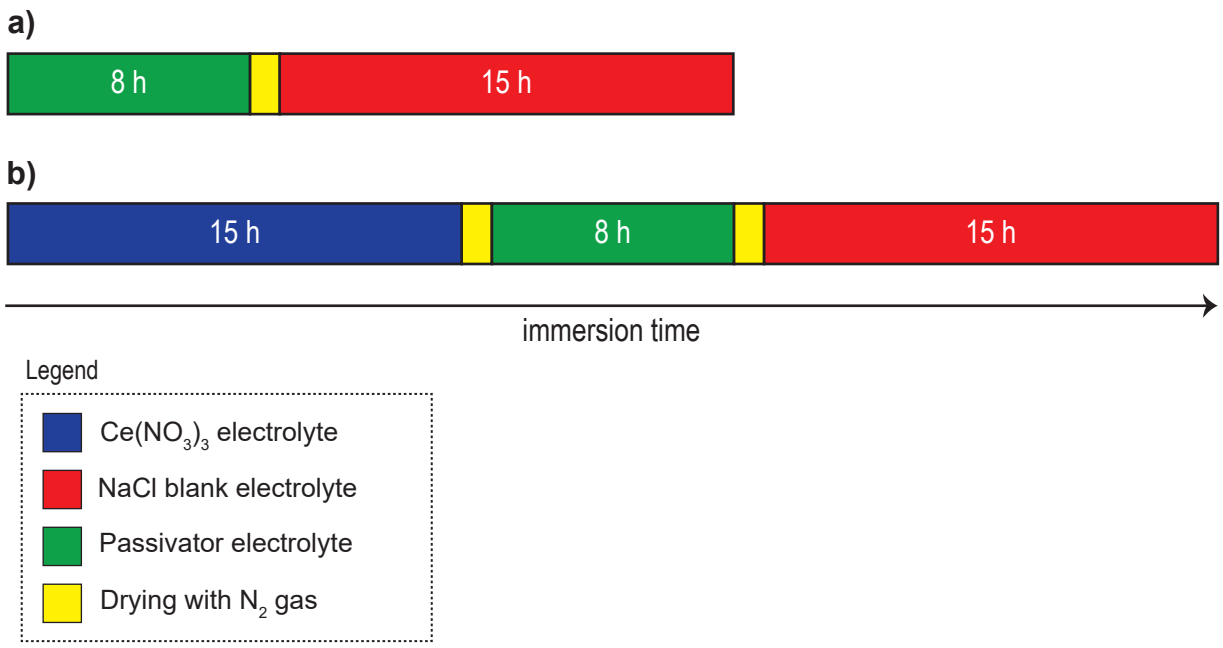

Figure 4.3: Test protocols for a) evaluation of the passivator protective performance on its own, b) evaluation of the Ce(III)-passivator interaction and stabilisation.

The chosen passivators were tested according to this protocol (*i.e.* with and without previous exposure to cerium) for the following reasons: i) the passivators may not show protection of AA 2024-T3 by themselves, but a possible interaction with cerium layers or ii) the they might already show inhibition properties by themselves. In the first case, the passivators were immediately tested in combination with $Ce(NO_3)_3$ to see if an interaction between the two exists. In the second case, however, it is worthy to understand whether the passivators also show stability upon re-exposure to NaCl. Therefore, this second class of passivators was further re-exposed to NaCl for 15 h. The logical process just described is schematically depicted in Figure 4.4 and the results will be helpful in understanding the Ce(III)-passivator constructive or destructive interaction.

4.2.2.2 SEM-BSE *post mortem*

SEM-BSE analysis *post mortem* was carried out by means of a different scanning electron microscope (JEOL JSM-IT100), with the same working conditions mentioned in Chapter 2. Also for *post mortem* analysis, the same stitching procedure was applied to reconstruct the exposed surface, as well as the same optical-fitting procedure mentioned in section 2.2.4.4.

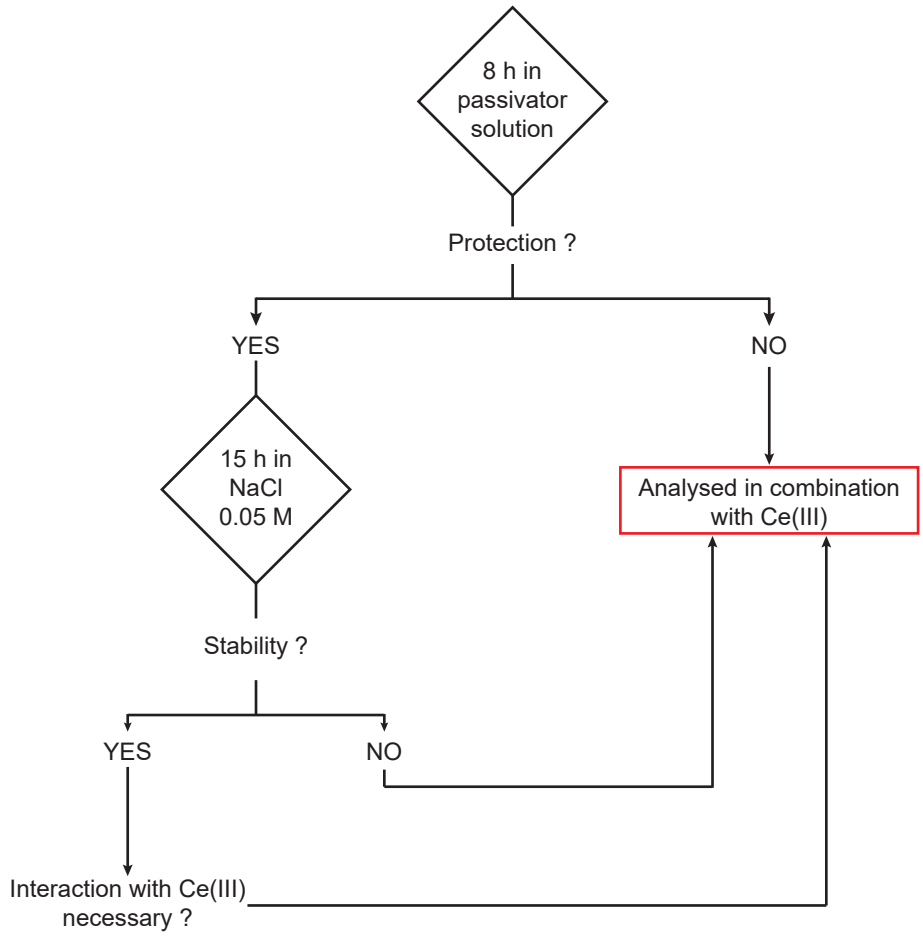

Figure 4.4: Flowchart explaining the logical process followed in testing the protective properties of passivators before analysing their interaction with Ce(III).

4.3 Results and Discussion

4.3.1 Direct exposure of AA 2024-T3 to passivator-containing solutions

Eight hours immersion in each passivator-containing electrolyte was performed as a first test. The optical and electrochemical data obtained from these tests are reported in Figure 4.5.

Figure 4.5a, relative to the immersion in alginate, displays an unstable OCP signal. After a short initial steady increase to more cathodic values ($\approx$ 100 s), the OCP is characterised by high-amplitude transients ($\approx$ 150 mV) between 100-1000 s, followed by a decrease in the transients amplitude and flattening of potential around an average value (-0.45 V *vs* Ag/AgCl). The AA% increases linearly with a rate of approximately $1.6{\cdot}10^{-3}$ %/s, taking the AA% to a value of 12% after 7200 s. Both the electrochemical and optical data were similar to the ones observed in section 2.3 for a corroding sample. In particular the initial steady increase followed by onset of transients and further stabilisation of the OCP could be associated to dealloying, trenching and stable pitting, respectively. Moreover, optical evidence of corrosion features enabled to conclude that localised corrosion is taking place in this electrolyte and the test could be stopped after 2 h already. Proof of the ongoing corrosion is provided by SEM-BSE *post mortem* reported in Appendix B.1 (Figure B.1).

Figure 4.5b displays the potential and affected area for 8 h immersion in PHA. It can be seen that the potential signal looks really unstable, with sharp and short-lived spikes ranging 300-350 mV, *i.e.* higher than the typical amplitude of corrosion transients (100-200 mV). The AA%, on the other hand, remains quite low throughout the test time ($\approx < 1.5\%$ at 28800 s). It is still unclear whether the OCP instabilities are related to localised corrosive events, especially because the AA% plot remains low for the whole test time. Given the almost optically-unaffected surface exposed, it can be presumed that the peaks in the potential plot can be representative of an interaction between PHA molecules and the surface, or perhaps even adsorption-desorption phenomena of PHA on/from the surface at a very local (atomic) scale.

Figure 4.5c shows the electrochemical potential and affected area for 8 h immersion in DMTD electrolyte. After an initial (stable) decrease of the signal (from -0.6 V *vs* Ag/AgCl to -0.75 V *vs* Ag/AgCl), the OCP starts to increase again to more positive values and flattens into a very stable plateau at an almost constant value ($\approx$ -0.62 V *vs* Ag/AgCl). This trend of potential is accompanied by almost inexistent optical changes, which make the AA% stable at 0%. These two trends confirm the excellent inhibition properties of DMTD. The initial decrease of the potential might be associated to a quick passivation of the IM Cu-rich particles by DMTD, due to the higher affinity between thiol groups and Cu [145]. Chelation of DMTD to Cu-rich IMs inhibits the cathodic reactions and makes the OCP become more anodic, in a similar way as the one explained in section 3.3.2 (see Figure 3.8 during Stage I). The further increase in potential and the consequent stabilisation, might be related to a slower complexation of DMTD with the Al-matrix as well, thus leading to the formation of a uniform chemisorbed monolayer across the exposed surface.

From the results explained above and according to the scheme in Figure 4.4, it can be deducted that:

- Sodium alginate does not provide inhibition on its own, so it can be directly tested in combination with Ce(III) as a potential passivator.
- PHA and DMTD seem to provide inhibiting properties on their own, so their stability upon re-immersion must be assessed first.

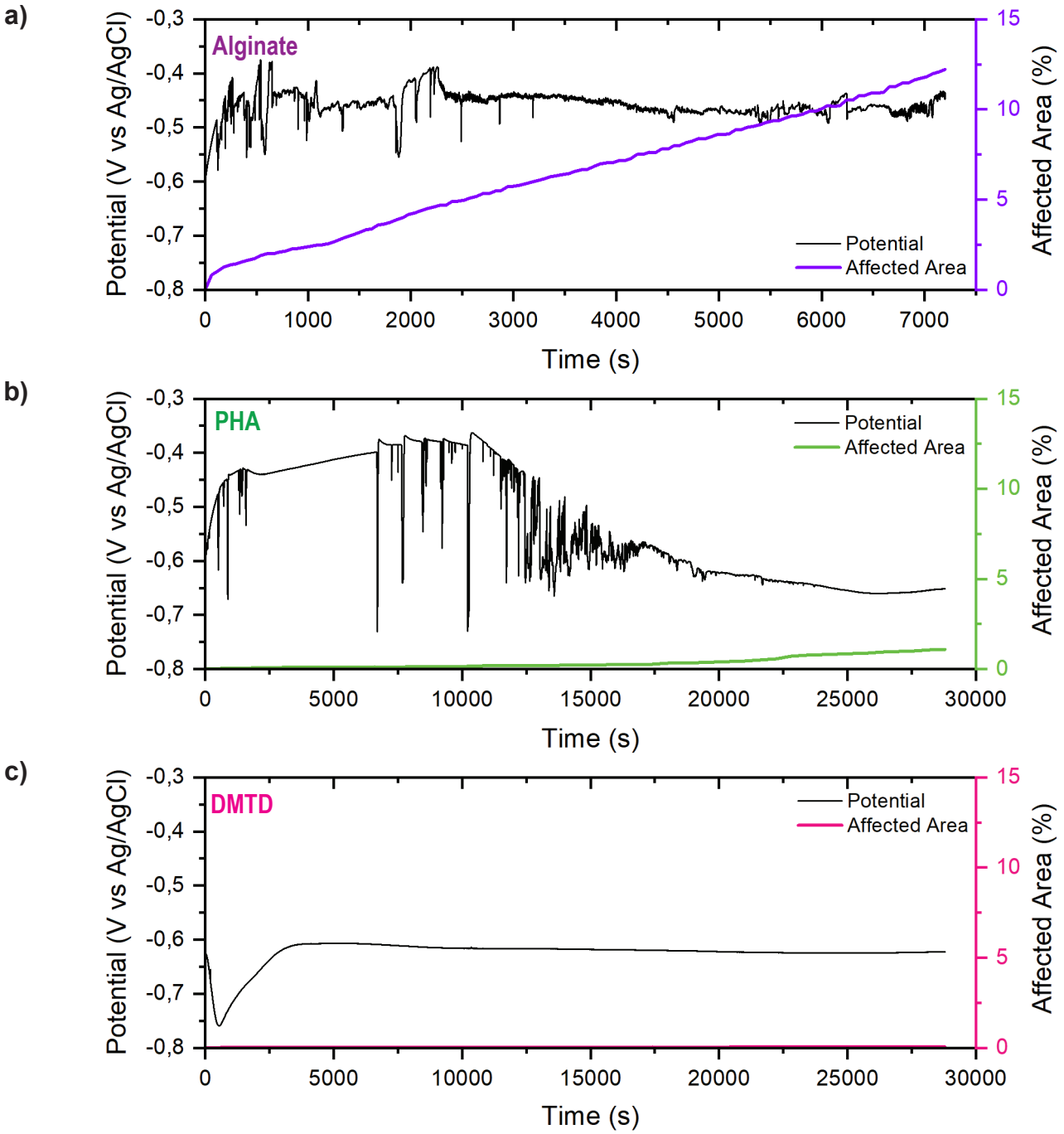

Figure 4.5: Opto-electrochemical data (OCP-AA% plots) for 8 h immersion in a) sodium alginate, b) PHA and c) DMTD.

The optical-electrochemical plots relative to 15 h re-immersion in NaCl solutions after exposure to PHA and DMTD are reported in Figure 4.6a and 4.6b, respectively.

Figure 4.6a for PHA shows that AA% increases linearly and rapidly (0.005 %/s) from the beginning of the test until it reaches high values of AA% and flattens into a plateau around $\approx$ 75%. The potential shows a sharp increase to more cathodic values in the beginning followed by a steep decrease until it stabilises around an average value (-0.6 V *vs* Ag/AgCl). It is interesting to see that stabilisation of OCP happens more or less at the same moment when AA% reaches a plateau. The initial sharp increase and decrease of OCP signal might represent the simultaneous desorption of PHA from the surface and the activation of the surface (corrosion). After all the PHA is lost (desorbed), corrosion can propagate and proceed at a constant value of free corrosion potential E_{corr}. Overall, PHA layers are significantly more unstable than those created with cerium (see section 3.3.3) as indicated by the high level of AA% reached in short re-immersion times.

Figure 4.6b shows the result of re-immersion of the sample treated with DMTD (Figure 4.6b) in NaCl solution. In this case, a pretty stable and almost constant OCP ($\approx$ -0.5 V *vs* Ag/AgCl) throughout the test time can be seen. Such stable signal seems to be perturbed only towards the end of the test (after 40000 s *circa*). In the last hours, a few spikes in the

potential ranging $\approx$ 150 mV start to appear. The global AA% at the end of the test is still very low ($< 2\%$). The stability of both OCP and AA% during re-immersion in NaCl lead to the conclusion that DMTD inhibitive layer is rather stable .

In conclusion:

- PHA is not stable upon re-immersion in NaCl, so its interaction with Ce(III)-layers might lead to increased stability, whereas
- DMTD shows excellent protection on its own even upon re-immersion in NaCl. Testing in combination with Ce(III) passivation layers should aim at revealing a possible further improvement of such stability.

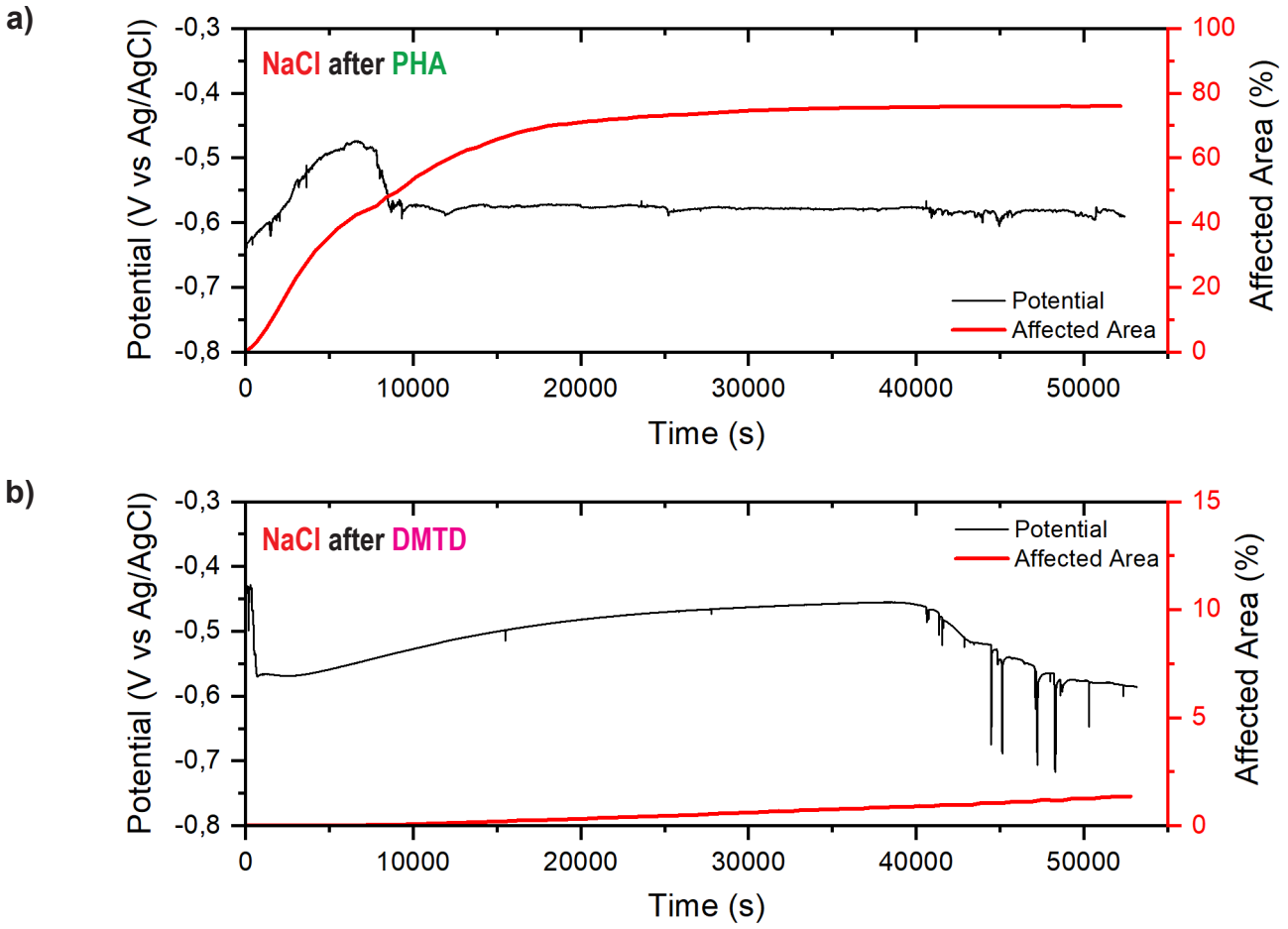

Figure 4.6: Opto-electrochemical data (OCP-AA% plots) for 15 h re-immersion in NaCl, after a previous immersion in a) PHA and b) DMTD.

4.3.2 Exposure of cerium passive layers to organic passivators and their stability after re-immersion in NaCl

The three different passivators were tested in combination with Ce(III) inhibitive layers. They were primarily investigated with real-time opto-electrochemical analysis according to the protocol of Figure 4.3b, then these results were complemented with other analytical techniques like SEM-EDS and Raman spectroscopy. However, except in a few (sporadic) cases, EDS and Raman spectroscopies were not useful and/or as much informative as the opto-electrochemical analysis, so their results are not reported. In the results displayed hereafter, data about immersion in 1 mM $Ce(NO_3)_3$ solutions are also not reported for brevity, as they have already been thoroughly discussed in Chapter 3.

Figure 4.7 contains the opto-electrochemical results obtained for Ce-passivation with sodium alginate. Figure 4.7a, in particular, is the OCP-AA% plot for 8 h immersion in alginate + 15 h immersion in NaCl after previous exposure to Ce(III). Figure 4.7b displays the optical images (original and processed) at the beginning and at the end of each immersion step. The intermediate drying of the sample and cleaning of the electrochemical cell is represented by two vertical red bars in both Figure 4.7a and 4.7b.

In the first 8 h (*i.e.* 28800 s) of immersion in alginate, Figure 4.7a shows that the electrochemical potential is initially quite stable, but becomes extremely unstable between 10000-20000 s until it stabilises again towards the end (after 20000 s). The population of fluctuations observed between 10000 and 20000 s is very dense and covers approximately 200 mV in amplitude. The AA%, however, is flat and stable at 0% and only starts to grow slightly after 20000 s, but remaining overall $< 3\%$. The optical images (Figure 4.7b) at 28800 s suggest that changes of mild intensity have spread on the surface, albeit they don't seem to have any relation with the IM phase, but rather with the Al-matrix. The OCP and AA% signals observed in the first 8 h immersion in alginate are similar to the ones observed in Figure 4.5b for immersion in PHA. The unstable potential accompanied by low AA% was most likely associated to an interaction of the passivator with the surface (adsorption-desorption). Considering the poor performance of alginate in protecting this alloy on its own (see Figure 4.5a), an interaction between Ce and this passivator can be already envisaged in these 8 h of immersion.

Re-immersion in NaCl for 15 h (30000-84000 s) indicates that stability is achieved during the first 2 h (approximately), in which optical changes are quiescent (AA = 0%). After 2 h, protection is suddenly lost and the AA% jumps to 60%. After 40000 s the AA% keeps growing moderately, leading to a final value of $\approx 75\%$ at the end of the test. The potential, on the other hand, is not as unstable as in the previous immersion step: there is an initial decrease of the OCP towards more anodic values up to 40000 s (from -0.5 V *vs* Ag/AgCl to -0.65 V *vs* Ag/AgCl), then the OCP stabilises around a constant average value ($\approx$ -0.65 V *vs* Ag/AgCl). A closer look at the optical images at 84000 s in Figure 4.7b reveals that degradation is distributed all over the surface, exception made for a few unchanged spots, which are actually located in the same positions as the IM particles. These results suggest that presence of cerium promoted the adhesion of alginate on the surface, which is able to provide protection and stability for the first 2 h of re-immersion in NaCl. For longer immersion times, however, protection is abruptly lost, perhaps due to a dissolution of alginate, and severe degradation of the surface is observed. However, the OCP, AA% curve and the optically unaffected IMs at 84000 s are not typical of a corroding AA 2024-T3 sample, as shown in section 2.3.

SEM-BSE *post mortem* analysis was done on the same sample to understand the morphology of the optical events observed. Comparison of SEM-BSE images before and after the test is reported in Figure 4.8. As expected, the spots corresponding to the IM phase seem to be well protected and unattacked (Figure 4.8b), unlike the surrounding Al-matrix which is severely degraded and covered with what looks like a build-up of corrosion products. It is also interesting to note that some IM particles with trenches are visible in Figure 4.8b, as highlighted by the red circles. However, by looking at the respective SEM-BSE image before immerision (Figure 4.8a), it is clear that these IMs were not there before the immersion. It can be presumed that these IMs were actually underneath the surface in the beginning, but the progressive degradation and "digging" in depth caused by corrosive attack on the Al-matrix has led to a progressive surfacing of these, eventually exposing them to the corrosive electrolyte. The protection on the other IMs (*i.e.* the ones already visible before testing) can only be explained by an initial protection by Ce(III)-passivation layers, stabilised during the immersion in alginate.

Although passivation of Ce(III)-layers with alginate seems to be possible, stability of the entire exposed surface (and so protection against corrosion) is not achieved. The severe and abrupt degradation observed on the Al-matrix suggest that corrosion shifts from a localised form to a general form because the (cathodic) IM particles are now well protected. This result denotes that achieving a protection of the IM phase only is not sufficient to stop corrosion phenomena completely. It could be that a total stifling of the IM cathodic particles induces the metal substrate (*i.e.* the Al-matrix) to find new favourable areas to support cathodic reactions, so that the conditions to have general corrosion can be met. Ideally, a passivator with a dual action, *i.e.* capable of passivating both Ce on top of IMs and the Al-matrix, should be sought after in order to hinder general corrosion too.

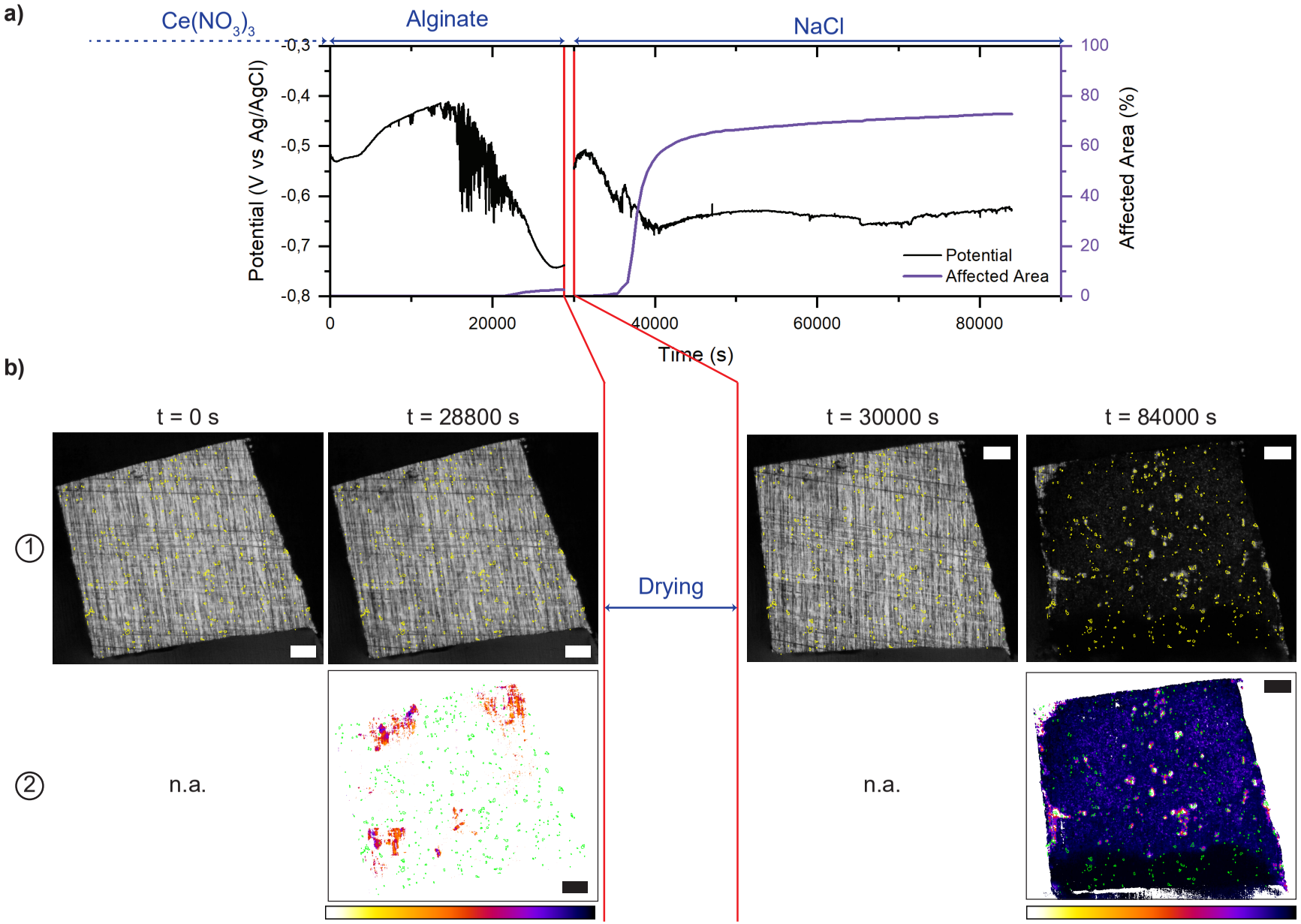

Figure 4.7: a) OCP-AA% plot and b) optical original (row 1) and porcessed (row 2) images collected during 8 h immersion in 0.1 wt% sodium alginate followed by 15 h in 0.05 M NaCl after previous exposure to 1 mM $Ce(NO_3)_3$. The scale bar in all the images represents 50 μm.

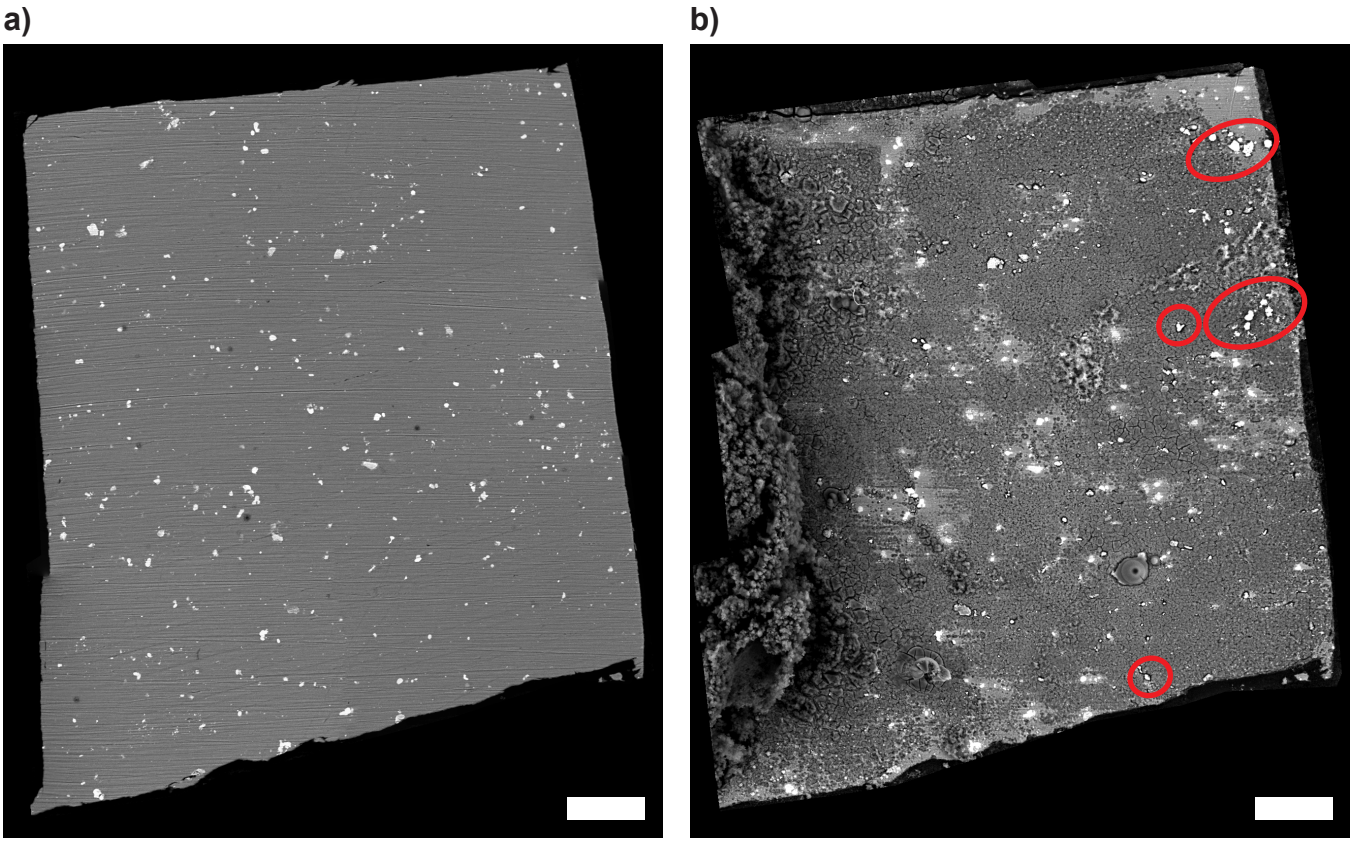

Figure 4.8: SEM-BSE images of the sample exposed to Ce-alginate-NaCl cycle a) before and b) after immersion. The scale bar in both images represents 50 μm.

The results obtained for tests with Ce and PHA are displayed in Figure 4.9. As before, Figure 4.9a shows the OCP-AA% plot for 8 h immersion in PHA (0-28800 s) followed by 15 h immersion in NaCl (30000-84000 s). Figure 4.9b shows the optical original (row 1) and processed (row 2) images acquired at the beginning and end of each immersion step. The drying cycle between the two immersions is represented by the two vertical red bars in Figure 4.9a-b.

The first 8 h of immersion in PHA (Figure 4.9a) show unstable OCP (high amplitude spikes ranging $\approx$ 300-400 mV), but limited optical changes ($<$ 3%). This behaviour is quite similar to the one observed in Figure 4.5b for the same passivator, where the low AA% coupled to an unstable potential were most likely attributed to PHA adsorption-desorption phenomena on/from the surface. Therefore, an interaction with Ce at this stage could not be predicted yet, as these trends were somewhat expected.

Subsequent 15 h immersion in NaCl (30000-84000 s) denote an electrochemical potential (Figure 4.9a) with some isolated and well-defined transients ranging 150-200 mV until $\approx$ 58000 s. These transients are associated to a linear increase in AA% leading almost 40% of the area to be affected. After 58000 s, the potential stabilises at $\approx$ -0.35 V *vs* Ag/AgCl (most likely the corrosion potential E_{corr}) and so does the AA%, which grows further but more slowly, reaching a final value just below 50%. Optical images (Figure 4.9b) at the end of the test show that almost half of the exposed surface has undergone severe degradation. The image analysis at 84000 s provides evidence of more intense optical activity centred on the IMs (purple-blue), while the surrounding Al-matrix is more mildly affected (red-pink), very similar to the localised corrosion events seen in section 2.3. It is important to note, though, that some of the IM particles and certain regions of the surface are still unaffected after 15 h of immersion in NaCl. SEM-BSE *post mortem* analysis was performed also on this micro-electrode and the results are shown in Figure 4.10, where Figure 4.10a and 4.10b were collected before and after immersion, respectively. It is even more blatant from these pictures that part of the IMs show typical features of localised corrosion (trenching around the white Cu-rich IMs), while some others are actually quite intact and unattacked, thus confirming the observation from optical inspection in Figure 4.9b.

Overall, subsequent re-exposure to NaCl gives evidence of typical localised corrosion of AA 2024-T3 (trenching and pitting) from optical, electrochemical and *post mortem* data, thus suggesting loss in protective properties and reversibility of the inhibitors tested. Surprisingly, the IM phase was only partially attacked at the end of the test, perhaps as a consequence of the stabilisation of Ce(III) layers with PHA. It remains unclear why such interaction is more favoured on certain particles than others and, more importantly, making it difficult to totally exclude *a priori* a synergy between Ce(III) and PHA. Nevertheless, the re-appearance of localised corrosion (as in the case of Ce(III) layers instability shown in Figure 3.9a and 3.9b) induces to think that, despite an hypothetical Ce-PHA interaction, stability is not achieved and it might be just a matter of time before all the protection is lost, so that all the IM phase becomes subject to localised attack. This finding is quite important, because it suggests that the typical approach to find a synergistic effect between different inhibitors can sometimes be misleading. Synergy between inhibitors does not necessarily involve the formation of a stable and irreversible system, and simple re-immersion in inhibitor-free solutions (*e.g.* NaCl solution) may already reveal the actual instability of both the inhibitors.

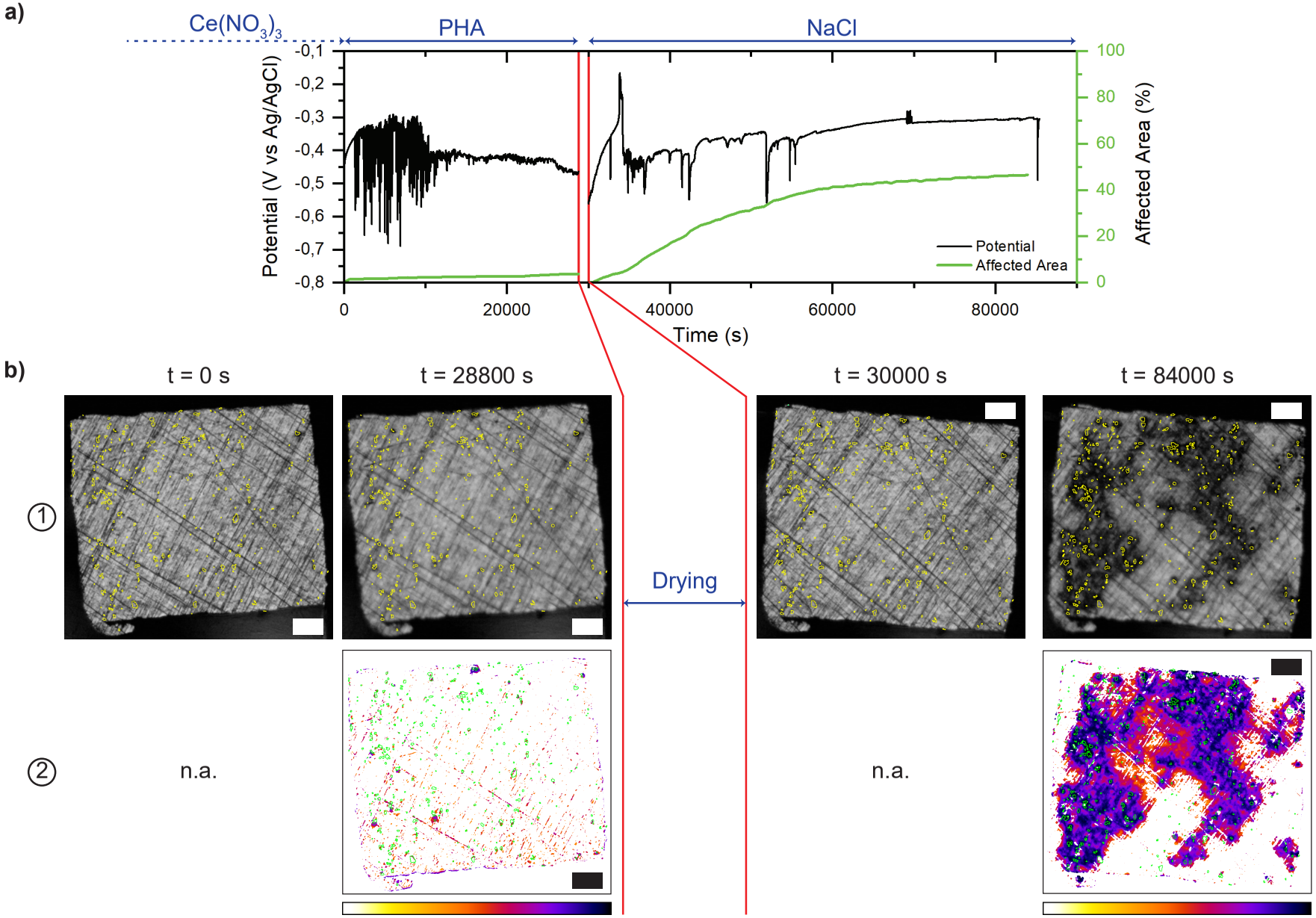

Figure 4.9: a) OCP-AA% plot and b) Optical original (row 1) and porcessed (row 2) images collected during 8 h immersion in 1 mM PHA followed by 15 h in 0.05 M NaCl after previous exposure to 1 mM $Ce(NO_3)_3$. The scale bar in all the images represents 50 μm

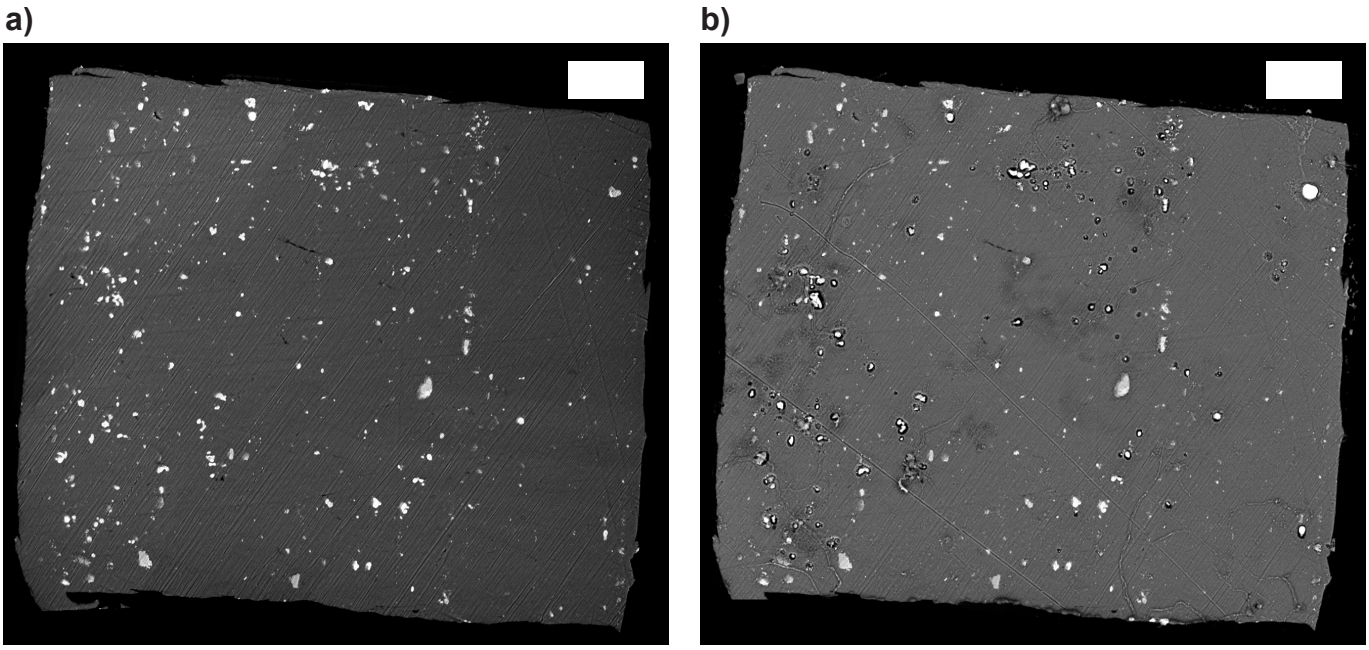

Figure 4.10: SEM-BSE images of the sample exposed to Ce-PHA-NaCl cycle a) before and b) after the full test. The scale bar in both images represents 50 μm.

Although DMTD already showed excellent stability on its own, its performance in combination with Ce inhibitive layers was tested and the results are shown in Figure 4.11. As before, Figure 4.11a shows the OCP-AA% plot for 8 h immersion in PHA (0-28800 s) and 20 h immersion in NaCl (30000-102000 s), while Figure 4.9b shows the respective optical original (row 1) and processed (row 2) images. Drying between the two immersions is represented by the two vertical red bars.

Figure 4.11a shows a negligible amount of optical changes (AA $<$ 0.5%) during the first 8 h of immersion in DMTD accompanied by a stable potential between -0.5 and -0.55 V *vs* Ag/AgCl. A few individual events ($\approx$ 100 mV) are also visible in the OCP signal, but the optical images of Figure 4.11b do not seem to show a correlation between these events and macroscopic surface changes. Stable potential and optical activity suggest that immersion in DMTD creates a stable system, as expected from the results shown in Figure 4.5c.

Re-immersion in NaCl was extended to 20 h, instead of 15 h. The OCP in Figure 4.11a remains stable around -0.55 V *vs* Ag/AgCl throughout the 20 h immersion. The AA% increases slightly from 0% to 0.5% after 40000 s and stabilises into a plateau. At $\approx$ 65000 s AA% increases again more sharply from 0.5% to 3% followed, again, by a flattening into a second plateau around 3.5%, after which it remains stable until the end of the immersion (102000 s). Optical images in Figure 4.11 show limited number of affected locations. In particular, three small and localised spots of high intensity (most likely associated to pits) appear, while lower intensity (yellow-orange) optical changes are spread across the electrode surface.

The increasing AA% trend in "steps" suggests that passivation with DMTD might be achieved by means of a multi-layers adsorption mechanism, so that the plateaus observed in the AA% curve during immersion in NaCl represent the progressive desorption of the topmost layer. Overall, the low amount of degradation at the end of the test (3.5%) matched with a stable OCP signal allows to conclude that the system studied is stable upon re-immersion in NaCl and the appearance of corrosion is significantly delayed in time. However, it is less clear whether the combination of Ce(III) and DMTD actually led to a positive interaction between the two inhibitors, especially if we consider that DMTD alone (*i.e.* without previous exposure to $Ce(NO_3)_3$) showed even lower amount of optical changes after 15 h in NaCl (1% without cerium *vs* 3% with cerium, see Figure 4.5c).

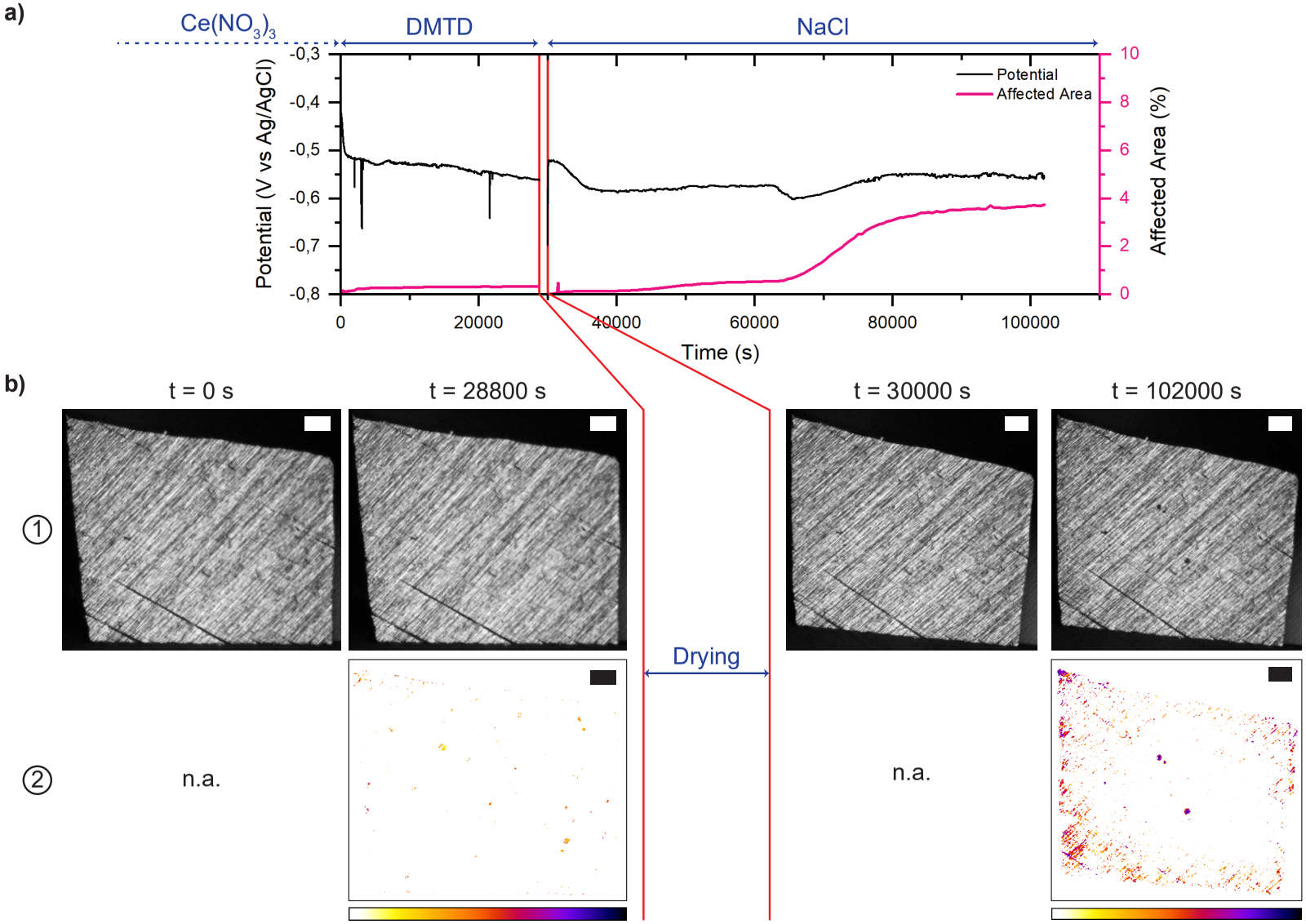

Figure 4.11: a) OCP-AA% plot and b) Optical original (row 1) and porcessed (row 2) images collected during 8 h immersion in 0.1 mM DMTD followed by 20 h in 0.05 M NaCl after previous exposure to 1 mM $Ce(NO_3)_3$. The scale bar in all the images represents 50 μm

In order to better capture the effect of Ce(III)-passivator interaction on the stability of corrosion inhibition properties, Figure 4.12 is proposed, in which the AA% kinetic trends are plotted for immersion in passivator solutions (left column) and subsequent re-immersion in NaCl (right column). Curves displaying the previous exposure to $Ce(NO_3)_3$ are displayed as dashed lines, while solid lines indicate performance of the passivator on its own. The slope relative to 5 h re-immersion in NaCl after exposure to $Ce(NO_3)_3$ (same as the one in Figure 3.9a) is also reported for a better evaluation.

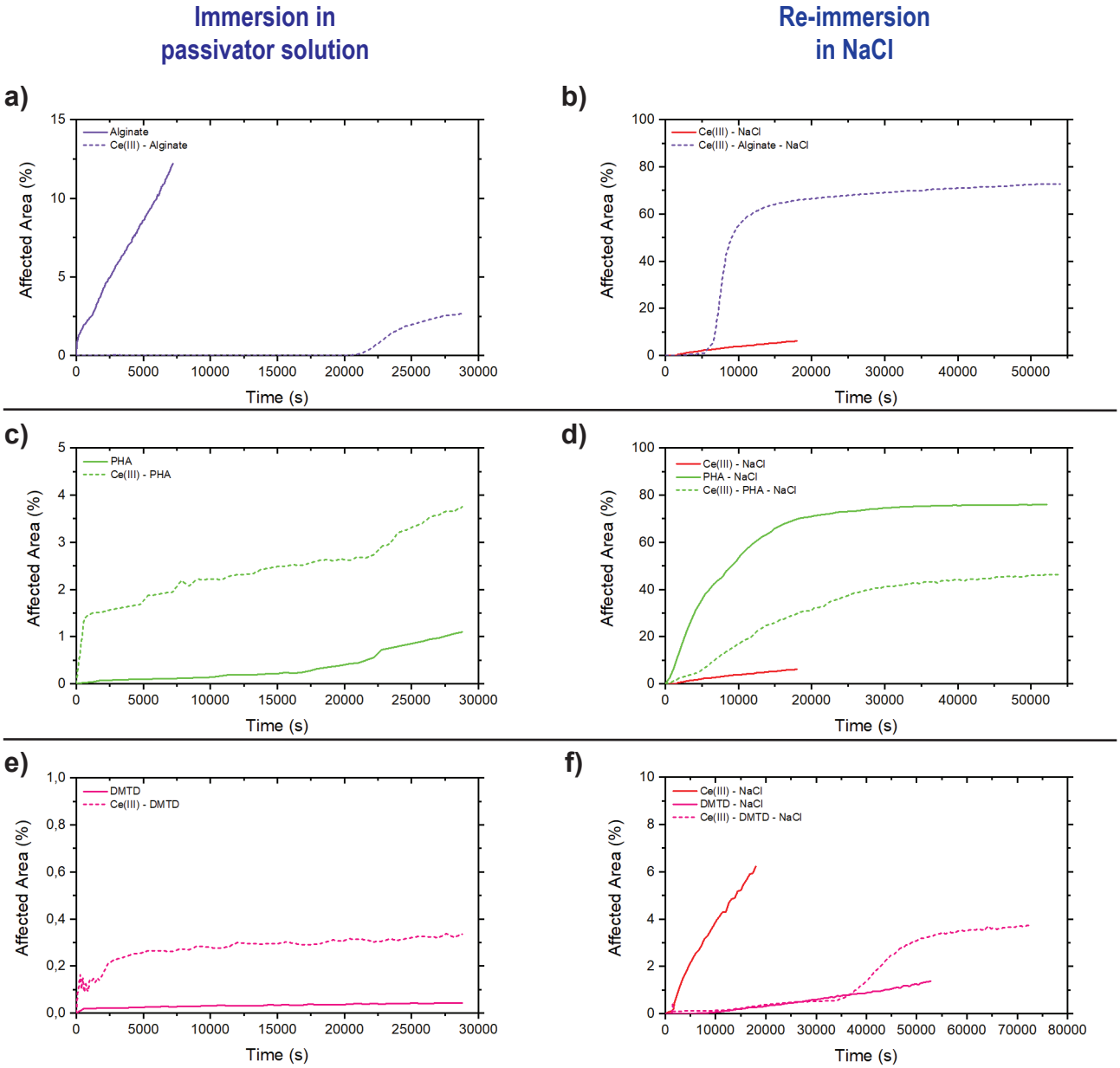

Figure 4.12: Optical data of Affected Area *vs* time for systems studied with a,b) sodium alginate, c,d) PHA and e,f) DMTD. The left column (a, c, e) represents immersion in the passivator solution, while the right column (b,d,f) re-exposure to NaCl.

Alginate is not capable of inhibiting corrosion on its own, but it can passivate Ce(III)-inhibited layers by remarkably suppressing macroscopic optical events during immersion in alginate solution (Figure 4.12a). Further exposure to NaCl shows that treatment with alginate is beneficial in stabilising Ce(III) layers for the fisrt 2 h immersion (Figure 4.12b), after which onset of general corrosion takes place on the Al-matrix.

PHA inhibits corrosion of AA 2024-T3 on its own and also in combination with Ce(III) passivation layers (Figure 4.12c). The higher amount of optical changes in the Ce(III)-PHA system in Figure 4.12c is difficult to interpret and does not exclude an interaction between the two. More interestingly the slopes of the curve in Figure 4.12c are very similar, implying that PHA is providing protection with a similar mechanism in both cases. Re-exposure to NaCl, however, shows poor stability of PHA on its own, even faster than the one of Ce(III) (Figure 4.12d). Combination of Ce(III) with PHA and further re-exposure to NaCl display lower optical rate compared to PHA lone, but still higher than Ce(III) alone (Figure

4.12d), which suggests a possible Ce(III)-PHA synergy lacking in stability.

DMTD shows excellent inhibition of AA 2024-T3 corrosion, both with and without previous exposure to Ce(III) (Figure 4.12e). Re-exposure to NaCl shows again stability in both the DMTD-treated systems (pink slopes belonging to DMTD are lower than the red one belonging to Ce(III) alone, Figure 4.12f). Moreover, both systems with DMTD show onset of the optical activity around the same immersion times (linear increase after 10000 s with a rate equal to $3.8 \cdot 10^{-5}$ %/s). The curve relative to Ce(III)-DMTD passivation, however, shows a more pronounced rate after 36000 s ($1.4 \cdot 10^{-4}$ %/s), which is very similar to the one of Ce(III) alone ($3.7 \cdot 10^{-4}$ %/s), while the sample treated only with DMTD keeps increasing with the same constant rate. This could indicated that Ce might be lost from the Ce(III)-DMTD treated sample and that its stabilisation with DMTD is not completely achieved. If that was the case, it can be concluded that DMTD still provides significant and beneficial delay of the onset of Ce(III)-layers dissolution (30 min for Ce(III)-NaCl *vs* 10 h for Ce(III)-DMTD-NaCl). However, further stabilisation of AA% after 50000 s ($\approx$ 3.5%) is difficult to interpret in case the slope between 36000 s and 50000 s represents the actual loss of cerium. For these reasons, and especially the better stability observed without previous exposure to $Ce(NO_3)_3$, it is concluded that further testing (maybe at longer immersion times) is needed to make stronger conclusions on this system, although DMTD seems to provide the desired stability after re-exposure to inhibitor-free electrolytes.

In conclusion a comparison between all the passivators tested is proposed in Figure 4.13 based on the optical kinetics observed during the NaCl re-immersion step.

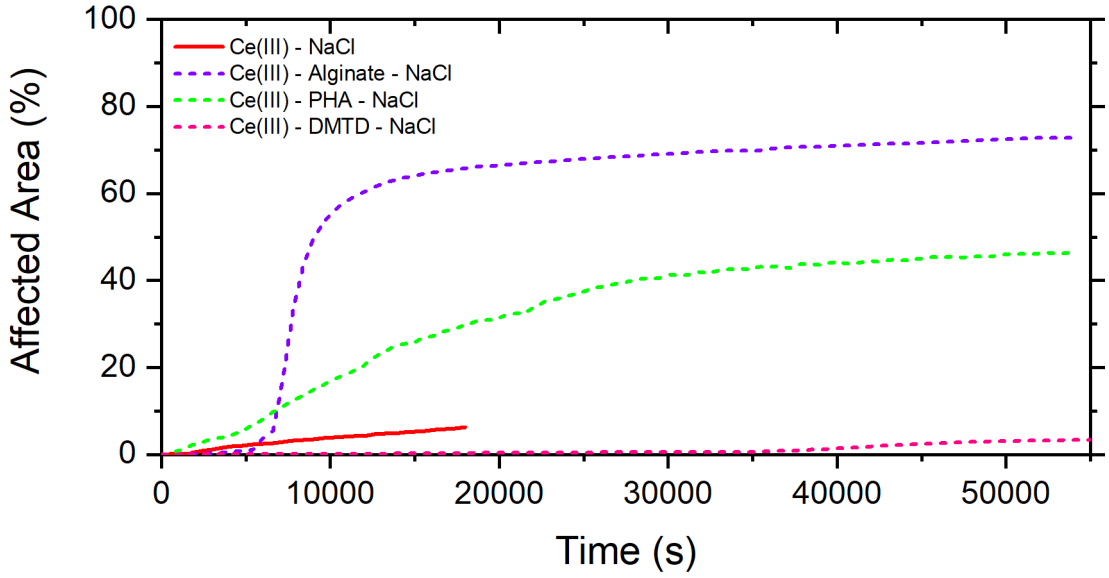

Figure 4.13: Comprehensive comparison of the AA% *vs* time kinetics for different Ce(III)-passivated systems re-immersed in NaCl.

4.4 Final Remarks and Conclusions

The potential of organic compounds to stabilise Ce(III)-inhibitive layers was studied. Three model molecules were chosen due to their potential affinity with Ce-based species, namely alginate (high molecular weight oligomer), phytic acid (organo-phosphate molecular compound) and DMTD (organic corrosion inhibitor). The organic species, named "passivators", were tested in combination with $Ce(NO_3)_3$ according to a protocol of analysis designed to simulate an hypothetical controlled release of the inhibitors from a coating (*i.e.* cerium comes first and the passivator follows) as well as re-immersion conditions with scarce supply of inhibitors. It was concluded that alginate molecules provide passivation and stabilisation of Ce(III) layers deposited on the IM phase. However, it was also revealed that protection of the IM phase alone does not successfully block corrosion events from happening, because blatancy of general corrosion located at the Al-matrix was visible. Phytic acid displayed a rapid but partial establishment of IM-localised corrosion events during re-immersion in NaCl, thereby suggesting incomplete stabilisation of the passivating film. DMTD, on the other hand, showed a significant delay of corrosion and high degree of protection (stability) upon re-immersion in NaCl, but its exceptional performance on its own (*i.e.* not combined with Ce(III) passivation layers) raises doubts about the actual interaction of Ce(III) with DMTD, thus its stabilisation. Further testing is needed to shed some light on this system.

Chapter 5

Conclusions, recommendations and future outlook

The objectives of this research were proposed in section 1.3 and are summarised by the following research question:

Can the protection of Ce(III) inhibitive layers on AA 2024-T3 be improved?

In **Chapter 2** the opto-electrochemical method used in this research was presented together with the protocol of analysis to interpret the results. Validation of this method was provided by an in-depth study of AA 2024-T3 corrosion in 0.05 M NaCl electrolyte. The results showed that high spatio-temporally resolved *in-situ* optics help to identify and reconstruct typical corrosion hierarchy of AA 2024-T3. This process evolves from a local (dealloying, trenching) to a global (pit clustering, corrosion domes, subsurface corrosion) scale. Furthermore, monitoring corrosion in real time allowed us to confirm (for the first time under immersion condition) the existence of a relation between the IM particles composition and their electrochemical activity, thus the time-dependency of their attack, which so far was always indirectly postulated from *post mortem* investigation. The optical-electrochemical *in situ* study proposed here not only led to a validation of the obtained experimental data, but also to a general improved understanding of AA 2024-T3 corrosion. The versatility and potential of this characterisation technique set the basis for further investigation with $Ce(NO_3)_3$ in solution, but, at the same time, opened up promising developments for future (electrochemical) studies on other alloys and/or inhibitors.

Chapter 3 was devoted to studying and understanding corrosion inhibition of AA 2024-T3 with $Ce(NO_3)_3$ by means of real-time opto-electrochemistry and other supporting techniques. The main conclusion from this chapter is that opto-electrochemical characterisation provides useful information about corrosion inhibition of AA 2024-T3 with $Ce(NO_3)_3$ (and Ce(III) salts in general). We were able to identify a certain dependency of the inhibition efficiency on Ce(III) concentration in solution by modelling the system with the Langmuir adsorption theory during the early stages of immersion. We also managed to optically visualize the possible formation of CeO_2 passive deposits on the IMs due to a peroxide-assisted oxidation of Ce(III) into Ce(IV), as well as their thickening in time. In this way, a mechanism of corrosion inhibition provided by Ce(III) salts was proposed based on the (optical and electrochemical) data collected *in situ*, which corroborates some models already proposed in literature and improves the understanding of the inhibition process. Stability of Ce-inhibitive layers to re-immersion in inhibitor-free solutions (NaCl) was also investigated with opto- and localised electrochemistry. It was found out that Ce inhibitive layers are reversible after re-immersion in NaCl, thus ceasing to protect AA 2024-T3. Instability is likely to be ascribed to a progressive re-dissolution of Ce layers, which makes the galvanic effects between IMs and Al-matrix become again influential, eventually leading to appearance of localised corrosion.

Finally, **Chapter 4** was dedicated to the study of Ce(III) inhibitive layers stabilisation with organic compounds (also called "passivators"). Alginate, phytic acid and DMTD were selected based on their potential affinity with Ce-species and assessed both individually and in combination with previously deposited Ce-based passivation layers. Overall, the three passivators showed different performance:

- Alginate was found to stabilise Ce(III) layers deposited on top of the IMs, thus providing long-term protection to this phase. However, onset of generalised corrosion was still observed on the Al-matrix, which led to severe degradation.
- Phytic acid was found to possibly interact with Ce(III)-inhibitive layers, but stabilisation of these was not accomplished - their dissolution was rather accelerated.

- DMTD was found to stabilise the Ce(III)-passivated surface even after re-immersion in sodium chloride solution by significantly decreasing the rate of optical detectable changes, thus delaying the onset of corrosion activity. However, due to its excellent performance even without previous exposure to Ce(III), more research is needed to unveil its mechanism of interaction with Ce(III) layers.

The results obtained from the whole research allow us to conclude that passivation of AA 2024-T3 with Ce(III) salts is an efficient way to inhibit its corrosion as a potential alternative to the highly debated Cr(VI)-based anticorrosion pigments. However, the gradual re-dissolution of the Ce(III) passivation layers when re-exposed to solutions without inhibitors limit their long-term protection, which is an important requirement for the design of anticorrosion primers. To overcome such limitation, the interaction and passivation of Ce(III) with organic compounds was studied as a method to improve the protection provided by Ce(III)-inhibitive layers. From this study, it can be concluded that passivation of Ce(III) layers with organic molecules is (in principle) possible to increase their stability, but some critical points were also inferred for each Ce(III)-passivator system:

- Investigation with sodium alginate showed that passivation of the Ce(III)-protected cathodic IMs was successful, but not enough to prevent corrosion of the Al-matrix (general corrosion). It can be concluded that passivators with multifunctional protection should be looked for, *i.e.* capable of passivating both the Ce(III) inhibitive layers and the Al-matrix. This could be the case of DMTD, which is a mixed (anodic and cathodic) organic inhibitor.

- Studies on passivation with phytic acid revealed that having synergy between inhibitors is not a sufficient condition to obtain irreversible systems. This is an important conclusion, which needs to be better addressed in future studies involving synergistic effects between different inhibitors for corrosion protection.

- Studies with DMTD showed promising potential of this compound to enhance irreversibility of corrosion inhibition layers. We were able to conclude that Ce(III)-DMTD provided higher stability after re-immersion in NaCl than Ce(III) alone due to the remarkable suppression of macroscopic surface events. However, this organic inhibitor also demonstrated to delay corrosion quite well on its own (*i.e.* without previous exposure to cerium), which poses the question whether the presence of Ce(III)-inhibitive films is still necessary (thus somehow undermining the original research question and bringing new value to organic inhibitors).

  From the optical-electrochemical study proposed here and the protocol of immersion chosen, it is difficult to give a complete interpretation of this system and further in-depth research is needed to corroborate these findings. For example, one strategy could be to extend the re-immersion time of the Ce(III)-DMTD and DMTD systems to see how the optical-electrochemical stability evolves in time. Other supporting techniques could also be used to provide quantification of the achieved stability. EIS, for instance, can be performed during the re-immersion in NaCl step to see whether the combination of Ce(III) and DMTD leads to a lower/higher impedance than DMTD alone. Due to the low amount of optical (macroscopic) events, other types of surface analysis could be performed, such as X-ray Photoelectron Spectroscopy (XPS), Auger spectroscpy (AES), Atomic force microscope infrared-spectroscopy (AMF-IR), *etc.*, to better understand the structure of the inhibitive layers formed during this passivation process.

In conclusion, the topic of Ce(III)-inhibitive layers stabilisation with organic molecules tackled in this thesis represents a promising route for future design of complex and Cr(VI)-free anticorrosion coating systems, where a controlled and timely release of multiple inhibitors (or passivators) might be required to successfully protect AA 2024-T3 from the detrimental effects of corrosion.

This research also strengthens the use of *in-situ* optics with high spatio-temporal resolution coupled to electrochemical investigation as a powerful tool to study different electrochemical processes (corrosion, corrosion inhibition, stability, *etc.*), since it provides both qualitative and quantitative parameters to describe the occurring electrochemical events. Real-time optical imaging was demonstrated to be helpful not only to understand the electrochemical signal itself, but also to reconstruct the phenomenology of electrochemical processes under immersion condition. On the other hand, the quantitative data obtained and their time-dependency (*e.g.* the AA%) might help to define the kinetics of the ongoing processes and, consequently, identify further requirements for a purposeful design of coating systems (for example how fast corrosion develops on the alloy, how fast the inhibitor should provide protection, how fast the inhibitor and/or passivator should be released from the coating before Ce(III)-inhibitive layers get dissolved, *etc.*). Such optical-electrochemical *in-situ* technique showed that insights of fundamental character could be gained regarding both the corrosion of AA 2024-T3 and its inhibition with $Ce(NO_3)_3$, but it would be nice to extend the boundaries of its application to other metals or metal-inhibitor systems in order to confirm its robustness in the field of corrosion science.

Appendices

Appendix A

Supporting Information - Chapter 3

A.1 Langmuir adsorption theory as a tool to model the different degrees of Ce(III) protection

To explain the different degrees of inhibition provided by different concentrations of $Ce(NO_3)_3$, considerations about the film-forming nature of Ce(III) inhibitors can be made. Based on the literature studies proposed in section 1.2.3, it is assumed that cathodic precipitation of $Ce(OH)_3$ in alkaline environment is responsible for the inhibition of Ce(III) on AA 2024-T3. For simplicty, the following assumptions can be made:

- Precipitation of one $Ce(OH)_3$ monolayer on top of the active areas (*i.e.* the IMs) is enough to achieve corrosion inhibition.
- Precipitation of $Ce(OH)_3$ on the surface can be assimilated to adsorption phenomena.
- The precipitation kinetics of $Ce(OH)_3$ on the IMs is the same for all concentrations.

Although $Ce(OH)_3$ inhibitive layers might be thicker than a single monolayer, this approximation seems to represent well the system in the very first seconds of immersion, where most of the activity is noticed for the lowest $Ce(NO_3)_3$ concentration tested (*i.e.* 0.01 mM). The assumption about same precipitation kinetics for different concentrations, instead, sounds reasonable since $Ce(OH)_3$ is the precipitating species in all circumstances.

These assumptions allow us to model the system studied with the Langmuir adsoprtion theory. The derivation of the Langmuir adsorption theory and all the equations reported hereafter were taken from [146]. This theory, which is based on kinetic reasoning, entails that the rates of adsorption and desorption of an adsorbate ($Ce(OH)_3$, in this case) on/from a surface (aluminium alloy, in this case) are equal at equilibrium. According to this model, the surface can be characterised by a finite and maximum number of available adsorption sites (φ_{max}), some of them being occupied (φ), some others being vacant ($\varphi_v = \varphi_{max}$ - φ). In the present case, we assume the corrosion sensitive IMs to be the adsorption sites as they need to be protected by the $Ce(OH)_3$ adsorbate. The rate of adsorption (r_{ads}) is limited by the concentration of adsorbate in the solution, as well as by the vacant available sites on the surface according to the following equation:

$$r_{ads} = k_{ads} \cdot \varphi_v \cdot C = k_{ads} \cdot [\varphi_{max} - \varphi] \cdot C, \tag{A.1}$$

where k_{ads} is the adsorption rate constant (s^{-1}) and C is the concentration of Ce^{3+} in solution (taken as dimensionless for simplicity, *e.g.* $m^3 \cdot m^{-3}$). The rate of desorption (r_{des}), on the other hand, is proportional to the number of already occupied sites according to the following:

$$r_{des} = k_{des} \cdot \varphi, \tag{A.2}$$

with k_{des} being the desorption rate constant (s^{-1}). At equilibrium, equation (A.1) = equation (A.2), so that the following equation can eventually be written:

$$\varphi = \frac{\varphi_{max} \cdot C}{k + C}, \tag{A.3}$$

with $k = k_{des}/k_{ads}$. This equilibrium equation in (A.3), considered for adsorption-desorption events happening at a constant temperature, represents the Langmuir's adsorption isotherm. The shape of a typical isotherm is represented in Figure A.1 (red curve). Two "extreme" scenarios can now be considered:

1. $C >> k$, so that $C+k \approx C$ and

2. C << k, so that C+k ≈ k.

In case 1, equation (A.3) becomes:

$$\varphi = \varphi_{max}, \tag{A.4}$$

whereas in case 2, equation (A.3) becomes:

$$\varphi = \frac{\varphi_{max} \cdot C}{k}. \tag{A.5}$$

By applying the third assumption made in the beginning, *i.e.* the rate of precipitation does not depend on C, k becomes a constant. This implies that:

1. For sufficiently high concentration of Ce(III) in solution (case 1), saturation of all the available sites with a monolayer of $Ce(OH)_3$ is favoured due to a high supply of Ce^{3+} ions, as represented by equation (A.4).
2. For low concentration of Ce(III) (case 2), the supply of Ce^{3+} ions is not high enough to reach a fast and immediate saturation of all the adsorption sites, so that the number of occupied $\varphi < \varphi_{max}$, as of equation (A.5), because the C/k ratio (with C<<k) becomes small (*i.e.* < 1).

If fast saturation of all the active sites due to the sufficiently high Ce^{3+} concentration occurs (case 1), an homogeneous $Ce(OH)_3$ monolayer is formed on top of all the adsorption sites, thus providing protection to the IMs. Conversely, if saturation of all the active sites lacks to occur (case 2), a non-homogenous $Ce(OH)_3$ monolayer forms on the adsorption sites, thus providing only partial protection. Therefore, the uncovered and unprotected active sites may favour the onset of corrosion, as well as the propagation into corrosion pits.

It is clear that the situation described in case 2, may well represent the case of [Ce(III)] = 0.01 mM, where nucleation and growth of pits limited to a few IMs was observed during the first 10000 s of immersion (Figure 3.5). Case 1, on the other hand, represents well higher concentrations of Ce(III), *i.e.* 0.1 and 1 mM, where activity is suppressed from the beginning (AA% = 0%, see Figure 3.3) as a consequence of a fast saturation and protection of the active sites.

For Ce(III) at 0.01 mM, a simple quantification of the φ at this concentration was calculated. The total number of IMs counted on the exposed surface was equal to 344. After 10000 s of immersion, the optically affected IMs were 24, meaning that 24 IM locations are likely to have grown into pits. This means that of the total 344 active sites (φ_{max}), $Ce(OH)_3$ can provide protection to only 320 of them (φ), thus leaving 7% of the IM phase at the mercy of corrosion attack. The situation just described is schematically summarised in Figure A.1, where the Langmuir Isotherm (φ *vs* C) is plotted and the three concentrations tested are highlighted.

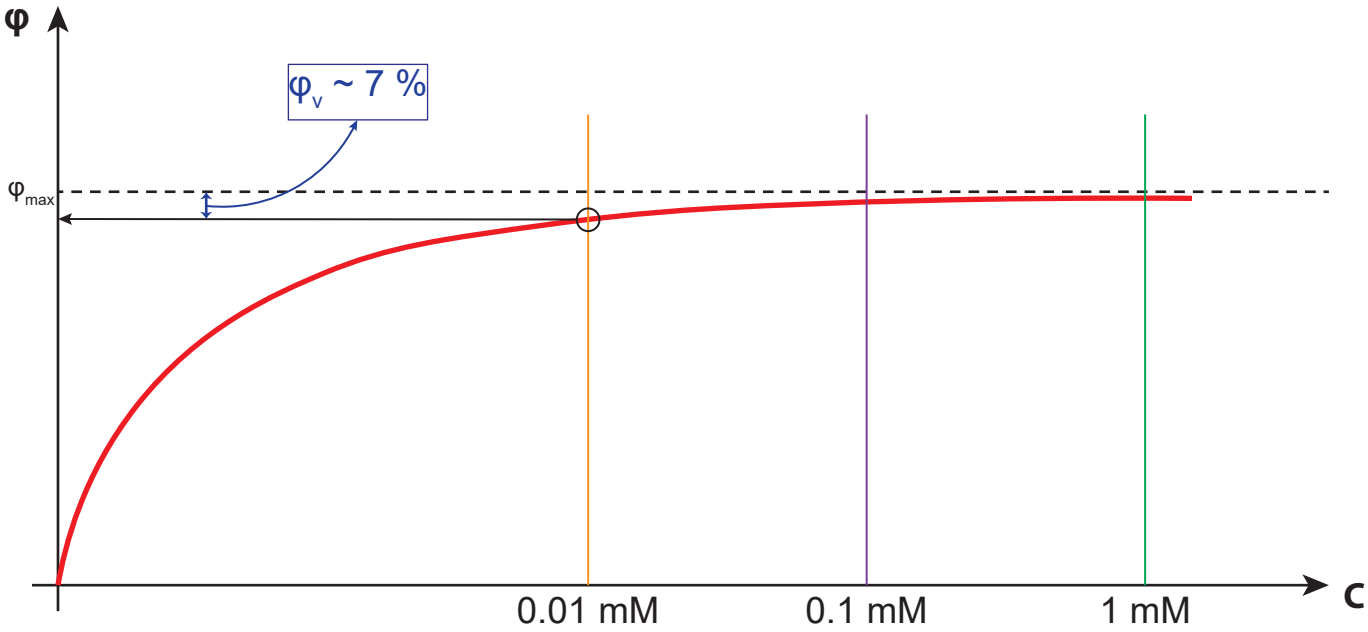

Figure A.1: Representation of a Langmuir adsorption isotherm and its relation with the different Ce(III) concentrations tested, namely 0.01 mM (orange), 0.1 mM (purple) and 1 mM (green).

A.2 SEM-BSE *post mortem* analysis after 15 h in Ce(III)

SEM-BSE images were collected before an after 15 h of immersion in 1 mM $Ce(NO_3)_3$ and they are shown in Figure A.2. The images do not provide any sign of corrosion attack, thus confirming corrosion inhibition provided by Ce(III) throughout the test time.

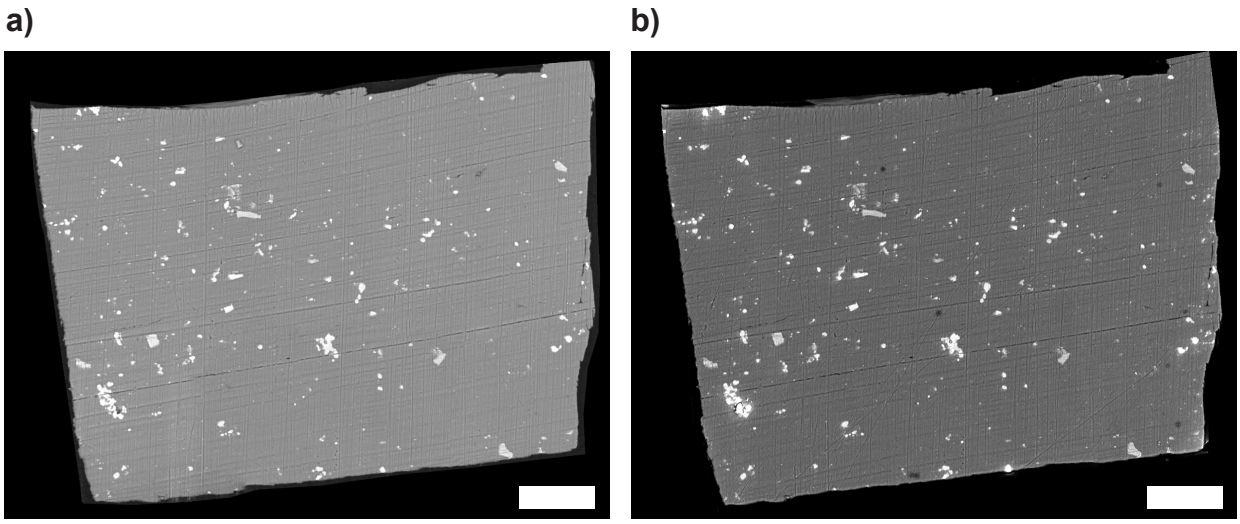

Figure A.2: SEM-BSE images a) before and b) after immersion in 1 mM $Ce(NO_3)_3$ for 15 h. The scale bar in both picture represents 50 μm

A.3 Electrochemical impedance spectroscopy on corroding and Ce(III)-inhibited AA 2024-T3

The results of EIS are displayed in Figure A.3, in the form of Bode (Figure A.3a), Phase Shift (Figure A.3b) and Nyquist plots (Figure A.3c). For the inhibited sample, three curves are displayed at 1 h, 7 h and 15 h immersion, representing the beginning, middle and end of the immersion time. As for the corroding sample, the curves relative to 1 h and 3 h of immersion are displayed as a reference. The impedance values have also been normalized to the exposed surface area.

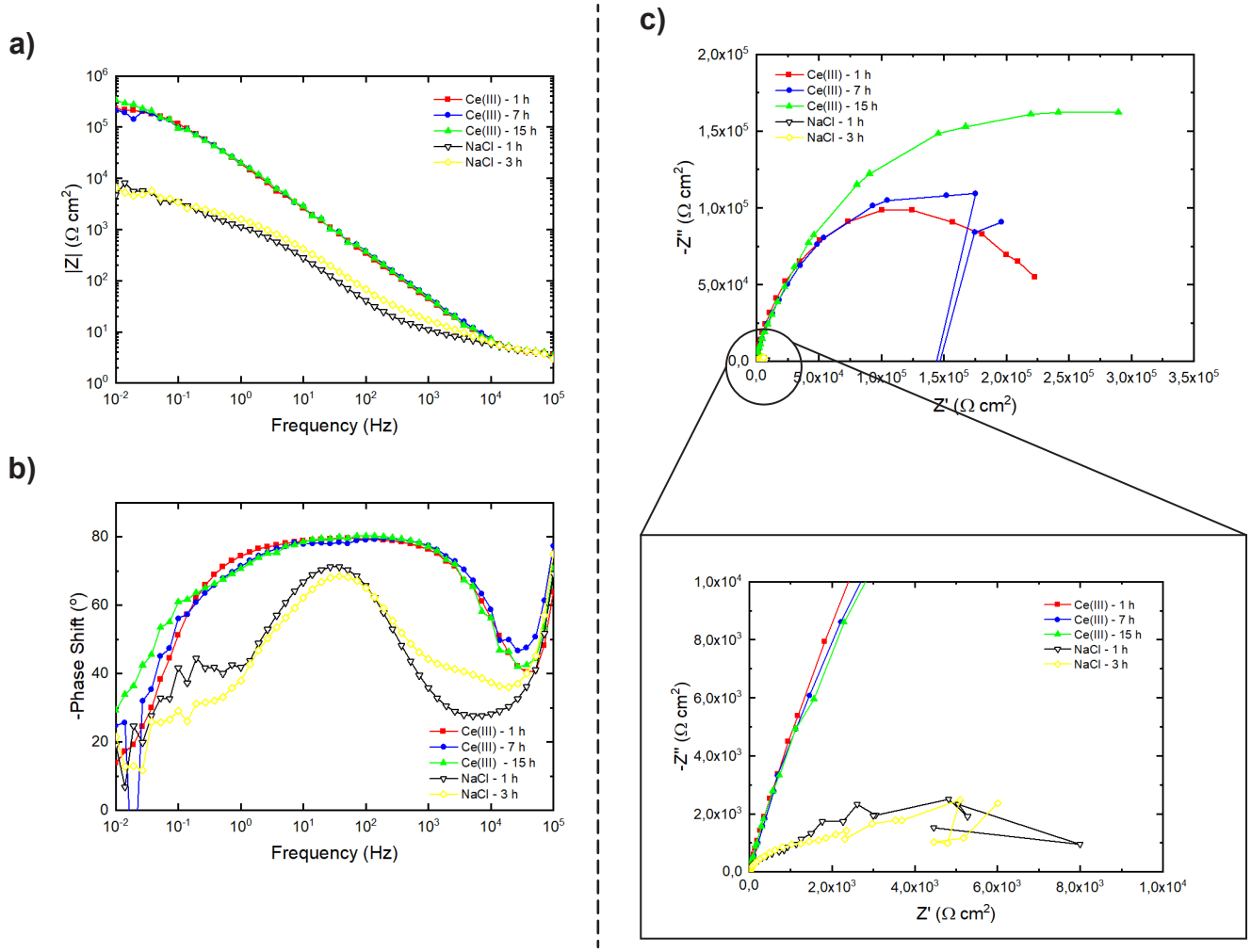

Figure A.3: a) Bode, b) Phase Shift and c) Nyquist plots for immersion in NaCl solutions (1 h and 3 h) and immersion in 1 mM Ce(III) solutions (1 h, 7 h and 15 h).

The Bode Plot in Figure A.3a shows that the sample immersed in Ce(III) solution for 1 h presents higher total impedance ($2 \cdot 10^{-5}$ Ω cm^2) in the low frequency domain (*i.e.* 10^{-2} Hz) than the sample immersed in NaCl solution at the same time ($4 \cdot 10^{-3}$ Ω cm^2). Such difference is of almost two orders of magnitude. Furthermore, the Bode (Figure A.3a) and phase shift (Figure A.3b) curves relative to 1 h immersion in NaCl solution seem to display two time constants, one a bit less defined around 10^{-2} Hz, while the other between 10^{1}-10^{2} Hz. These time constants were also reported elsewhere [147, 148] and attributed to the electron charge transfer across the electrical double layer and to the native oxide layer, respectively. For the same immersion time, the phase shift plot (Figure A.3b) suggests that the addition of Ce(III) to the solution causes the low frequency time constant to disappear, while the other one is broadened to a wider range of frequencies ($\approx 10^{-1}$-10^{4} Hz), as confirmed by the wide plateau of phase angle at 80°. This broadening of the second time constant translates into a long straight line between the 10^{-1}-10^{4} Hz in Bode plot (Figure A.3a). A very similar behaviour was also reported in other EIS studies using Ce(III) compounds [94, 149, 150]. The Nyquist plots after 1 h immersion,

shown in Figure A.3c, highlight even further the difference between a sample immersed in NaCl and one immersed in Ce(III), because the size of the capacitive loops differ significantly in order of magnitudes ($\approx$ two orders of magnitude).

The total impedance ($|Z|$) at low frequency in the Bode plot of Figure A.3a is a direct measure of the protection against corrosion. The difference in two orders of magnitude of $|Z|$ between a sample immersed in NaCl and Ce(III) clearly highlights the inhibitive properties given by small additions of Ce(III). This difference is also quite clear from the Nyquist plot in Figure A.3c, so that it makes it easier to conclude that Ce(III) is indeed protecting the metal alloy and inhibiting corrosion. The disappearance of the time constant associated to the charge transfer across the electrical double layer and the simultaneous broadening of the one related to the native oxide layer suggest that the addition of Ce(III) to the electrolyte:

- slows down the electron transfer kinetics across the double layer (hence the corrosion rate);
- inhibits corrosion by forming a passivation layer with capacitive behaviour.

Ascertained that clear difference can be seen in EIS plots with and without the addition of Ce(III) in the solution, it is more interesting to see how these plots develop with time. For the corroding sample in NaCl solution, not many differences can be seen between the curves at 1 h and 3 h of immersion in Bode (Figure A.3a), phase shift (Figure A.3b) and Nyquist plots (Figure A.3c), meaning that these trends are quite representative of the ongiong corrosion process of the substrate. For this reason, the measurement was stopped after 3 h of immersion. As for the Ce-inhibited sample, new time constants were not noticeable after 7 and 15 h (Figure A.3a and Figure A.3b). A mild increase of the low frequency impedance with immersion time can be witnessed, but ovrall remaining at the same order of magnitude as of 1 h (*i.e.* $\approx 10^5\ \Omega\ \text{cm}^2$). The increase in total impedance, translates into a growth of the phase shift angle at the same frequency (from 15°to 30°), which highlights and increase in the capacitive properties of the inhibitive passivation layer with time. Such increase is even clearer from the Nyquist plot in Figure A.3c, where the capacitive arcs become progressively bigger in size from 1 to 15 h of immersion. The increase of capacitive behaviour in time can be explained with a progressive thickening in time of the formed capacitive and protective layer. However, conversion into an insulating Ce(IV) oxide phase can also be a plausible option due to the reduced the permittivity of the formed phase.

A.4 Opto-electrochemical analysis with H_2O_2 solution

The test protocol of such test was described above (Figure 3.1b). It is important to remind that the replacement of the electrolyte did not involve neither removal and drying of the sample form the cell nor washing of the cell itself. The new electrolyte was simply flushed while the potentiostat was still measuring potential fluctuations, in order not to have discontinuity in the signal.

Optical and electrochemical data relative to the first 2 h immersion in 1 mM $Ce(NO_3)_3$ (*i.e.* before flushing of H_2O_2 in the cell) are reported in Figure A.4. As expected, the potential is stable and the optical changes very limited, in agreement with the observations already extracted from Figure 3.6 for the same immersion time.

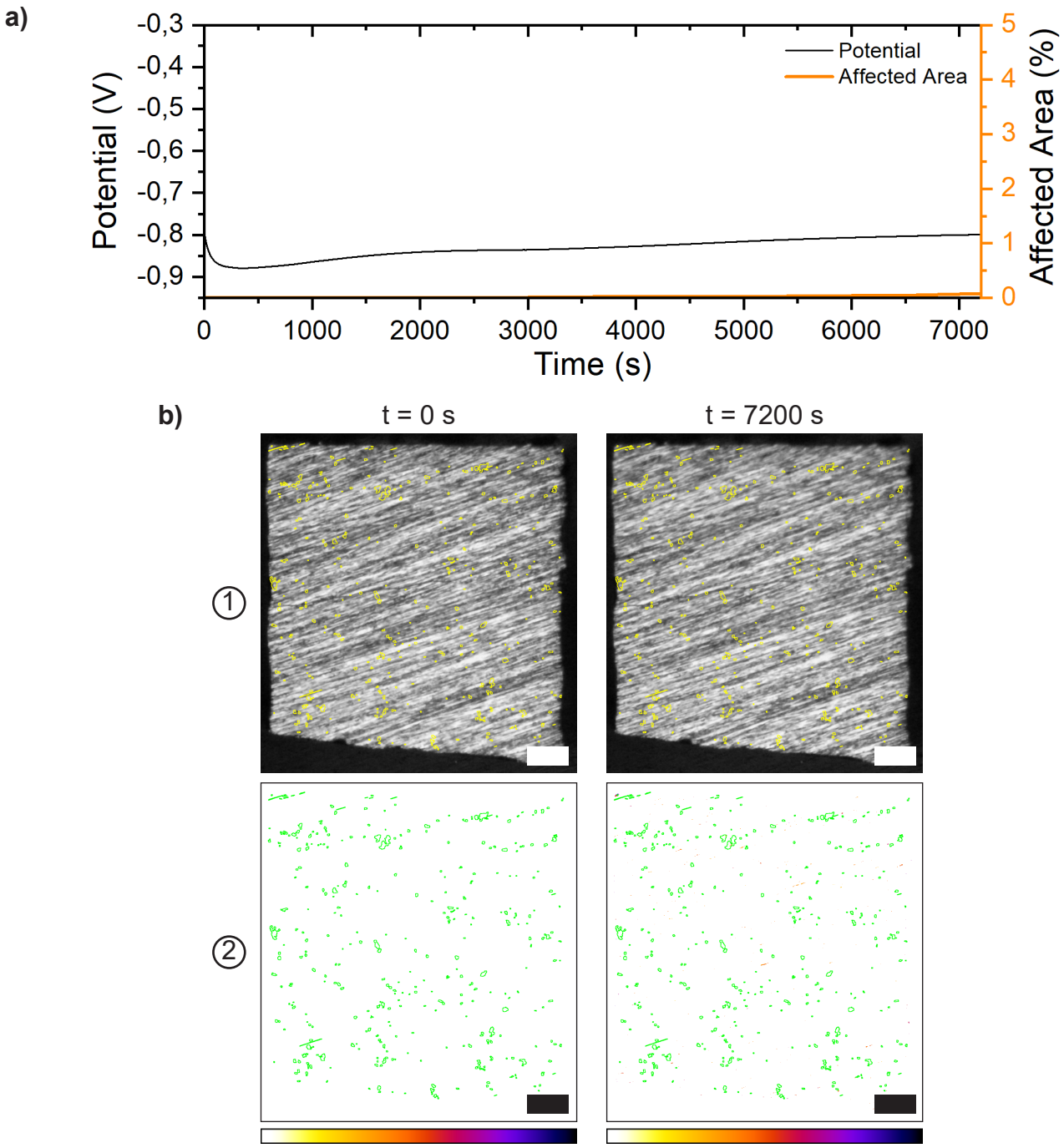

Figure A.4: a) OCP-AA% plot and b) optical original (row 1) and processed (row 2) images relative to the first 2 h of immersion in $Ce(NO_3)_3$ 1 mM before the addition of H_2O_2 electrolyte. The scale bar in the images represents 50 μm.

The results obtained after the addition of H_2O_2 are shown in Figure A.5, in which Figure A.5a reports the OCP and AA% trends, while Figure A.5b reports the optical (original and processed) images. Data of immersion in H_2O_2 after 7800 s were

not analysed because significant production of gas bubbles (probably H_2 evolution) was observed, which compromised the optical data. After 7200 s the Faraday cage was opened, which caused some disturbance to the electrochemical potential signal in the form of small perturbations $<$ 50 mV (see arrow in Figure A.5a). Soon after the Faraday cage was opened, H_2O_2 electrolyte was flushed inside the electrolytic cell, which caused the potential to increase firmly from -0.8 V *vs* Ag/AgCl to -0.4 V *vs* Ag/AgCl as indicated by the arrow in Figure A.5a. Once the electrolytic cell was filled with H_2O_2, the Faraday cage was closed again so that the actual optical-electrochemical measurement could start. The start time of the test is shown in Figure A.5 as a red vertical bar labelled as t_{start}. After t_{start}, the potential keeps increasing in a stable manner towards -0.35 V *vs* Ag/AgCl until it becomes unstable at 7400 s and transients of large amplitude (100 mV) appear. The amplitude and density of transients seems to decrease with time in a similar way as the one observed in Figure 2.14a. The AA% curve in Figure A.5a, on the other hand, is characterised by a limited growth between t_{start} and 7600 s (1%), followed by a more pronounced (exponential) growth between 7600 s and 7800 s (from 1% to 8%). The optical images of Figure A.5b show the exposed surface at two different immersion times, namely t_{start} and 7600 s, which is the time before the onset of H_2 evolution. The original images (row 1) do not show significant changes occurring between t_{start} and 7600 s, but the processed image (row 2) display some low intensity changes (red in the colour intensity bar) to be localised on (a few) IM particles.

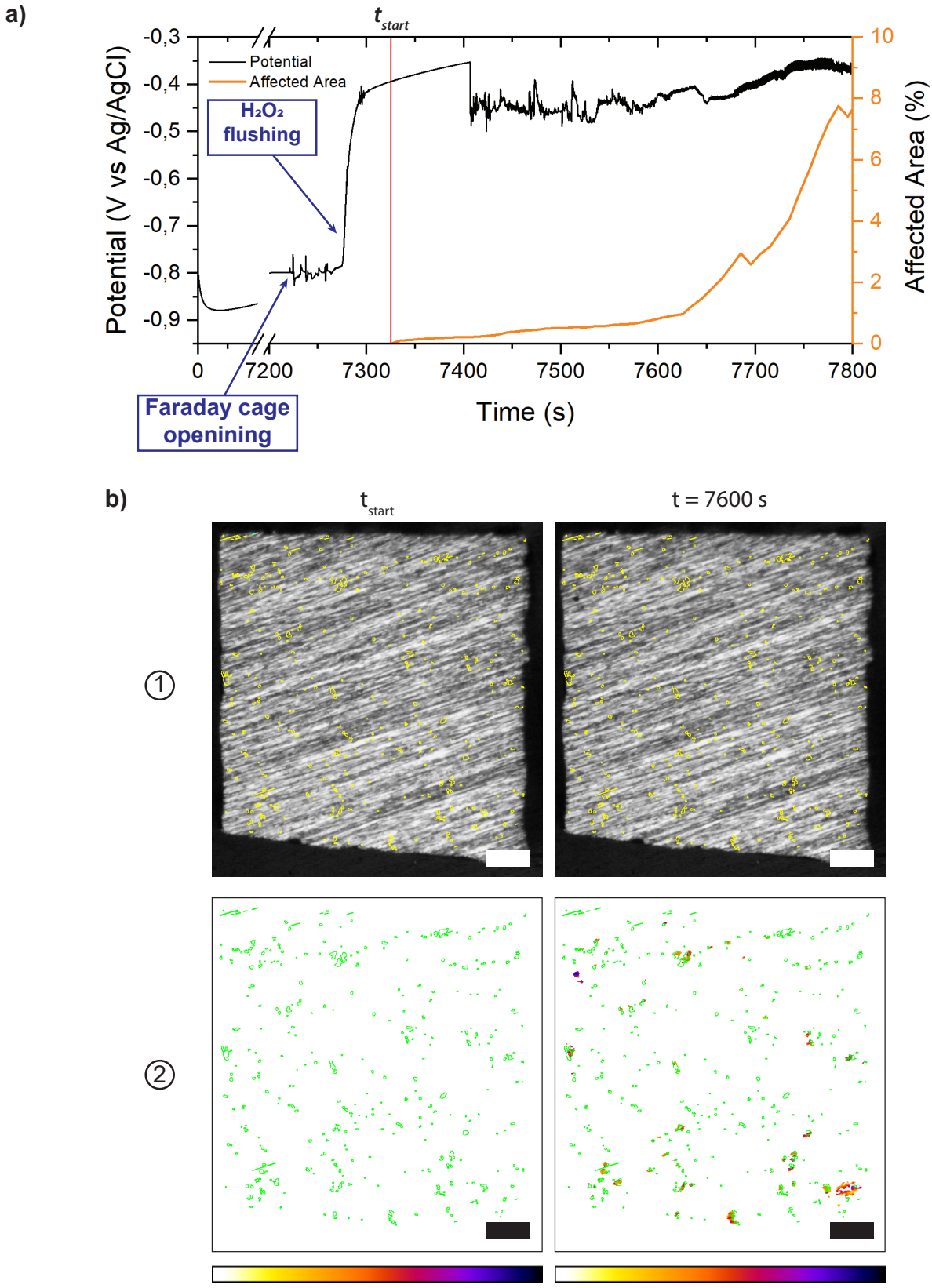

Figure A.5: a) OCP and AA% plots *vs* time for immersion in H_2O_2 electrolyte after exposure to Ce(III) (7200-7800 s). b) Optical original (row 1) and processed (row 2) images relative to immersion in H_2O_2 electrolyte at t_{start} and 7600 s. The scale bar in the pictures represent 50 μm.

Since the optical analysis was compromised by gas evolution, SEM-BSE *post mortem* analysis was performed after 30 minutes of immersion in H_2O_2 solution (Figure A.5b shows images until 13 min immersion in H_2O_2). Figure A.6 reports the result of this analysis, in particular Figure A.6a shows the micro-electrode surface before immersion, while Figure A.6b

shows the same surface after immersion for comparison. It can be observed from Figure A.6b that the sample shows some clear surface features after the test: build-up of corrosion products (green arrows), cracks (red arrows), and corrosion rings as big as 50-60 μm around single or multiple IM particles (yellow circles). Despite these signs, the IM particles seem to be overall unaffected. The blue circles in Figure A.6b, in particular, highlight some of the IM particles that seemed to be optically affected at 7600 s (Figure A.5b), but they actually look unattacked and well protected even after exposure to H_2O_2. EDS and Raman spectroscopies were also performed on these samples to see if detection of cerium could be achieved, but these measurements were unsuccessful.

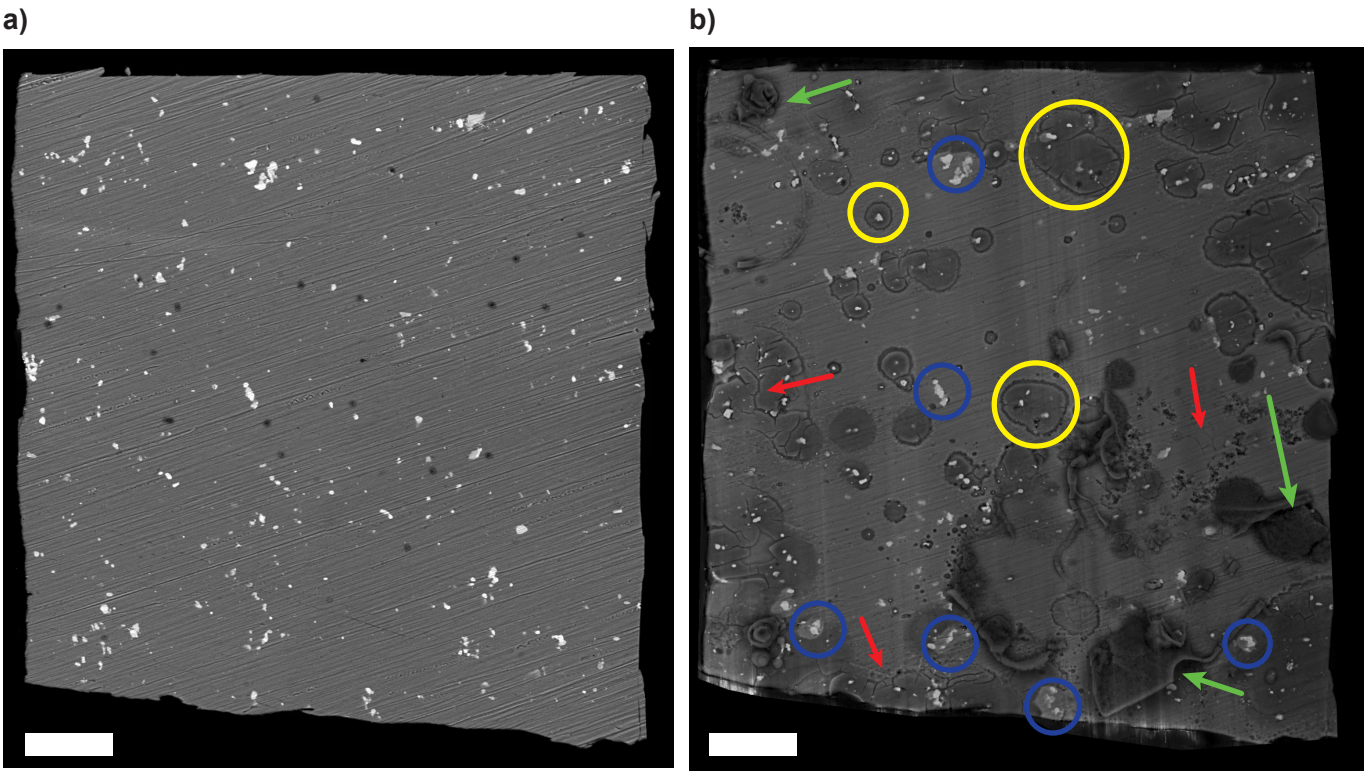

Figure A.6: a) SEM-BSE image of the working electrode used for H_2O_2 test before immersion in Ce(III) electrolyte. b) SEM-BSE *post mortem* image of the working electrode used for H_2O_2 test after exposure to Ce(III) and H_2O_2 electrolytes. The scale bars in both pictures represent 50 μm.

The results from immersion in H_2O_2 showed that corrosion took place on the analysed sample. In particular, the transient in the OCP signal after 7400 s and its noisy character up to 7800 s suggest a similar corrosion process as the one observed in section 2.3. Onset of optical (and possibly electrochemical) activity localised on the IMs is also observed in the first 7600 s. Nonetheless, SEM-BSE *post mortem* analysis reveals that the degradation caused by corrosion is mainly located at the Al-matrix, thus leaving the IM phase overall unaffected and protected. The lack of corrosive attack on the IM phase is atypical for this alloy, whose corrosion evolution was demonstrated in section 2.3 to be initially localised on the IMs and spread to a global scale due to the co-operation of the different IMs. Therefore, if the IM phase is optically affected from t_{start} till 7600 s, but the *post mortem* analysis reveals no signs of attack (*e.g.* dealloying, trenching, *etc.*), it can be concluded that the optical changes caused by the addition of H_2O_2 at 7600 s cannot be due to localised corrosion.

On balance, the results seem to suggest that the optical changes at 7600 s, which are qualitatively similar to the ones observed in Figure 3.6b after 11000 s, can be ascribed to the selective deposition of Ce-inhibitive layers on the IM particles. In particular, the accelerated detection of these optical changes after the addition of H_2O_2 ($\approx$ 5 minutes after H_2O_2 flushing) together with the prompt increase in potential to more noble values ($\approx$ 400 mV), suggests that formation of a passive Ce(IV)-oxide layer (CeO_2) occurs on the IMs, as a consequence of the promoted oxidation from Ce(III) to Ce(IV) species.

It is difficult to say whether the optical signal observed on the IMs is caused by a progressive thickening effect of the deposits or just due to the oxidation itself as a change in refractive index. It is reasonable to assume that both these processes are actually occurring simultaneously, so that a progressive build-up of a passive oxide phase on top of the IMs leads to an increased protection. This explanation might justify the increase in protective properties observed in section A.3. On the other hand, the lack of Ce detection with EDS and Raman spectroscopy underline the substantial thinness of

these protective layers, which raises questions about the optical detection limit due to thickening.

With these conclusions, the opto-electrochemical test with hydrogen peroxide confirms itself as a powerful tool to corroborate the active role of H_2O_2 during the inhibition mechanism provided by $Ce(NO_3)_3$ (and Ce(III) inhibitors in general) through the two-electron pathway, as it was discussed in section 1.2.3. Thus, we confirm that oxidation of Ce(III) to Ce(IV) and CeO_2 formation is possible due to peroxide oxidation, and that the surface changes obsered in Figure 3.6 after 11000 s can be related to passive layer thickening or conversion to more stable CeO_2.

A.5 Instability of Ce layers studied with Scanning Kelvin Probe Force Microscopy

The Volta potential map and profiles measured with SKPFM after 20 minutes of immersion in 1 mM $Ce(NO_3)_3$ are reported in Figure A.7.

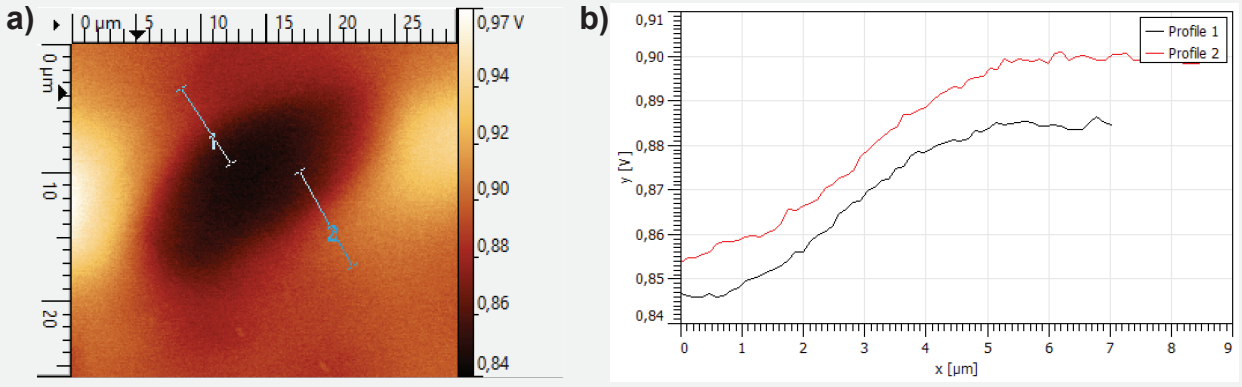

Figure A.7: Volta potential a) map and b) profiles on an IM particle after 20 minutes of immersion in 1 mM $Ce(NO_3)_3$.

Figure A.8 displays the optical image taken after 5 h of re-immersion in NaCl. The high level of degradation (pits) spread across the surface impeded the measurement of the Volta potential at this immersion step.

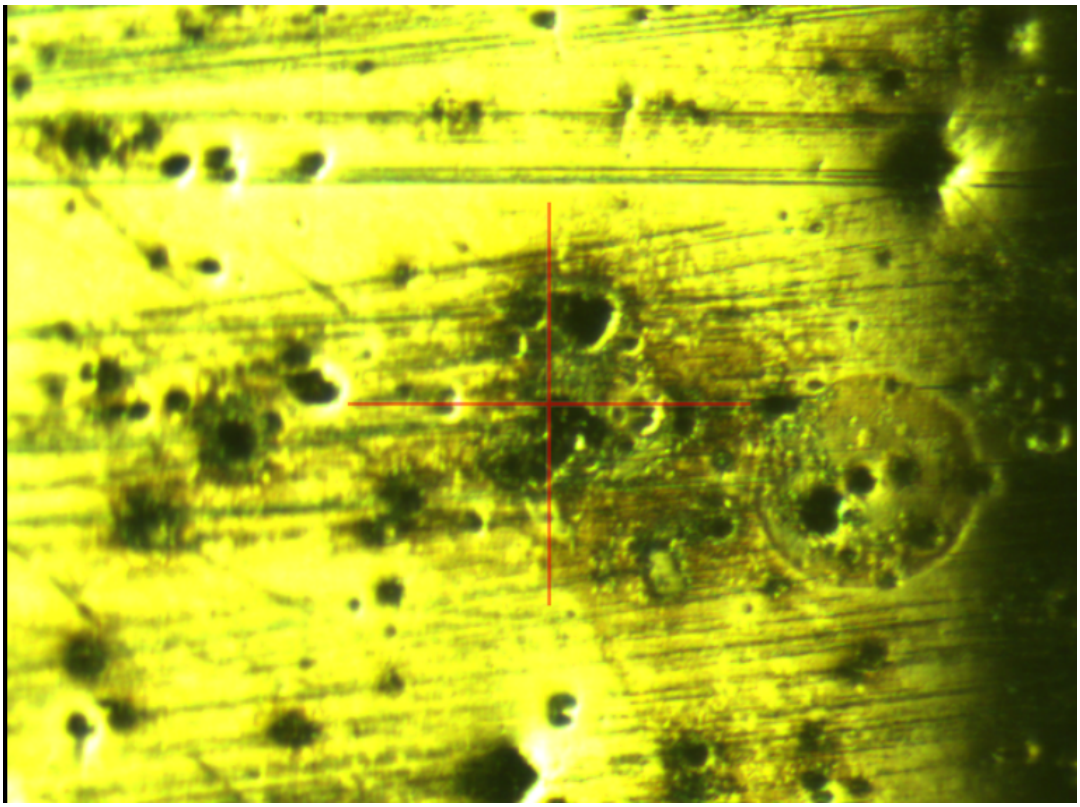

Figure A.8: Optical microscopy image showing the high density of pits after 5 h of re-immersion in NaCl

Appendix B

Supporting Information - Chapter 4

B.1 SEM-BSE *post mortem* analysis after 2 h immersion in alginate

SEM-BSE images were collected before an after 2 h of immersion in 0.1 wt% alginate and they are shown in Figure B.1. The image after 2 h of immersion shows clear signs of corrosive attack like trenches around IMs and build-up of corrosion products.

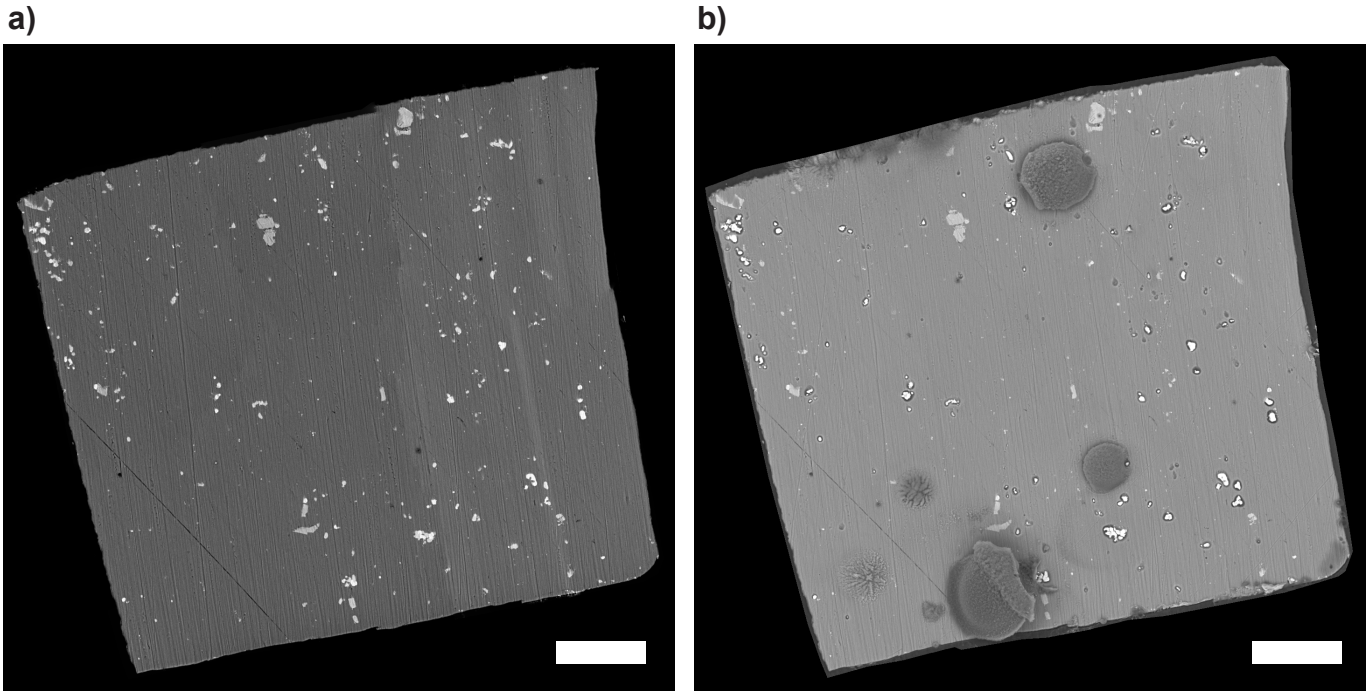

Figure B.1: SEM-BSE images a) before and b) after immersion in 0.1 wt% alginate for 2 h.

Bibliography

[1] A. P. Mouritz, "Aluminium alloys for aircraft structures," in *Introduction to Aerospace Materials*, pp. 173–201, Elsevier, 2012.

[2] A. E. Hughes, R. Parvizi, and M. Forsyth, "Microstructure and corrosion of AA2024," *Corrosion Reviews*, vol. 33, pp. 1–30, Jan. 2015.

[3] A. E. Hughes, N. Birbilis, J. M. Mol, S. J. Garcia, X. Zhou, and G. E. Thompson, "High Strength Al-alloys: Microstructure, Corrosion and Principles of Protection," in *Recent Trends in Processing and Degradation of Aluminium Alloys*, InTech, Nov. 2011.

[4] G. Gottstein, *Physical Foundations of Materials Science*. Springer Berlin Heidelberg, 2004.

[5] A. P. Mouritz, "Strengthening of metal alloys," in *Introduction to Aerospace Materials*, pp. 57–90, Elsevier, 2012.

[6] E. McCafferty, "Getting started on the basics," in *Introduction to Corrosion Science*, pp. 13–31, Springer New York, Nov. 2009.

[7] F. Queiroz, M. Magnani, I. Costa, and H. de Melo, "Investigation of the corrosion behaviour of AA 2024-T3 in low concentrated chloride media," *Corrosion Science*, vol. 50, pp. 2646–2657, Sept. 2008.

[8] R. G. Buchheit, "A compilation of corrosion potentials reported for intermetallic phases in aluminum alloys," *Journal of The Electrochemical Society*, vol. 142, no. 11, p. 3994, 1995.

[9] A. Boag, A. Hughes, A. Glenn, T. Muster, and D. McCulloch, "Corrosion of AA2024-T3 part I: Localised corrosion of isolated IM particles," *Corrosion Science*, vol. 53, pp. 17–26, Jan. 2011.

[10] A. Hughes, A. Boag, A. Glenn, D. McCulloch, T. Muster, C. Ryan, C. Luo, X. Zhou, and G. Thompson, "Corrosion of AA2024-T3 part II: Co-operative corrosion," *Corrosion Science*, vol. 53, pp. 27–39, Jan. 2011.

[11] A. Glenn, T. Muster, C. Luo, X. Zhou, G. Thompson, A. Boag, and A. Hughes, "Corrosion of AA2024-T3 part III: Propagation," *Corrosion Science*, vol. 53, pp. 40–50, Jan. 2011.

[12] N. Birbilis and R. G. Buchheit, "Investigation and discussion of characteristics for intermetallic phases common to aluminum alloys as a function of solution pH," *Journal of The Electrochemical Society*, vol. 155, no. 3, p. C117, 2008.

[13] G. O. Ilevbare, O. Schneider, R. G. Kelly, and J. R. Scully, "In situ confocal laser scanning microscopy of AA 2024-T3 corrosion metrology," *Journal of The Electrochemical Society*, vol. 151, no. 8, p. B453, 2004.

[14] A. E. Hughes, A. M. Glenn, N. Wilson, A. Moffatt, A. J. Morton, and R. G. Buchheit, "A consistent description of intermetallic particle composition: An analysis of ten batches of AA2024-T3," *Surface and Interface Analysis*, vol. 45, pp. 1558–1563, Jan. 2013.

[15] L. Lacroix, L. Ressier, C. Blanc, and G. Mankowski, "Combination of AFM, SKPFM, and SIMS to study the corrosion behavior of S-phase particles in AA2024-T351," *Journal of The Electrochemical Society*, vol. 155, no. 4, p. C131, 2008.

[16] L. Lacroix, L. Ressier, C. Blanc, and G. Mankowski, "Statistical study of the corrosion behavior of Al_2CuMg intermetallics in AA2024-T351 by SKPFM," *Journal of The Electrochemical Society*, vol. 155, no. 1, p. C8, 2008.

[17] R. G. Buchheit, "Local dissolution phenomena associated with S phase (Al_2CuMg) particles in aluminum alloy 2024-T3," *Journal of The Electrochemical Society*, vol. 144, no. 8, p. 2621, 1997.

[18] O. Schneider, G. O. Ilevbare, J. R. Scully, and R. G. Kelly, "In situ confocal laser scanning microscopy of AA 2024-T3 corrosion metrology," *Journal of The Electrochemical Society*, vol. 151, no. 8, p. B465, 2004.

[19] V. Guillaumin and G. Mankowski, "Localized corrosion of 2024 T351 aluminium alloy in chloride media," *Corrosion Science*, vol. 41, pp. 421–438, Mar. 1998.

[20] C. Blanc, B. Lavelle, and G. Mankowski, "The role of precipitates enriched with copper on the susceptibility to pitting corrosion of the 2024 aluminium alloy," *Corrosion Science*, vol. 39, pp. 495–510, Mar. 1997.

[21] M. A. Amin, "Metastable and stable pitting events on Al induced by chlorate and perchlorate anions—polarization, XPS and SEM studies," *Electrochimica Acta*, vol. 54, pp. 1857–1863, Feb. 2009.

[22] S. T. Pride, "Metastable pitting of aluminum and criteria for the transition to stable pit growth," *Journal of The Electrochemical Society*, vol. 141, no. 11, p. 3028, 1994.

[23] A. Boag, R. Taylor, T. Muster, N. Goodman, D. McCulloch, C. Ryan, B. Rout, D. Jamieson, and A. Hughes, "Stable pit formation on AA2024-T3 in a NaCl environment," *Corrosion Science*, vol. 52, pp. 90–103, Jan. 2010.

[24] A. Kreta, M. Rodošek, L. S. Perše, B. Orel, M. Gaberšček, and A. Š. Vuk, "In situ electrochemical AFM, ex situ IR reflection–absorption and confocal raman studies of corrosion processes of AA 2024-T3," *Corrosion Science*, vol. 104, pp. 290–309, Mar. 2016.

[25] N. Li, C. Dong, C. Man, and J. Yao, "In situ electrochemical atomic force microscopy and auger electro spectroscopy study on the passive film structure of 2024-T3 aluminum alloy combined with a density functional theory calculation," *Advanced Engineering Materials*, vol. 21, p. 1900386, Sept. 2019.

[26] Y. Mao, A. Gokhale, and J. Harris, "Computer simulations of realistic microstructures of coarse constituent particles in a hot-rolled aluminum alloy," *Computational Materials Science*, vol. 37, pp. 543–556, Oct. 2006.

[27] M. D. Hager, P. Greil, C. Leyens, S. van der Zwaag, and U. S. Schubert, "Self-healing materials," *Advanced Materials*, vol. 22, pp. 5424–5430, Sept. 2010.

[28] S. García, H. Fischer, and S. van der Zwaag, "A critical appraisal of the potential of self healing polymeric coatings," *Progress in Organic Coatings*, vol. 72, pp. 211–221, Nov. 2011.

[29] M. Montemor, "Functional and smart coatings for corrosion protection: A review of recent advances," *Surface and Coatings Technology*, vol. 258, pp. 17–37, Nov. 2014.

[30] S. B. Ulaeto, R. Rajan, J. K. Pancrecious, T. Rajan, and B. Pai, "Developments in smart anticorrosive coatings with multifunctional characteristics," *Progress in Organic Coatings*, vol. 111, pp. 294–314, Oct. 2017.

[31] F. Zhang, P. Ju, M. Pan, D. Zhang, Y. Huang, G. Li, and X. Li, "Self-healing mechanisms in smart protective coatings: A review," *Corrosion Science*, vol. 144, pp. 74–88, Nov. 2018.

[32] J. de Damborenea, A. Conde, and M. Arenas, "Corrosion inhibition with rare earth metal compounds in aqueous solutions," in *Rare Earth-Based Corrosion Inhibitors*, pp. 84–116, Elsevier, 2014.

[33] M. Zheludkevich, K. Yasakau, S. Poznyak, and M. Ferreira, "Triazole and thiazole derivatives as corrosion inhibitors for AA2024 aluminium alloy," *Corrosion Science*, vol. 47, pp. 3368–3383, Dec. 2005.

[34] T. Harvey, S. Hardin, A. Hughes, T. Muster, P. White, T. Markley, P. Corrigan, J. Mardel, S. Garcia, J. Mol, and A. Glenn, "The effect of inhibitor structure on the corrosion of AA2024 and AA7075," *Corrosion Science*, vol. 53, pp. 2184–2190, June 2011.

[35] A. Khramov, N. Voevodin, V. Balbyshev, and M. Donley, "Hybrid organo-ceramic corrosion protection coatings with encapsulated organic corrosion inhibitors," *Thin Solid Films*, vol. 447-448, pp. 549–557, Jan. 2004.

[36] I. A. Kartsonakis, E. P. Koumoulos, and C. A. Charitidis, "Advancement in corrosion resistance of AA 2024-T3 through sol-gel coatings including nanocontainers," *Manufacturing Review*, vol. 4, p. 2, 2017.

[37] H. Shi, L. Wu, J. Wang, F. Liu, and E.-H. Han, "Sub-micrometer mesoporous silica containers for active protective coatings on AA 2024-T3," *Corrosion Science*, vol. 127, pp. 230–239, Oct. 2017.

[38] A. Balaskas, I. Kartsonakis, L.-A. Tziveleka, and G. Kordas, "Improvement of anti-corrosive properties of epoxy-coated AA 2024-T3 with TiO_2 nanocontainers loaded with 8-hydroxyquinoline," *Progress in Organic Coatings*, vol. 74, pp. 418–426, July 2012.

[39] C. Drewien, M. O. Eatough, D. R. Tallant, C. R. Hills, and R. G. Buchheit, "Lithium-aluminum-carbonate-hydroxide hydrate coatings on aluminum alloys: Composition, structure, and processing bath chemistry," *Journal of Materials Research*, vol. 11, pp. 1507–1513, June 1996.

[40] Y. Liu, P. Visser, X. Zhou, S. B. Lyon, T. Hashimoto, M. Curioni, A. Gholinia, G. E. Thompson, G. Smyth, S. R. Gibbon, D. Graham, J. M. C. Mol, and H. Terryn, "Protective film formation on AA2024-t3 aluminum alloy by leaching of lithium carbonate from an organic coating," *Journal of The Electrochemical Society*, vol. 163, pp. C45–C53, Dec. 2015.

[41] P. Visser, Y. Liu, H. Terryn, and J. M. C. Mol, "Lithium salts as leachable corrosion inhibitors and potential replacement for hexavalent chromium in organic coatings for the protection of aluminum alloys," *Journal of Coatings Technology and Research*, vol. 13, pp. 557–566, Apr. 2016.

[42] P. Visser, H. Terryn, and J. M. Mol, "Active corrosion protection of various aluminium alloys by lithium-leaching coatings," *Surface and Interface Analysis*, vol. 51, pp. 1276–1287, Mar. 2019.

[43] B. R. W. Hinton, D. R. Arnott, and N. E. Ryan, "Inhibition of aluminium alloy corrosion by cerous cations," *Metals Forum*, vol. 7, pp. 211–217, 1984.

[44] D. Arnott, N. Ryan, B. Hinton, B. Sexton, and A. Hughes, "Auger and XPS studies of cerium corrosion inhibition on 7075 aluminum alloy," *Applications of Surface Science*, vol. 22-23, pp. 236–251, May 1985.

[45] B. Hinton, "Corrosion inhibition with rare earth metal salts," *Journal of Alloys and Compounds*, vol. 180, pp. 15–25, Mar. 1992.

[46] D. R. Arnott, B. R. W. Hinton, and N. E. Ryan, "Cationic-film-forming inhibitors for the protection of the AA 7075 aluminum alloy against corrosion in aqueous chloride solution," *CORROSION*, vol. 45, pp. 12–18, Jan. 1989.

[47] S. R. Taylor and B. D. Chambers, "Identification and characterization of nonchromate corrosion inhibitor synergies using high-throughput methods," *CORROSION*, vol. 64, pp. 255–270, Mar. 2008.

[48] P. J. Denissen and S. J. Garcia, "Cerium-loaded algae exoskeletons for active corrosion protection of coated AA2024-T3," *Corrosion Science*, vol. 128, pp. 164–175, Nov. 2017.

[49] C. D. Dieleman, P. J. Denissen, and S. J. Garcia, "Long-term active corrosion protection of damaged coated-AA2024-T3 by embedded electrospun inhibiting nanonetworks," *Advanced Materials Interfaces*, vol. 5, p. 1800176, Apr. 2018.

[50] D. Snihirova, S. V. Lamaka, M. Taryba, A. N. Salak, S. Kallip, M. L. Zheludkevich, M. G. S. Ferreira, and M. F. Montemor, "Hydroxyapatite microparticles as feedback-active reservoirs of corrosion inhibitors," *ACS Applied Materials & Interfaces*, vol. 2, pp. 3011–3022, Oct. 2010.

[51] S. Dias, S. Lamaka, C. Nogueira, T. Diamantino, and M. Ferreira, "Sol–gel coatings modified with zeolite fillers for active corrosion protection of AA2024," *Corrosion Science*, vol. 62, pp. 153–162, Sept. 2012.

[52] T. G. Harvey, "Cerium-based conversion coatings on aluminium alloys: a process review," *Corrosion Engineering, Science and Technology*, vol. 48, pp. 248–269, June 2013.

[53] C. E. Castano, W. G. Fahrenholtz, and M. J. O'Keefe, "Ceria-based coatings and pigments," in *Cerium Oxide (CeO_2): Synthesis, Properties and Applications*, pp. 211–257, Elsevier, 2020.

[54] J. Alba-Galvín, L. González-Rovira, M. Bethencourt, F. Botana, and J. Sánchez-Amaya, "Influence of aerospace standard surface pretreatment on the intermetallic phases and CeCC of 2024-T3 Al-Cu alloy," *Metals*, vol. 9, p. 320, Mar. 2019.

[55] P. Campestrini, H. Terryn, A. Hovestad, and J. de Wit, "Formation of a cerium-based conversion coating on AA2024: relationship with the microstructure," *Surface and Coatings Technology*, vol. 176, pp. 365–381, Jan. 2004.

[56] A. Hughes, J. Mol, and I. Cole, "The cost and availability of rare earth-based corrosion inhibitors," in *Rare Earth-Based Corrosion Inhibitors*, pp. 291–305, Elsevier, 2014.

[57] K. Binnemans, P. T. Jones, B. Blanpain, T. V. Gerven, Y. Yang, A. Walton, and M. Buchert, "Recycling of rare earths: a critical review," *Journal of Cleaner Production*, vol. 51, pp. 1–22, July 2013.

[58] MineralPrices.com. https://mineralprices.com/. Online; Last accessed: 8 - 02 - 2020.

[59] E. McCafferty, "Corrosion inhibitors," in *Introduction to Corrosion Science*, pp. 357–402, Springer New York, Nov. 2009.

[60] K. A. Yasakau, M. L. Zheludkevich, and M. G. S. Ferreira, "Lanthanide salts as corrosion inhibitors for AA5083. Mechanism and efficiency of corrosion inhibition," *Journal of The Electrochemical Society*, vol. 155, no. 5, p. C169, 2008.

[61] T. Behrsing, G. Deacon, and P. Junk, "The chemistry of rare earth metals, compounds, and corrosion inhibitors," in *Rare Earth-Based Corrosion Inhibitors*, pp. 1–37, Elsevier, 2014.

[62] A. Davenport, H. Isaacs, and M. Kendig, "XANES investigation of the role of cerium compounds as corrosion inhibitors for aluminum," *Corrosion Science*, vol. 32, pp. 653–663, Jan. 1991.

[63] P. Rodič and I. Milošev, "Corrosion inhibition of pure aluminium and alloys AA2024-T3 and AA7075-T6 by Cerium(III) and Cerium(IV) salts," *Journal of The Electrochemical Society*, vol. 163, pp. C85–C93, Dec. 2015.

[64] A. J. Aldykewicz, "The investigation of cerium as a cathodic inhibitor for aluminum-copper alloys," *Journal of The Electrochemical Society*, vol. 142, no. 10, p. 3342, 1995.

[65] D. Snihirova, M. Taryba, S. V. Lamaka, and M. F. Montemor, "Corrosion inhibition synergies on a model Al-Cu-Mg sample studied by localized scanning electrochemical techniques," *Corrosion Science*, vol. 112, pp. 408–417, Nov. 2016.

[66] L. Coelho, M. Mouanga, M.-E. Druart, I. Recloux, D. Cossement, and M.-G. Olivier, "A SVET study of the inhibitive effects of benzotriazole and cerium chloride solely and combined on an aluminium/copper galvanic coupling model," *Corrosion Science*, vol. 110, pp. 143–156, Sept. 2016.

[67] S. Kallip, A. C. Bastos, K. A. Yasakau, M. L. Zheludkevich, and M. G. Ferreira, "Synergistic corrosion inhibition on galvanically coupled metallic materials," *Electrochemistry Communications*, vol. 20, pp. 101–104, July 2012.

[68] M. van Soestbergen, S. Erich, H. Huinink, and O. Adan, "Inhibition of pH fronts in corrosion cells due to the formation of cerium hydroxide," *Electrochimica Acta*, vol. 110, pp. 491–500, Nov. 2013.

[69] K. A. Yasakau, M. L. Zheludkevich, S. V. Lamaka, and M. G. S. Ferreira, "Mechanism of corrosion inhibition of AA2024 by rare-earth compounds," *The Journal of Physical Chemistry B*, vol. 110, pp. 5515–5528, Mar. 2006.

[70] A. Kolics, A. S. Besing, P. Baradlai, and A. Wieckowski, "Cerium deposition on aluminum alloy 2024-T3 in acidic NaCl solutions," *Journal of The Electrochemical Society*, vol. 150, no. 11, p. B512, 2003.

[71] A. J. Aldykiewicz, "Studies of the formation of cerium-rich protective films using X-ray absorption near-edge spectroscopy and rotating disk electrode methods," *Journal of The Electrochemical Society*, vol. 143, no. 1, p. 147, 1996.

[72] B. Bouchaud, J. Balmain, G. Bonnet, and F. Pedraza, "pH-distribution of cerium species in aqueous systems," *Journal of Rare Earths*, vol. 30, pp. 559–562, June 2012.

[73] P. Yu, S. A. Hayes, T. J. O'Keefe, M. J. O'Keefe, and J. O. Stoffer, "The phase stability of cerium species in aqueous systems," *Journal of The Electrochemical Society*, vol. 153, no. 1, p. C74, 2006.

[74] A. Hughes, T. Harvey, N. Birbilis, A. Kumar, and R. Buchheit, "Coatings for corrosion prevention based on rare earths," in *Rare Earth-Based Corrosion Inhibitors*, pp. 186–232, Elsevier, 2014.

[75] I. I. Udoh, H. Shi, F. Liu, and E.-H. Han, "Synergistic effect of 3-amino-1, 2, 4-triazole-5-thiol and cerium chloride on corrosion inhibition of AA2024-T3," *Journal of The Electrochemical Society*, vol. 166, no. 6, pp. C185–C195, 2019.

[76] F. Scholes, C. Soste, A. Hughes, S. Hardin, and P. Curtis, "The role of hydrogen peroxide in the deposition of cerium-based conversion coatings," *Applied Surface Science*, vol. 253, pp. 1770–1780, Dec. 2006.

[77] P. Visser, H. Terryn, and J. Mol, "On the importance of irreversibility of corrosion inhibitors for active coating protection of AA2024-T3," *Corrosion Science*, vol. 140, pp. 272–285, Aug. 2018.

[78] H. D. Song, M. Lee, G.-P. Kim, I. Choi, and J. Yi, "Real-time optical monitoring of pt catalyst under the potentiodynamic conditions," *Scientific Reports*, vol. 6, Dec. 2016.

[79] F. Li, Z. Liu, T. Sun, C. Yang, W. Sun, X. Sun, Y. Ma, and X. Ding, "In situ analysis of electrocrystallization process of metal electrodeposition with confocal energy dispersive x-ray diffraction based on polycapillary x-ray optics," *Nuclear Instruments and Methods in Physics Research Section A: Accelerators, Spectrometers, Detectors and Associated Equipment*, vol. 785, pp. 201–205, June 2015.

[80] D. H. Han, S. Park, E. J. Kim, and T. D. Chung, "In situ confocal microscopy of electrochemical generation and collision of emulsion droplets in bromide redox system," *Electrochimica Acta*, vol. 252, pp. 164–170, Oct. 2017.

[81] T. Tokuda and M. Ives, "Pitting corrosion of Ni," *Corrosion Science*, vol. 11, pp. 297–306, May 1971.

[82] C. Merola, H.-W. Cheng, K. Schwenzfeier, K. Kristiansen, Y.-J. Chen, H. A. Dobbs, J. N. Israelachvili, and M. Valtiner, "In situ nano- to microscopic imaging and growth mechanism of electrochemical dissolution (e.g., corrosion) of a confined metal surface," *Proceedings of the National Academy of Sciences*, vol. 114, pp. 9541–9546, Aug. 2017.

[83] A. Chiba, I. Muto, Y. Sugawara, and N. Hara, "A microelectrochemical system for in situ high-resolution optical microscopy: Morphological characteristics of pitting at MnS inclusion in stainless steel," *Journal of The Electrochemical Society*, vol. 159, no. 8, pp. C341–C350, 2012.

[84] A. Chiba, I. Muto, Y. Sugawara, and N. Hara, "Microelectrochemical investigation of pit initiation and selective dissolution between MnS and stainless steel," *ECS Transactions*, vol. 50, pp. 15–23, Apr. 2013.

[85] A. M. Zimer, E. C. Rios, P. de Carvalho Dias Mendes, W. N. Gonçalves, O. M. Bruno, E. C. Pereira, and L. H. Mascaro, "Investigation of AISI 1040 steel corrosion in H_2S solution containing chloride ions by digital image processing coupled with electrochemical techniques," *Corrosion Science*, vol. 53, pp. 3193–3201, Oct. 2011.

[86] A. M. Zimer, M. A. D. Carra, E. C. Rios, E. C. Pereira, and L. H. Mascaro, "Initial stages of corrosion pits on AISI 1040 steel in sulfide solution analyzed by temporal series micrographs coupled with electrochemical techniques," *Corrosion Science*, vol. 76, pp. 27–34, Nov. 2013.

[87] B. Yuan, Z. Li, S. Tong, L. Li, and C. Wang, "In situ monitoring of pitting corrosion on stainless steel with digital holographic surface imaging," *Journal of The Electrochemical Society*, vol. 166, no. 11, pp. C3039–C3047, 2019.

[88] A. C. Balaskas, M. Curioni, and G. E. Thompson, "Evaluation of inhibitor performance by electrochemical methods: Comparative study of nitrate salts on AA 2024-T3," *Journal of The Electrochemical Society*, vol. 161, no. 9, pp. C389–C394, 2014.

[89] P. J. Denissen and S. J. Garcia, "Reducing subjectivity in EIS interpretation of corrosion and corrosion inhibition processes by in-situ optical analysis," *Electrochimica Acta*, vol. 293, pp. 514–524, Jan. 2019.

[90] P. J. Denissen, A. M. Homborg, and S. J. Garcia, "Interpreting electrochemical noise and monitoring local corrosion by means of highly resolved spatiotemporal real-time optics," *Journal of The Electrochemical Society*, vol. 166, no. 11, pp. C3275–C3283, 2019.

[91] Redox.me, "Magnetic mount raman electrochemical flow cell." https://redox.me/collections/spectro-electrochemical-cells/products/raman-efc-4-mm-path-0-7-ml-raman-electrochemical-flow-cell. Online; Last accessed: 8 - 01 - 2020.

[92] P. Thevenaz, U. Ruttimann, and M. Unser, "A pyramid approach to subpixel registration based on intensity," *IEEE Transactions on Image Processing*, vol. 7, no. 1, pp. 27–41, 1998.

[93] A. R. Trueman, "Determining the probability of stable pit initiation on aluminium alloys using potentiostatic electrochemical measurements," *Corrosion Science*, vol. 47, pp. 2240–2256, Sept. 2005.

[94] S. Garcia, T. Markley, J. Mol, and A. Hughes, "Unravelling the corrosion inhibition mechanisms of bi-functional inhibitors by EIS and SEM–EDS," *Corrosion Science*, vol. 69, pp. 346–358, Apr. 2013.

[95] P. Schmutz, "Characterization of AA2024-T3 by scanning kelvin probe force microscopy," *Journal of The Electrochemical Society*, vol. 145, no. 7, p. 2285, 1998.

[96] P. Campestrini, E. van Westing, H. van Rooijen, and J. de Wit, "Relation between microstructural aspects of AA2024 and its corrosion behaviour investigated using AFM scanning potential technique," *Corrosion Science*, vol. 42, pp. 1853–1861, Nov. 2000.

[97] P. Leblanc and G. S. Frankel, "A study of corrosion and pitting initiation of AA2024-T3 using atomic force microscopy," *Journal of The Electrochemical Society*, vol. 149, no. 6, p. B239, 2002.

[98] V. Guillaumin, P. Schmutz, and G. S. Frankel, "Characterization of corrosion interfaces by the scanning kelvin probe force microscopy technique," *Journal of The Electrochemical Society*, vol. 148, no. 5, p. B163, 2001.

[99] T. H. Muster and A. E. Hughes, "Applications and limitations of scanning kelvin probe force microscopy for the surface analysis of aluminum alloys," *Journal of The Electrochemical Society*, vol. 153, no. 11, p. B474, 2006.

[100] E. L. Ferrer, A. P. Rollon, H. D. Mendoza, U. Lafont, and S. J. Garcia, "Double-doped zeolites for corrosion protection of aluminium alloys," *Microporous and Mesoporous Materials*, vol. 188, pp. 8–15, Apr. 2014.

[101] M. A. Zadeh, J. Tedim, M. Zheludkevich, S. van der Zwaag, and S. Garcia, "Synergetic active corrosion protection of AA2024-T3 by 2D-anionic and 3D-cationic nanocontainers loaded with Ce and mercaptobenzothiazole," *Corrosion Science*, vol. 135, pp. 35–45, May 2018.

[102] L. Coelho, D. Cossement, and M.-G. Olivier, "Benzotriazole and cerium chloride as corrosion inhibitors for AA2024-T3: An EIS investigation supported by SVET and ToF-SIMS analysis," *Corrosion Science*, vol. 130, pp. 177–189, Jan. 2018.

[103] M. Forsyth, M. Seter, B. Hinton, G. Deacon, and P. Junk, "New 'green' corrosion inhibitors based on rare earth compounds," *Australian Journal of Chemistry*, vol. 64, no. 6, p. 812, 2011.

[104] Y. Peng, A. E. Hughes, J. I. Mardel, G. B. Deacon, P. C. Junk, M. Forsyth, B. R. W. Hinton, and A. E. Somers, "Leaching behavior and corrosion inhibition of a rare earth carboxylate incorporated epoxy coating system," *ACS Applied Materials & Interfaces*, vol. 11, pp. 36154–36168, Sept. 2019.

[105] N. Birbilis, R. G. Buchheit, D. L. Ho, and M. Forsyth, "Inhibition of AA2024-T3 on a phase-by-phase basis using an environmentally benign inhibitor, cerium dibutyl phosphate," *Electrochemical and Solid-State Letters*, vol. 8, no. 11, p. C180, 2005.

[106] I. Donati and S. Paoletti, "Material properties of alginates," in *Alginates: Biology and Applications*, pp. 1–53, Springer Berlin Heidelberg, 2009.

[107] A. Haug, B. Larsen, O. Smidsrød, J. Møller, J. Brunvoll, E. Bunnenberg, C. Djerassi, and R. Records, "A study of the constitution of alginic acid by partial acid hydrolysis," *Acta Chemica Scandinavica*, vol. 20, pp. 183–190, 1966.

[108] A. Haug, B. Larsen, O. Smidsrød, O. Smidsrød, G. Eriksson, R. Blinc, S. Paušak, L. Ehrenberg, and J. Dumanović, "Studies on the sequence of uronic acid residues in alginic acid," *Acta Chemica Scandinavica*, vol. 21, pp. 691–704, 1967.

[109] K. Y. Lee and D. J. Mooney, "Alginate: Properties and biomedical applications," *Progress in Polymer Science*, vol. 37, pp. 106–126, Jan. 2012.

[110] C. H. Goh, P. W. S. Heng, and L. W. Chan, "Alginates as a useful natural polymer for microencapsulation and therapeutic applications," *Carbohydrate Polymers*, vol. 88, pp. 1–12, Mar. 2012.

[111] S. Belbekhouche, N. Bousserrhine, V. Alphonse, F. L. Floch, Y. C. Mechiche, I. Menidjel, and B. Carbonnier, "Chitosan based self-assembled nanocapsules as antibacterial agent," *Colloids and Surfaces B: Biointerfaces*, vol. 181, pp. 158–165, Sept. 2019.

[112] T. Nalini, S. K. Basha, A. M. M. Sadiq, V. S. Kumari, and K. Kaviyarasu, "Development and characterization of alginate / chitosan nanoparticulate system for hydrophobic drug encapsulation," *Journal of Drug Delivery Science and Technology*, vol. 52, pp. 65–72, Aug. 2019.

[113] M. A. Khan, C. Yue, Z. Fang, S. Hu, H. Cheng, A. M. Bakry, and L. Liang, "Alginate/chitosan-coated zein nanoparticles for the delivery of resveratrol," *Journal of Food Engineering*, vol. 258, pp. 45–53, Oct. 2019.

[114] J. Cui, X. Li, Z. Pei, and Y. Pei, "A long-term stable and environmental friendly self-healing coating with polyaniline/sodium alginate microcapsule structure for corrosion protection of water-delivery pipelines," *Chemical Engineering Journal*, vol. 358, pp. 379–388, Feb. 2019.

[115] C. Coquery, F. Carosio, C. Negrell, N. Caussé, N. Pébère, and G. David, "New bio-based phosphorylated chitosan/alginate protective coatings on aluminum alloy obtained by the LbL technique," *Surfaces and Interfaces*, vol. 16, pp. 59–66, Sept. 2019.

[116] S. D. Mookhoek, H. R. Fischer, and S. van der Zwaag, "Alginate fibres containing discrete liquid filled vacuoles for controlled delivery of healing agents in fibre reinforced composites," *Composites Part A: Applied Science and Manufacturing*, vol. 43, pp. 2176–2182, Dec. 2012.

[117] W. Post, E. Jeoffroy, S. García, and S. van der Zwaag, "Self-healing glass fiber reinforced polymer composites based on montmorillonite reinforced compartmented alginate fibers," *Polymer Composites*, vol. 40, pp. 471–480, Nov. 2017.

[118] A. Tabaković, W. Post, D. Cantero, O. Copuroglu, S. J. Garcia, and E. Schlangen, "The reinforcement and healing of asphalt mastic mixtures by rejuvenator encapsulation in alginate compartmented fibres," *Smart Materials and Structures*, vol. 25, p. 084003, July 2016.

[119] S. Xu, X. Liu, A. Tabaković, and E. Schlangen, "Investigation of the potential use of calcium alginate capsules for self-healing in porous asphalt concrete," *Materials*, vol. 12, p. 168, Jan. 2019.

[120] A. Mignon, J. Vermeulen, G.-J. Graulus, J. Martins, P. Dubruel, N. D. Belie, and S. V. Vlierberghe, "Characterization of methacrylated alginate and acrylic monomers as versatile SAPs," *Carbohydrate Polymers*, vol. 168, pp. 44–51, July 2017.

[121] J. P. Paques, E. van der Linden, C. J. van Rijn, and L. M. Sagis, "Preparation methods of alginate nanoparticles," *Advances in Colloid and Interface Science*, vol. 209, pp. 163–171, July 2014.

[122] U. Schlemmer, W. Frølich, R. M. Prieto, and F. Grases, "Phytate in foods and significance for humans: Food sources, intake, processing, bioavailability, protective role and analysis," *Molecular Nutrition & Food Research*, vol. 53, pp. S330–S375, Sept. 2009.

[123] J. Gerke, "Phytate (inositol hexakisphosphate) in soil and phosphate acquisition from inositol phosphates by higher plants. A review," *Plants*, vol. 4, pp. 253–266, May 2015.

[124] G. B. Darband and M. Aliofkhazraei, "Electrochemical Phosphate Conversion Coatings: A Review," *Surface Review and Letters*, vol. 24, p. 1730003, Mar. 2017.

[125] B. Liu, X. Zhang, G. yong Xiao, and Y. peng Lu, "Phosphate chemical conversion coatings on metallic substrates for biomedical application: A review," *Materials Science and Engineering: C*, vol. 47, pp. 97–104, Feb. 2015.

[126] H. Shi, E.-H. Han, F. Liu, and S. Kallip, "Protection of 2024-T3 aluminium alloy by corrosion resistant phytic acid conversion coating," *Applied Surface Science*, vol. 280, pp. 325–331, Sept. 2013.

[127] S. Wang, H. Peng, Z. Shao, Q. Zhao, and N. Du, "Sealing of anodized aluminum with phytic acid solution," *Surface and Coatings Technology*, vol. 286, pp. 155–164, Jan. 2016.

[128] Y. Hao, L. A. Sani, T. Ge, and Q. Fang, "Phytic acid doped polyaniline containing epoxy coatings for corrosion protection of Q235 carbon steel," *Applied Surface Science*, vol. 419, pp. 826–837, Oct. 2017.

[129] Y. Hao, Y. Zhao, X. Yang, B. Hu, S. Ye, L. Song, and R. Li, "Self-healing epoxy coating loaded with phytic acid doped polyaniline nanofibers impregnated with benzotriazole for Q235 carbon steel," *Corrosion Science*, vol. 151, pp. 175–189, May 2019.

[130] S. Shen, X. yu Guo, P. Song, Y.-C. Pan, H. qiong Wang, Y. Wen, and H.-F. Yang, "Phytic acid adsorption on the copper surface: Observation of electrochemistry and raman spectroscopy," *Applied Surface Science*, vol. 276, pp. 167–173, July 2013.

[131] S. Shen, C. di Zhu, X. yu Guo, C. chuan Li, Y. Wen, and H.-F. Yang, "The synergistic mechanism of phytic acid monolayers and iodide ions for inhibition of copper corrosion in acidic media," *RSC Adv.*, vol. 4, no. 21, pp. 10597–10606, 2014.

[132] C. chuan Li, X. yu Guo, S. Shen, P. Song, T. Xu, Y. Wen, and H.-F. Yang, "Adsorption and corrosion inhibition of phytic acid calcium on the copper surface in 3wt% NaCl solution," *Corrosion Science*, vol. 83, pp. 147–154, June 2014.

[133] S. Shen, J. Du, X. yu Guo, Y. Wen, and H.-F. Yang, "Adsorption behavior of pH-dependent phytic acid micelles at the copper surface observed by raman and electrochemistry," *Applied Surface Science*, vol. 327, pp. 116–121, Feb. 2015.

[134] R. Zhang, H. Yang, Y. Sun, W. Song, X. Zhu, N. Wang, Y. Wang, Y. Pan, and Z. Zhang, "Competitive adsorption of 4-methyl-4h-1, 2, 4-triazole-3-thiol and Na salt of phytic acid on a silver surface: Raman spectral and electrochemical observations," *The Journal of Physical Chemistry C*, vol. 113, pp. 9748–9754, May 2009.

[135] J. Dong, Y. Wen, Y. Miao, Z. Xie, Z. Zhang, and H. Yang, "A nanoporous zirconium phytate film for immobilization of redox protein and the direct electrochemical biosensor," *Sensors and Actuators B: Chemical*, vol. 150, pp. 141–147, Sept. 2010.

[136] Y. Wang, X. Ma, Y. Wen, Y. Zheng, G. Duan, Z. Zhang, and H. Yang, "Phytic acid-based layer-by-layer assembly for fabrication of mesoporous gold film and its biosensor application," *Journal of The Electrochemical Society*, vol. 157, no. 1, p. K5, 2010.

[137] N. Wang, Y. Wen, Y. Wang, R. Zhang, X. Chen, B. Ling, S. Huan, and H. Yang, "The IP6micelle-stabilized small Ag cluster for synthesizing Ag–Au alloy nanoparticles and the tunable surface plasmon resonance effect," *Nanotechnology*, vol. 23, p. 145702, Mar. 2012.

[138] J. Ou and X. Chen, "Corrosion resistance of phytic acid / Ce (III) nanocomposite coating with superhydrophobicity on magnesium," *Journal of Alloys and Compounds*, vol. 787, pp. 145–151, May 2019.

[139] G. Williams, A. J. Coleman, and H. N. McMurray, "Inhibition of aluminium alloy AA2024-T3 pitting corrosion by copper complexing compounds," *Electrochimica Acta*, vol. 55, pp. 5947–5958, Aug. 2010.

[140] D. Snihirova, S. Lamaka, P. Taheri, J. Mol, and M. Montemor, "Comparison of the synergistic effects of inhibitor mixtures tailored for enhanced corrosion protection of bare and coated AA2024-T3," *Surface and Coatings Technology*, vol. 303, pp. 342–351, Oct. 2016.

[141] W. Qafsaoui, A. E. Taouil, M. W. Kendig, O. Heintz, H. Cachet, S. Joiret, and H. Takenouti, "Corrosion protection of bronze using 2, 5-dimercapto-1, 3, 4-thiadiazole as organic inhibitor: spectroscopic and electrochemical investigations," *Journal of Applied Electrochemistry*, vol. 49, pp. 823–837, June 2019.

[142] L. Huang, F. Tang, B. Hu, J. Shen, T. Yu, and Q. Meng, "Chemical reactions of 2, 5-dimercapto-1, 3, 4-thiadiazole (DMTD) with metallic copper, silver, and mercury," *The Journal of Physical Chemistry B*, vol. 105, pp. 7984–7989, Aug. 2001.

[143] L. Liu, X. Pan, J. Xing, and J. Qian, "Anti-corrosion behavior of thiadiazole derivatives for silver strip in hydrogen sulfide solutions," *Anti-Corrosion Methods and Materials*, vol. 62, pp. 353–362, Nov. 2015.

[144] W. Chen, H. Q. Luo, and N. B. Li, "Inhibition effects of 2, 5-dimercapto-1, 3, 4-thiadiazole on the corrosion of mild steel in sulphuric acid solution," *Corrosion Science*, vol. 53, pp. 3356–3365, Oct. 2011.

[145] M. Kendig and C. Yan, "Critical concentrations for selected oxygen reduction reaction inhibitors," *Journal of The Electrochemical Society*, vol. 151, no. 12, p. B679, 2004.

[146] Patiha, E. Heraldy, Y. Hidayat, and M. Firdaus, "The Langmuir isotherm adsorption equation: The monolayer approach," *IOP Conference Series: Materials Science and Engineering*, vol. 107, p. 012067, Feb. 2016.

[147] N. Rosero-Navarro, S. Pellice, A. Durán, and M. Aparicio, "Effects of ce-containing sol–gel coatings reinforced with SiO_2 nanoparticles on the protection of AA2024," *Corrosion Science*, vol. 50, pp. 1283–1291, May 2008.

[148] B. Prakashaiah, D. V. Kumara, A. A. Pandith, A. N. Shetty, and B. A. Rani, "Corrosion inhibition of 2024-T3 aluminum alloy in 3.5% NaCl by thiosemicarbazone derivatives," *Corrosion Science*, vol. 136, pp. 326–338, May 2018.

[149] E. A. Matter, S. Kozhukharov, M. Machkova, and V. Kozhukharov, "Electrochemical studies on the corrosion inhibition of AA2024 aluminium alloy by rare earth ammonium nitrates in 3.5% NaCl solutions," *Materials and Corrosion*, vol. 64, pp. 408–414, Jan. 2012.

[150] P. Rodič and I. Milošev, "The influence of additional salts on corrosion inhibition by cerium(III) acetate in the protection of AA7075-T6 in chloride solution," *Corrosion Science*, vol. 149, pp. 108–122, Apr. 2019.